

Numerical Investigation of One-Dimensional Storage
Tank Models and the Development of Analytical
Modelling Techniques

NUMERICAL INVESTIGATION OF ONE-DIMENSIONAL
STORAGE TANK MODELS AND THE DEVELOPMENT OF
ANALYTICAL MODELLING TECHNIQUES

By CODY UNRAU, B.Sc.

A THESIS SUBMITTED TO THE SCHOOL OF GRADUATE STUDIES IN PARTIAL
FULFILLMENT OF THE REQUIREMENTS FOR THE DEGREE OF MASTER OF
APPLIED SCIENCE

Master of Applied Science (2017)

McMaster University

Mechanical Engineering

Hamilton, Ontario, Canada

TITLE: Numerical Investigation of One-Dimensional Storage Tank
Models and the Development of Analytical Modelling
Techniques

AUTHOR: Cody Unrau
B. Eng., Mechanical Engineering
McMaster University, Hamilton, Canada

SUPERVISOR: Dr. Marilyn Lightstone

NUMBER OF PAGES: xxv, 185

Abstract

To assess the long-term performance of a solar thermal system, mathematical models that accurately capture the effects of heat transfer within and interactions between individual components are required. For solar domestic hot water systems, the components can include the solar collectors, storage tanks, heat exchangers, pumps, and associated piping. In addition, weather data and demand profiles are also required. Simplified models for each component are needed to reduce the computational time required to run long-term simulations. The simplified models, however, must also be sufficiently accurate in order to provide meaningful system-level results.

Accurate prediction of the temperature profiles in the storage tanks of these systems is important since the temperature within the tank has a large impact on the efficiency of the entire system. TRNSYS, which is a commercial code commonly used for such simulations, contains a variety of different one-dimensional storage tank models. Previous research has indicated that these models have deficiencies in predicting experimental data. Therefore, this thesis is focussed on the analysis of the tank modelling used in TRNSYS. Results of this thesis show that the poor predictions are a result of numerical diffusion due to insufficient grid resolution. The correct theoretical profiles could be obtained by using a large number of nodes. However, this would lead to a significant increase in computational time.

Alternative modelling strategies were also developed using analytical techniques to more accurately predict the temperature profiles within a storage tank while keeping a relatively low computational cost. Different models were created which considered the different mixing mechanisms present in a storage tank, such as increasing inlet temperatures with time, heat losses to the surroundings, tank wall heat conduction, and inlet jet mixing.

Acknowledgements

Firstly, I would like to express my sincere gratitude to my supervisor, Dr. Marilyn F. Lightstone of the Department of Mechanical Engineering at McMaster University, for all of her support and motivation during my Master's research. I am thankful for her patience and for her extensive knowledge that helped me accomplish all that I have.

I would also like to thank Dr. Stephen Harrison of the Department of Mechanical and Materials Engineering at Queen's University for his insight and motivation for the topic of this thesis.

I also acknowledge the financial support provided by the Natural Sciences and Engineering Research Council (NSERC), Smart Net-Zero Energy Buildings Strategic Research Network (SNEBRN).

Finally, I would like to thank my parents, sister, and my colleagues in the CFD lab for all of their support and encouragement.

Glossary of Terms

Acronyms and Abbreviations

Symbol	Definition
CFD	Computational Fluid Dynamics
DHW	Domestic Hot Water
DLSC	Drake Landing Solar Community

Nomenclature

Symbol	Definition
<i>A</i>	Area (m^2)
<i>C</i>	Vertical location of the thermocline center with respect to the top of the tank where the inlet is located (m)
<i>C_P</i>	Specific Heat Capacity (J/kgK)
<i>D</i>	Tank Diameter (m)
<i>E</i>	Total Solar Thermal System Energy (W)
<i>f</i>	Solar Fraction ($Q_{solar\ to\ load}/Q_{load}$)
<i>H</i>	Tank Height (m)
<i>h</i>	Convective Heat Transfer Coefficient (W/m^2K)
<i>k</i>	Thermal Conductivity (W/mK)

L	Tank Length/Height (m)
$LMTD$	Log Mean Temperature Difference
m	Mass (kg)
\dot{m}	Mass Flow Rate (kg/s)
n/N	Total Number of One-Dimensional Nodes
P	Tank Perimeter (m)
Q	Heat Transfer (J)
\dot{Q}	Rate of Heat Transfer (W)
T	Temperature ($^{\circ}C$)
t	Time (s)
U	Tank Wall Heat Loss Coefficient (W/m^2K)
u	Fluid Velocity (m/s)
V	Volume (m^3)
\dot{V}	Volumetric Flow Rate (m^3/s)
W	Thermocline Width (m)
x	Horizontal Location in the Storage Tank (m)
Z	Non-Dimensional Tank Location (x/H)

Greek Letters

Symbol	Definition
α	Thermal Diffusivity (m^2/s)
α'	Eddy Thermal Diffusivity (Nizami) (m^2/s)
β	Thermal Expansion Coefficient ($1/K$)
δ	Storage Tank Region Designation for Nizami's Quasi One-Dimensional Model
ϵ	Eddy Thermal Diffusivity (Zurigat) (m^2/s)
μ	Fluid Viscosity ($kg/m\ s$)
ρ	Density (kg/m^3)
τ/θ	Non-Dimensional Temperature

Subscripts

Symbol	Definition
<i>actual</i>	Value for an actual storage tank
<i>avg/ave</i>	Average value
<i>aux</i>	Value for an auxiliary heater
<i>c</i>	Value for the cold tank region
<i>charge</i>	Value which occurs during tank charging
<i>cond</i>	Value due to conduction

<i>crit</i>	Critical value
<i>del</i>	Value delivered to the heating load
<i>discharge</i>	Value which occurs during tank discharging
<i>elec</i>	Value entering system from an electrical source
<i>ent</i>	Value for the entrainment into the inlet jet
<i>env</i>	Value for the environment surrounding the storage tank
<i>exp</i>	Value obtained from experiments
<i>h</i>	Value for the hot tank region
<i>i</i>	Arbitrary node value (one-dimensional models)
<i>intial</i>	Initial value at the start of a simulation
<i>j</i>	Value for the inlet jet of a storage tank
<i>k</i>	Arbitrary time step number (one-dimensional models)
<i>r</i>	Value for the inlet mixing region of a storage tank
<i>s</i>	Value at the surface
<i>sim</i>	Value obtained from simulations
<i>fluid</i>	Value of the tank fluid
<i>I</i>	Average value for the inlet mixing region of a storage tank
<i>ideal</i>	Value for the ideal storage tank (perfectly stratified)
<i>in</i>	Value at the inlet of the tank/node
<i>initial</i>	Initial value within the tank

<i>load</i>	Value required by the load
<i>loss</i>	Value lost to the storage tank surroundings
<i>mains</i>	Value for the mains water entering the system
<i>mixed</i>	Value for a fully mixed storage tank
<i>o</i>	Value at the wall boundary for the semi-infinite wall solution
<i>out</i>	Value leaving the tank/node
<i>P</i>	Value for the inlet pipe
<i>p</i>	Value for the plume within the inlet jet mixing region
<i>pump</i>	Value for the pump in the solar thermal system
<i>ref</i>	Reference Value
<i>solar to load</i>	Value leaving the solar thermal system and delivered to load
<i>sun</i>	Value from the sun (due to incident radiation)
<i>tank</i>	Value for the entire storage tank
<i>therm</i>	Value for the thermocline in a storage tank
<i>top tank</i>	Value at the top of the thermal storage tank
<i>total</i>	Total value for a specific node
<i>wall</i>	Value of the tank wall
<i>whc</i>	Value for the tank wall heat conduction
∞	Value for the tank surroundings

Dimensionless Groupings

Symbol	Definition
<i>Ar</i>	Archimedes Number ($g\Delta\rho D^3/\rho u_{in}^2 D_P^2$)
<i>Fr</i>	Froude Number (u_{in}/\sqrt{gH})
<i>Gr</i>	Grashoff Number ($g\beta(T_{in} - T_{initial})H^3/\nu^2$)
<i>Re</i>	Reynolds Number ($\rho u_{in} D/\mu$)
<i>Ri</i>	Richardson Number ($g\beta(T_{in} - T_{initial})H/u_{in}^2$)

Table of Contents

Abstract	iii
Acknowledgements	iv
Glossary of Terms	v
Table of Contents	xi
List of Figures	xv
List of Tables	xxiv
Chapter 1 Introduction	1
1.1 Solar Thermal Systems	1
1.2 Solar Thermal Storage Tanks	4
1.3 Thermal Stratification	4
1.4 System Simulation Modelling	7
1.5 Problem/Motivation	9
1.6 Objective and Approach	11
1.7 Outline of Thesis	12
Chapter 2 Thermal Storage Tank Behaviour	14
2.1 Thermal Stratification in Storage Tanks	14
2.1.1 Inlet Jet Mixing	16

2.1.2	Fluid Conduction	22
2.1.3	Tank Wall Heat Conduction	23
2.1.4	Heat Losses to Surroundings	26
2.2	Dimensionless Numbers.....	28
2.3	Summary	30
Chapter 3	Thermal Storage Tank Models for System Simulation.....	31
3.1	One-Dimensional Multi-Node Models.....	31
3.1.1	TRNSYS One-Dimensional Models.....	31
3.1.2	Quasi One-Dimensional Model	42
3.2	Numerical Diffusion in One-Dimensional Models	53
3.3	Alternative Modelling Techniques.....	58
3.3.1	TRNSYS Plug Flow Model	58
3.3.2	One-Dimensional Adaptive-Grid Model	60
3.4	Summary	64
Chapter 4	Analysis of TRNSYS One-Dimensional Storage Tank Models	65
4.1	Simple Case Analysis.....	66
4.2	Analytical Solution.....	69
4.3	Simulation Results and Discussion	73
4.3.1	Case 1 Results	74

4.3.2	Case 2 Results	79
4.4	Numerical Diffusion Analysis.....	86
4.4.1	In-House One-Dimensional Code Comparison	86
4.4.2	Taylor Series Expansion of the Discretized Energy Equation.....	88
4.4.3	Comparison with Experimental Data (Chu [12]).....	94
4.5	Conclusions	99
Chapter 5	Development of Analytical Modelling Strategies.....	101
5.1	Idealized Analytical Solution	101
5.2	Additional Considerations.....	103
5.2.1	Variable Inlet Temperatures	104
5.2.2	Heat Losses to the Surroundings.....	110
5.2.3	Tank Wall Conduction.....	115
5.2.4	Inlet Jet Mixing.....	118
5.3	Conclusions	136
Chapter 6	Conclusions and Future Work	139
6.1	Performance of the TRNSYS One-Dimensional Multi-node Models.....	140
6.2	Development of New Analytical Modelling Techniques.....	142
6.3	Recommendations for Future Work.....	144
References	147

Appendix A	Semi-Infinite Wall Solution Comparison for Storage Tank Conduction	151
Appendix B	RMS Errors for TRNSYS Tank Model Case Studies	154
Appendix C	Taylor Series Expansion of Energy Equation	158
C.1	Converting Time Derivatives to Spatial Derivatives	158
C.2	Taylor Series Expansions for Each Term.....	159
C.3	Combining Discretized Terms	162
Appendix D	MATLAB Code for the Analytical Models	164
D.1	Ideal Analytical Model Code	164
D.2	Increasing Inlet Temperature Analytical Model Code	166
D.3	Heat Losses to the Surroundings Analytical Code Model	169
D.4	Wall Heat Conduction Analytical Model Code	172
D.5	Inlet Jet Mixing Analytical Model Code.....	175
Appendix E	Inlet Jet Mixing Model Validation	180
E.1	2D Axisymmetric Simulation Conditions	180
E.1.1	Storage Tank Mesh	180
E.1.2	ANSYS CFX 14.0 Simulation Parameters	182
E.2	Choice of Initial Volume for Region 2.....	183

List of Figures

Figure 1.1 – Schematic of a solar thermal system consisting of a solar collector, a storage tank, a pump, and piping between the components as well as to the heating load and from the mains.	2
Figure 1.2 – (a) Hourly domestic hot water flow rate required by for a heating load [5], (b) Typical available solar radiation over a 24 hour period [6].	3
Figure 1.3 – Temperature profiles for a perfectly stratified tank at different times during charging. (a) $t = t_1$, (b) $t = t_2$, (c) $t = t_{final}$	5
Figure 1.4 – Varying levels of stratification, (a) Moderate level of stratification with a small thermocline width, (b) Low level of stratification with a large thermocline width, (c) No thermal stratification with a fully mixed tank [8].	5
Figure 1.5 – Yearly solar fraction versus the collector flow rate for a perfectly stratified tank and a fully mixed tank [9].	6
Figure 1.6 – Components of a solar thermal system studied by Chu [12] consisting of collectors, cold and hot storage tanks, and a heat pump.	8
Figure 1.7 – TRNSYS visualization of the component models used to simulate the conditions studied by Chu [12] to determine the accuracy of the hot storage tank model.	10
Figure 1.8 – LEFT: Storage tank thermocouple positioning used to determine the experimental temperature profiles, RIGHT: Simulation and experimental temperature profile results obtained by Chu [12].	10
Figure 2.1 – Energy inputs and outputs for the overall solar thermal system.	15

Figure 2.2 – Schematic of a storage tank showing the inlet jet mixing as the initial tank fluid is entrained into the jet stream [19]	17
Figure 2.3 – Experimental temperature profile results obtained by Oliveski et al. [18] showing an increasing temperature at the top of the tank for two different cases at different times during the simulation (LEFT: 10, 40 70 and 100 minutes; RIGHT: 10, 30, 50, 70, and 90 minutes).....	18
Figure 2.4 – Velocity vectors after (a) 10 min, (b) 40 min, and (c) 70 min predicted with CFD showing the inlet jet penetration depth and varying velocity patterns within the tank [17].	19
Figure 2.5 – Different inlet baffle designs tested by Shah and Furbo [21] and numerical results for tank discharging at 2 different times. LEFT – Raw pipe entering tank, MIDDLE – Metro, hemispherical baffle plate above inlet pipe, RIGHT – Large baffle plate above inlet pipe.	21
Figure 2.6 – Temperature profiles at different times showing an increasing thermocline width due to conduction between the hot and cold regions [27]	23
Figure 2.7 – Temperature profiles at different times showing the conduction of heat through a solid determined by the semi-infinite wall solution [29]	23
Figure 2.8 – Schematic of wall heat conduction showing heat entering the wall from the hot fluid region (Region 1) and leaving into the cold fluid region (Region 2) [19].	25

Figure 2.9 – Schematic of the thermal storage tank used by Oliveski et al. [18] to study the temperature profiles with time with the effects of heat losses to the surroundings.	26
Figure 2.10 – Temperature profile results obtained by Oliveski et al. [18] showing the decrease in the temperature of an initially constant temperature tank with time as a result of the heat losses to the surroundings. Due to natural convection, colder fluid falls to the bottom of the tank.	27
Figure 3.1 – One-dimensional node discretization of a thermal storage tank use by the TRNSYS models.	32
Figure 3.2 – Energy flows into and out of each node used to calculate the node temperatures for the TRNSYS one-dimensional models [33].	34
Figure 3.3 – Schematic of a storage tank showing hot fluid entering below cold fluid layers. A mixing algorithm is used to account for the rise of hot fluid due to buoyancy [33]	38
Figure 3.4 – Accuracy of two different TRNSYS one-dimensional models: Old Model (Type 4) and New Model (Type 60) [33]. (a) Temperature profile comparison for a small time step size (1 min), (b) Temperature profiles for a large time step (1 hour).	41
Figure 3.5 – Schematic of the modelling concept used by Nizami [17]. Region $\delta 1$ consists of the inlet jet, region $\delta 2$ involves the recirculation region where fluid enters from the jet region and is redirected downward due to the tank walls, and region $\delta 3$ makes up the rest of the inlet mixing region where fluid enters from region $\delta 2$ at the top	

and leaves due to the entrainment into the jet and out the bottom to the rest of the tank.....	44
Figure 3.6 – Node discretization used by Nizami to model the inlet mixing effects with a quasi-one-dimensional model [17]. The jet region, $\delta 1$, is represented as a single node while regions $\delta 2$ and $\delta 3$ are divided into N one-dimensional nodes in the axial direction.	45
Figure 3.7 – Jet penetration depth calculated by models developed by different researchers for a range of Richardson numbers between 0.001 and 100 [38].	50
Figure 3.8 – Schematic of the different velocity regions near a circular jet [19]. The momentum driven jet region is indicated separately from the buoyancy drive plume region where there are different diffusion characteristics.....	52
Figure 3.9 – Comparison of the results obtained by the different correlations for the turbulent jet diffusivity for a range of Richardson numbers from 0.001 to 0.1.....	53
Figure 3.10 – Variation in the amount of diffusion shown by the temperature profiles determined by a one-dimensional model of a storage tank with different amounts of nodes [39].....	54
Figure 3.11 – Visualization of numerical diffusion after a single time step. (a) shows the initial temperature profile, (b) shows the actual profile after a single time step where hot fluid has filled a portion of the next node, and (c) shows the profile output by a one-dimensional model with a fully mixed temperature for the middle node.	55
Figure 3.12 – Description of the process used to calculate the temperature profile in a storage tank using the TRNSYS plug flow model (Type 38) [11].	59

Figure 3.13 – Schematic of the node distribution used for the adaptive-grid plug flow model developed by Powell and Edgar [39].	61
Figure 3.14 – Visualization of the different events determined by the adaptive-grid plug flow model. (a) Initial charging phase with stationary nodes as the thermocline moves downwards, (b) tank nodes move downwards with the thermocline when the center reaches the middle node, (c) the thermocline center is kept at the middle node as the volumes of node n and node 1 change, (d) when the nodes reach the bottom of the tank, they become stationary as the thermocline continues downwards [39].	63
Figure 4.1 – Tank dimensions and initial conditions used for (a) Case 1 and (b) Case 2 to study the TRNSYS one-dimensional models.	67
Figure 4.2 – Experimental temperature profile showing a large variation in the temperature of the hot and cold regions above and below the thermocline [41].	72
Figure 4.3 – Limits of the thermocline thicknesses determined using Eq. (4.7) for different cut-off values, X	73
Figure 4.4 – Temperature vs tank depth results for Case 1 after 4 hours into the simulation with varying numbers of nodes and 1 second time steps. (a) Type 534 model, (b) Type 60 model, (c) Type 4 model.....	76
Figure 4.5 – Temperature vs tank depth results for Case 2 after 4 hours with varying time step sizes and 50 nodes. (a) Type 534 model, (b) Type 60 model, (c) Type 4 model.	78

Figure 4.6 – Temperature vs tank depth results for Case 2 after 1 hour with varying numbers of nodes and 1 second time steps. (a) Type 534 model, (b) Type 60 model, (c) Type 4 model.....	80
Figure 4.7 – Temperature vs tank depth results for Case 2 after 1 hour for varying time step sizes and 50 nodes. Plotted model results show the time-averaged nodal temperatures. (a) Type 534 model, (b) Type 60 model, (c) Type 4 model.....	83
Figure 4.8 – Temperature vs tank depth results for Case 2 after 1 hour with varying time step sizes and 50 nodes. Plotted model results are time-average nodal temperatures at half a time step ahead to compare with analytical results. (a) Type 534 model, (b) Type 60 model, (c) Type 4.....	84
Figure 4.9 – Temperature vs tank depth results for Case 2 after 1 hour with an increasing amount of nodes and 1 second time steps. (a) shows the comparison between the TRNSYS Type 534 model and the in-house code up to the maximum of 100 nodes allowed by TRNSYS. (b) shows the in-house code results for 100 to 1000 nodes.	87
Figure 4.10 – Temperature vs tank depth results for Case 2 after 1 hour using 1 second time steps. The TRNSYS Type 60 results are compared with the analytical solution and the analytical solution with the additional diffusion. (a) 100, (b) 50, (c) 10 Nodes.	93
Figure 4.11 – Temperature vs time results at 5 different tank depths. The idealized analytical model results are compared with the experimental and simulation results obtained by Chu [12].	96

Figure 4.12 – Temperature vs time results at 5 different tank depths. The idealized analytical model results with additional numerical diffusion, calculated using the conditions studied by Chu, are compared with the experimental and simulation results obtained by Chu [12].	98
Figure 5.1 – Two thermoclines that are determined separately such that they can be combined using superposition to determine the overall temperature profile when the tank inlet temperature increases with time.....	106
Figure 5.2 – Temperature vs. tank depth results after 900, 2100, 3300, and 4500 seconds for the analytical model (using 600 second time steps) and the in-house one-dimensional model (using 1 second time steps)	108
Figure 5.3 – Temperature vs. tank depth results after 900, 2100, 3300, and 4500 seconds for the analytical model (using 10 second time steps) and the in-house one-dimensional model (using 1 second time steps)	108
Figure 5.4 – Temperature vs tank depth results for the previous Case 1 conditions after 12 hours with the additional effects of heat losses to the surroundings calculated by the heat losses analytical model.....	113
Figure 5.5 - Temperature vs tank depth results for the previous Case 1 conditions after 12 hours with the additional effects of tank wall heat conduction calculated by the wall conduction analytical model.	117
Figure 5.6 – Temperature contours of the inlet jet region for the conditions studied by Nizami et al. [17] after (a) 200s, (b) 400s, and (c) 600s, showing the formation of a thermocline within the inlet jet region.	119

Figure 5.7 - Schematic of the constant temperature regions defined for time intervals 1 and 2 that are used to determine the temperature profile within the tank over time. For time interval 1, the tank is divided into 4 regions: (1) jet region, (2) inlet mixing hot region, (3) inlet mixing cold region, and (4) cold tank region. For time interval 2, the tank consists of 2 regions: (5) hot tank region and (6) cold tank region.....	120
Figure 5.8 – Description of the energy inputs and outputs for temperature region 1, the inlet jet region.	122
Figure 5.9 – Description of the energy inputs and outputs for temperature region 2, the inlet mixing hot region.	124
Figure 5.10 – Description of the energy inputs and outputs of region 3, the inlet mixing cold region.	126
Figure 5.11 – Plots of the jet penetration depth and the thermocline center depth with time showing the intersection point when time interval 1 ends. The exact time is determined by assuming linear profiles between the two closest time steps values.	127
Figure 5.12 – Temperature vs tank depth results at 10 min, 40 min, and 70 min for the low Reynolds number ($Re=1340$) case. The inlet jet mixing model results were compared with the idealized analytical model, the experimental results obtained by Oliveski et al. [18], and the results from Nizami’s quasi-1D model [17].....	132
Figure 5.13 - Temperature vs tank depth results at 15 min, 35 min, and 55 min for the high Reynolds number ($Re=8000$) case conditions. The inlet jet mixing model results are	

compared with the idealized analytical model, the experimental results obtained by Leohrke and Holzer [20], and the results from Nizami's quasi-1D model [17].	134
Figure 5.14 – Temperature vs time results at 5 different tank depths. The results of the inlet jet mixing model are compared with the idealized analytical model and the experimental results obtained by Chu [12].	136
Figure A.1 – Initial conditions and dimensions of the storage tank used for simulations to compare the semi-infinite wall solutions with the in-house one-dimensional model.	152
Figure A.2 – Temperature vs. tank depth results of the simulations using the semi-infinite wall solution and the in-house one-dimensional model after 6 and 12 hours.	152
Figure B.1 – RMS temperature errors for a) Case 1 with varying grid spacing (after 4 hours), b) Case 1 with varying time step sizes (after 4 hours), c) Case 2 with varying grid spacing (after 1 hour), and d) Case 2 with varying time step sizes (after 1 hour).	155
Figure E.1 – (a) Isometric view of the geometry used for the storage tank mesh created in ICEM, (b) Front view, (c) Top View.	181
Figure E.2 – Calculated values for the duration of time interval 1 using different values for the initial depth of Region 2, Ci , using the low Reynolds number conditions studied by Oliveski et al. [18].	184
Figure E.3 – Region 2 temperature versus time for different values of Ci using the low Reynolds number case studied by Oliveski et al. [18].	185

List of Tables

Table 3.1 – Descriptions of the energy terms used to calculate the node temperatures for the TRNSYS one-dimensional models.	32
Table 3.2 – Comparison of the TRNSYS Type 4, Type 60, and Type 534 one-dimensional model characteristics [34]. * indicates that the model includes the respective characteristic.	37
Table 3.3 – Energy equations used by the model developed by Nizami [17] to calculate the temperatures of the nodes in each of the different tank regions.	46
Table 3.4 – Comparison of correlations developed by different researchers to determine the jet penetration distance for a fluid entering a medium with a different density. ...	48
Table 3.5 – Comparison of correlations developed by different researchers to calculate the turbulent diffusivity of the fluid in the proximity of at jet of fluid.	51
Table 4.1 – Description of the cases used to study the TRNSYS one-dimensional models.	66
Table 4.2 – Water properties used for one-dimensional simulations of Case 1 and Case 2.	68
Table 4.3 – Discretizations used by the Type 60 model for each of the terms in the one-dimensional, unsteady, convection/diffusion energy equation. The Crank-Nicolson scheme was implemented for each node.	89
Table 4.4 – Numerical and simulation diffusivities calculated for the use with the analytical model to show the additional diffusion created from the numerical error in the one-dimensional models.	92

Table 4.5 – Simulation conditions used for the analytical model to replicate the conditions tested by Chu [12].	95
Table 5.1 – Tank inlet temperatures at different times used for the simulation of the varying inlet temperature analytical model.	107
Table 5.2 – Steel tank wall dimensions and thermal properties used for the tank wall heat conduction analytical model simulations.	116
Table 5.3 – Low and high Reynolds number case conditions used by Oliveski et al. [18] and Leohrke and Holzer [20] for the experiments that were used to compare with the inlet mixing analytical model.	131
Table B.1 – Equations of the trend-lines that fit the RMS error data for each of the TRNSYS models tested in Case 1 and Case 2.	156
Table E.1 – Dimensions of the geometry used for the mesh of the storage tank.	181

Chapter 1

Introduction

In order to mitigate climate change and to meet Canada's commitment to greenhouse gas reductions, there is a need for greater deployment of non-carbon based energy systems. The residential sector makes up 17% of the total Canadian energy use [1]. Of this, 82% is for space or hot water needs. Solar energy provides an alternative to natural gas or electrical resistance heating and approximately half of the residential electricity requirements in Canada could be satisfied by installing solar panels on residential buildings [2]. Moreover, it has been demonstrated that a well-designed community equipped with solar heating systems and using seasonal storage, such as the Drake Landing Solar Community (DLSC), can achieve nearly 100% of the space heating needs through solar thermal energy [3]. Careful design of these systems is needed in order to minimize capital costs while also ensuring that the desired performance is attainable. System simulation codes such as TRNSYS [4] play an important role in the design process. Sufficiently accurate models of the system components and their interactions is thus needed.

1.1 Solar Thermal Systems

A typical solar thermal domestic hot water (SDHW) system consists of solar panels, thermal storage tanks, pumps, piping, mains supply, and a household load, as shown in Figure 1.1. Solar panels are used to collect solar energy by heating a working fluid using

the solar radiation. The heat absorbed by the fluid is then transferred to a storage tank with the use of a heat exchanger or by directly sending the hot fluid into the tank.

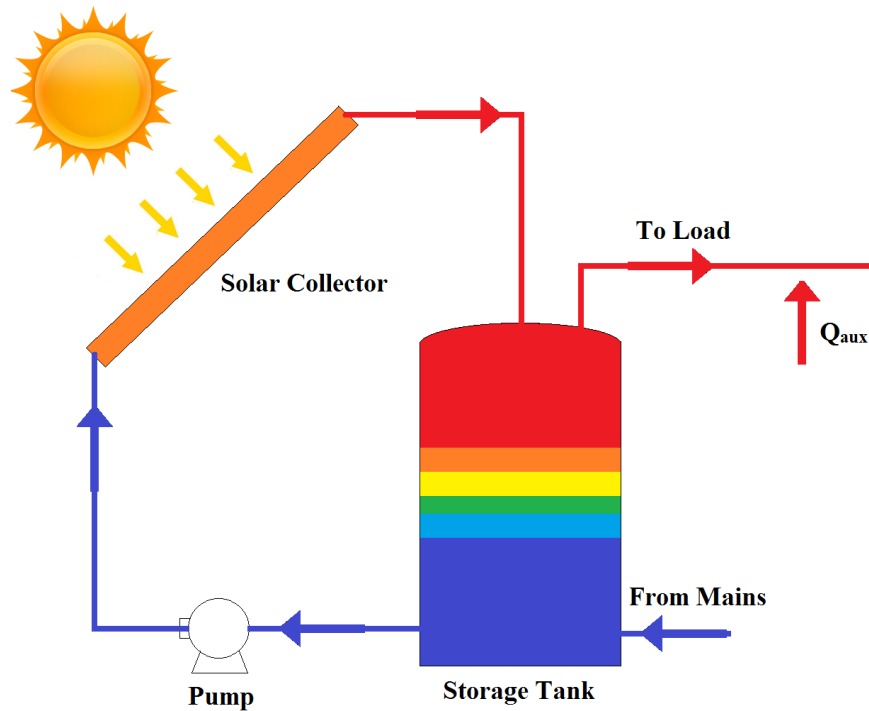


Figure 1.1 – Schematic of a solar thermal system consisting of a solar collector, a storage tank, a pump, and piping between the components as well as to the heating load and from the mains.

The storage tank initially contains a cold fluid. While the tank fills with hot fluid from the collectors, the cold fluid is pumped to the solar collector to be heated, creating a cycle. When there is a heating load, such as for space-heating or domestic hot water (DHW) requirements, hot fluid is taken from the storage tank and is replaced by cold mains fluid. These systems can also have an additional heating system to heat the fluid being sent to the load when the temperature at the output of the storage tank is insufficient for space-heating or DHW requirements.

Thermal storage is required in these systems because of the temporal mismatch between the availability of solar energy and the demand for hot water. Hot water loads are typically higher during the night time and lower during the day when there is less activity for a residential household, as shown in Figure 1.2a. However, this trend does not match with the temporal distribution of solar energy, as shown in Figure 1.2b, which shows the peak solar availability during the middle of the day. Thermal storage tanks are therefore required to store the excess solar energy collected during the day, such that it can be accessed at a later time.

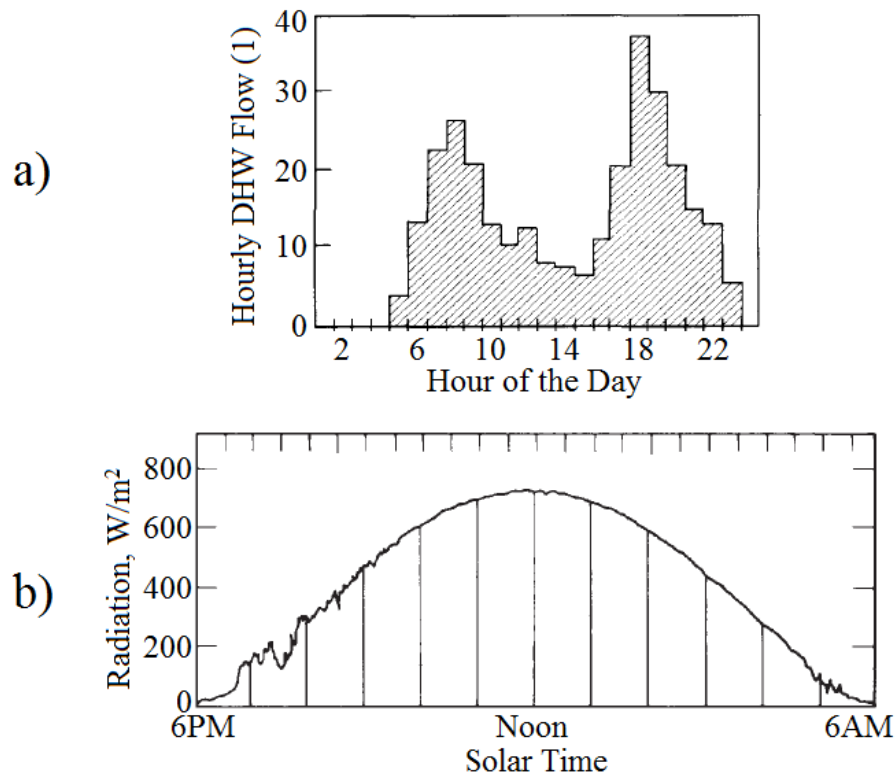


Figure 1.2 – (a) Hourly domestic hot water flow rate required by for a heating load [5],
(b) Typical available solar radiation over a 24 hour period [6].

1.2 Solar Thermal Storage Tanks

The two key operations that occur for a storage tank are charging and discharging. For a typical charging cycle, hot water from the solar collectors enters the tank through an inlet at the top. At the same time, the initial cold water leaves the tank through an outlet at the bottom and is sent to the solar collectors to be heated. The hot inlet water will remain at the top of the tank due to buoyancy effects since the hot water will have a lower density. Tank discharging occurs when cold mains water enters the tank at the bottom and the hot water leaves through an outlet at the top of the tank. This water is then sent to the load. The load outlet is located at the top of the tank to ensure the highest temperature water is extracted. These two operations can also occur at the same time as hot fluid is added from the solar collectors and simultaneously extracted to be sent to the load. Auxiliary heating may be required if the temperature of the fluid leaving the tank is below the temperature set point required by the load.

1.3 Thermal Stratification

Due to the density difference between the hot inlet fluid and the initial cold fluid during a charging cycle, thermal stratification, in which the fluid in the tank is hot at the top and cooler at the bottom, can develop [6]. During charging, a perfectly stratified tank would occur if the hot inlet fluid did not mix with the cold fluid and filled the tank with a plug flow motion. This would create a spatial temperature profile which resembled a step-function [7]. The hot region would grow as more fluid is added, and move as a plug flow in the tank, as shown in Figure 1.3. This allows for the greatest amount of energy to be

extracted from the tank when a hot water load is desired because the temperature of the water in the hot region of the tank would not change. However, this would not be possible under realistic conditions due to various mixing mechanisms and heat losses which would mix the two regions together, creating intermediate temperature regions known as the thermocline, reducing the temperature of the hot region, as shown in Figure 1.4 [8]. This represents a lower level of stratification.

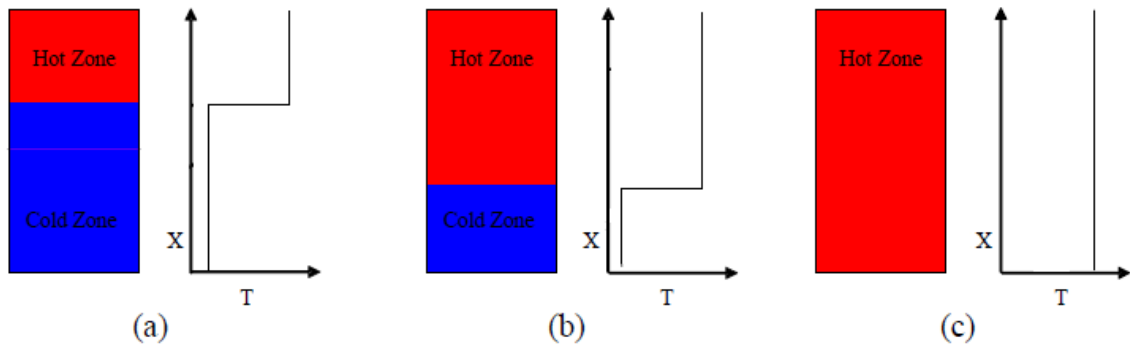


Figure 1.3 – Temperature profiles for a perfectly stratified tank at different times during charging. (a) $t = t_1$, (b) $t = t_2$, (c) $t = t_{final}$

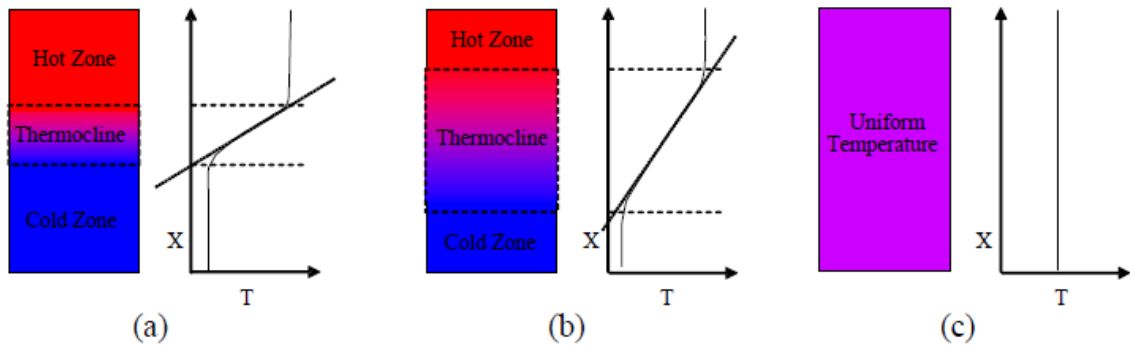


Figure 1.4 – Varying levels of stratification, (a) Moderate level of stratification with a small thermocline width, (b) Low level of stratification with a large thermocline width, (c) No thermal stratification with a fully mixed tank [8].

Figure 1.4a) represents a moderate level of stratification as only a small amount of mixing occurred between the hot and cold regions. The width of the thermocline region is

relatively small compared to the other cases. Figure 1.4b) shows a lower level of stratification as a significant amount of mixing occurred, causing the width of the thermocline to increase. Figure 1.4c) shows a fully mixed storage tank at a uniform temperature. Note that all tanks contain the same amount of thermal energy.

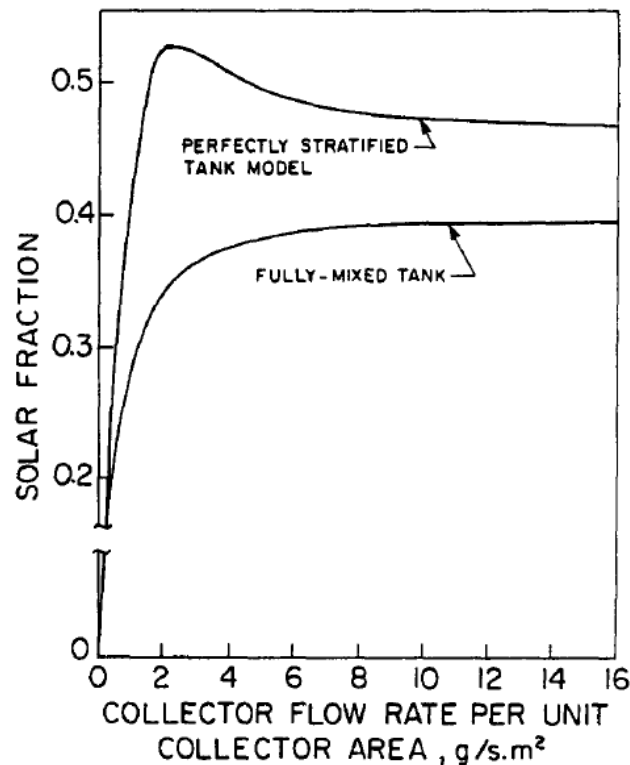


Figure 1.5 – Yearly solar fraction versus the collector flow rate for a perfectly stratified tank and a fully mixed tank [9].

A well-stratified tank is known to improve the solar thermal system performance in comparison to a well-mixed tank. Figure 1.5 shows a comparison of the expected yearly solar fraction (fraction of total energy demand supplied by solar thermal system) versus the system flow rate for a perfectly stratified tank and a fully mixed tank [9]. The higher solar fractions found for a perfectly stratified tank means that a larger portion of the energy required is supplied by the tested solar thermal system. Ideally, the storage tank would send

the highest temperature fluid possible to the load [7]. This would ensure that the same amount of energy that was put into the tank was extracted and therefore, a smaller amount of auxiliary heating would be required to meet heating load requirements. A high level of stratification would also allow for the coldest temperature fluid to be sent to the solar collectors, thus reducing collector heat losses. In contrast, a well-mixed tank would send warmer fluid to the collector, which increases collector losses. These two effects act to reduce the overall system efficiency in comparison to a stratified tank.

1.4 System Simulation Modelling

Numerical simulation of a thermal storage tank design is often necessary to assess how it will perform over time under different conditions. This can be done with the use of three-dimensional CFD models. These models are able to obtain fine details about the performance of the storage tank, such as flow patterns and temperature profiles at different locations and times. This is useful for comparing different storage tank designs, such as done by Shaarawy [10]. Multiple tank designs were compared, with the use of ANSYS CFX, which contained different baffle arrangements. The simulations were used to show the flow patterns created within the tanks and to determine which design created the highest level of stratification.

However, these three-dimensional models can be computationally expensive due to the large number of nodes required to accurately predict the velocity and temperature profiles. As such, this approach is not suitable for system simulations which are used to

predict the long term performance of a system consisting of multiple components. Therefore, simpler models of the components are required.

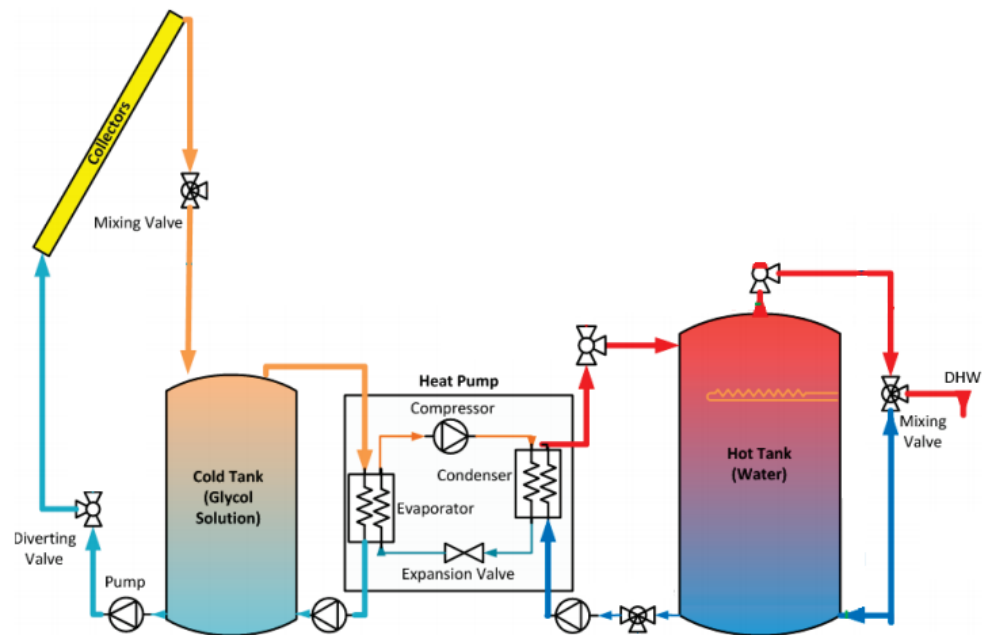


Figure 1.6 – Components of a solar thermal system studied by Chu [12] consisting of collectors, cold and hot storage tanks, and a heat pump.

TRNSYS [11] is a commonly used transient system simulation tool that contains a large variety of different component models (or Types) that can be combined into a single simulation. Figure 1.6 shows an example of a solar thermal system that was simulated previously by Chu [12]. Individual models for each of these components were connected and simulated together to determine the performance of this system over a long period of time. The data input for this simulation was a set of weather data, used for the collector model, and the demand load profiles. The inputs for the other models would therefore depend on the outputs of the solar collector model. A glycol solution was used as the

working fluid for the collectors and the cold storage tank. Water was used for the hot storage tank such that it could be used to be sent to the load.

The challenge with using simplified models for storage tanks is that they are not as accurate as the three-dimensional models and are not able to obtain finer details about the flow within the tank. Generally, the simplified models solve the one-dimensional thermal energy equation using an assumed flow pattern. Chapter 3 will present various simple modelling strategies for storage tanks that are used to obtain the most accurate solutions possible while keeping computational time low to allow for incorporation into the larger system simulations.

1.5 Problem/Motivation

The topic of this thesis was motivated by simulation results obtained by Chu [12]. In addition to the simulations of the solar thermal system shown in Figure 1.6, Chu also performed separate simulations for the hot storage tank to validate the TRNSYS storage tank model that was used. This was done by comparing the simulation results with experimental results from the same system.

The hot storage tank was simulated together with the heat pump, as shown in Figure 1.7, to ensure that the temperature of the water entering the hot tank was the same as in the experiments. Data collected from experiments for the temperature and flow rate of the glycol solution leaving the cold tank was used as an input for the heat pump model. The initial temperature of the water in the tank was 20°C and the flow rate of the water entering the tank during a charging cycle was about 3 L/min .

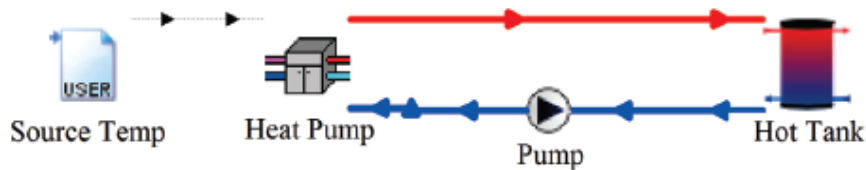


Figure 1.7 – TRNSYS visualization of the component models used to simulate the conditions studied by Chu [12] to determine the accuracy of the hot storage tank model.

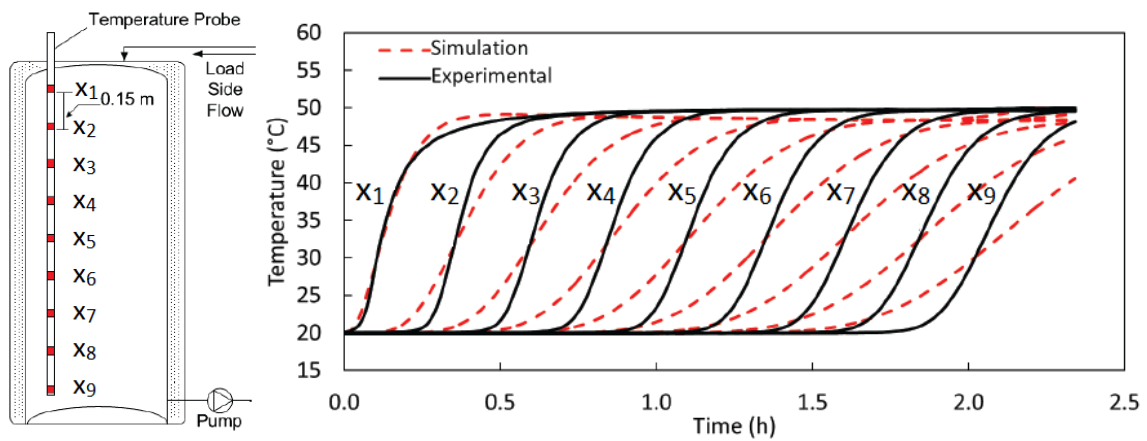


Figure 1.8 – LEFT: Storage tank thermocouple positioning used to determine the experimental temperature profiles, RIGHT: Simulation and experimental temperature profile results obtained by Chu [12].

The TRNSYS one-dimensional model results did not match the experimental data. Figure 1.8 shows the temperature versus time results at 9 different locations along the height of the tank. The profiles representing the simulation results showed a much lower level of stratification compared to the experimental data. This was not expected because the TRNSYS storage tank model simplifies the flow such that it neglects some of the mixing mechanisms that can occur in an actual storage tank. Therefore, they should output temperature profiles that show a higher level of stratification.

This problem was also experienced with TRNSYS simulations performed by Baldwin and Cruickshank [13]. The results predicted more mixing within the tank in comparison to the experiments. Further analysis performed by Baldwin revealed that the error was reduced by increasing the number of nodes used for the model. However, the improvement experienced when the amount of nodes was increased was very small. Therefore, the number of nodes would likely need to be increased to a much larger value before the error was significantly reduced.

1.6 Objective and Approach

The objective of the current research was to investigate the reasons why the TRNSYS models used in Chu's research did not provide accurate temperature profile results compared to the experiments. This was done by creating two simple case studies that outlined the key heat transfer and flow mechanisms that occur within a thermal storage tank. The first case involved conduction between the hot and cold regions of an initially perfectly stratified tank while there was no flow in or out. The second case considered typical charging conditions where the tank was initially filled with a cold fluid and hot fluid entered from an inlet at the top of the tank. These cases were simulated using three different TRNSYS models and compared with an idealized analytical solution.

An investigation of the governing equations was also performed to derive an expression for the amount of numerical error that occurred with the TRNSYS models for varying simulation parameters, such as the number of nodes and time step size. A Taylor series expansion was performed on all of the discretized terms of the one-dimensional

convection/diffusion energy equation. This also helped to determine the simulation parameters that would be required to significantly reduce the error between the simulation and analytical results.

In addition to the analysis of the TRNSYS storage tank models, new modelling techniques were developed that improve on the TRNSYS results. These were grid-less models that used analytical solutions to determine the temperatures at different locations and times. Different techniques were developed to account for the additional mixing mechanisms that can occur within a storage tank. Some of which are not considered by the TRNSYS models.

1.7 Outline of Thesis

This thesis is divided into four main sections including a review of the literature on thermal storage tanks, an overview of some of the commonly used storage tank models developed by various researchers, an analysis of the TRNSYS one-dimensional storage tank models, and the development of the analytical modelling techniques.

Chapter 2 is a review of the literature involving the design of thermal storage tanks. It includes a study of the main causes that lead to mixing within a storage tank and methods that different researchers have proposed to reduce this. The key dimensionless groupings that are commonly used to help define the level of stratification in a storage tank have also been shown.

Chapter 3 gives an overview of some of the simple storage tank models that are used for long-term system simulations. The TRNSYS one-dimensional models used for

this research are discussed, as well as a quasi-one-dimensional model developed to account for inlet jet mixing. Finally, two different plug flow models are described which allow for movement of the one-dimensional nodes to track the location of the thermocline.

Chapter 4 involves a numerical analysis of the TRNSYS one-dimensional storage tank models. Two different case studies were simulated to determine the conditions that lead to an unacceptable amount of numerical error. A Taylor series expansion also gives a representation of this numerical error and how the simulation parameters can be changed to obtain a more accurate result.

Finally, Chapter 5 shows the development of different analytical modelling techniques that are able to simulate the ideal performance of a storage tank with more accuracy than the TRNSYS models. Each of the techniques consider different heat loss and mixing mechanisms that occur in an actual storage tank. The results of each of the models were compared with either experimental data or results obtained from an in-house one-dimensional model.

Chapter 2

Thermal Storage Tank Behaviour

This chapter provides an overview of the performance of thermal storage tanks. The importance of obtaining a high level of thermal stratification is discussed. The heat transfer and mixing mechanisms that act to reduce the level of stratification have also been examined.

2.1 Thermal Stratification in Storage Tanks

Obtaining a high level of stratification in a thermal storage tank can contribute to an increase in the performance of a solar thermal system. Figure 2.1 shows a control volume surrounding an entire solar thermal system to observe the energy input and outputs. The energy entering the system comes from the solar energy from the sun, the mains water entering the tank, and electrical energy to run the pump (which is neglected for this analysis). Energy leaves the system as fluid is delivered to the load, from heat losses out of the tank, and from solar collector losses.

The solar fraction is defined as the ratio of the energy provided to the load by the solar thermal system and the load requirements. This is calculated by dividing the energy delivered to the load by the solar thermal system, $Q_{solar\ to\ load}$, by the total energy required by the load, Q_{load} , as shown by Eq. (2.1).

$$f = \frac{Q_{solar\ to\ load}}{Q_{load}} \quad (2.1)$$

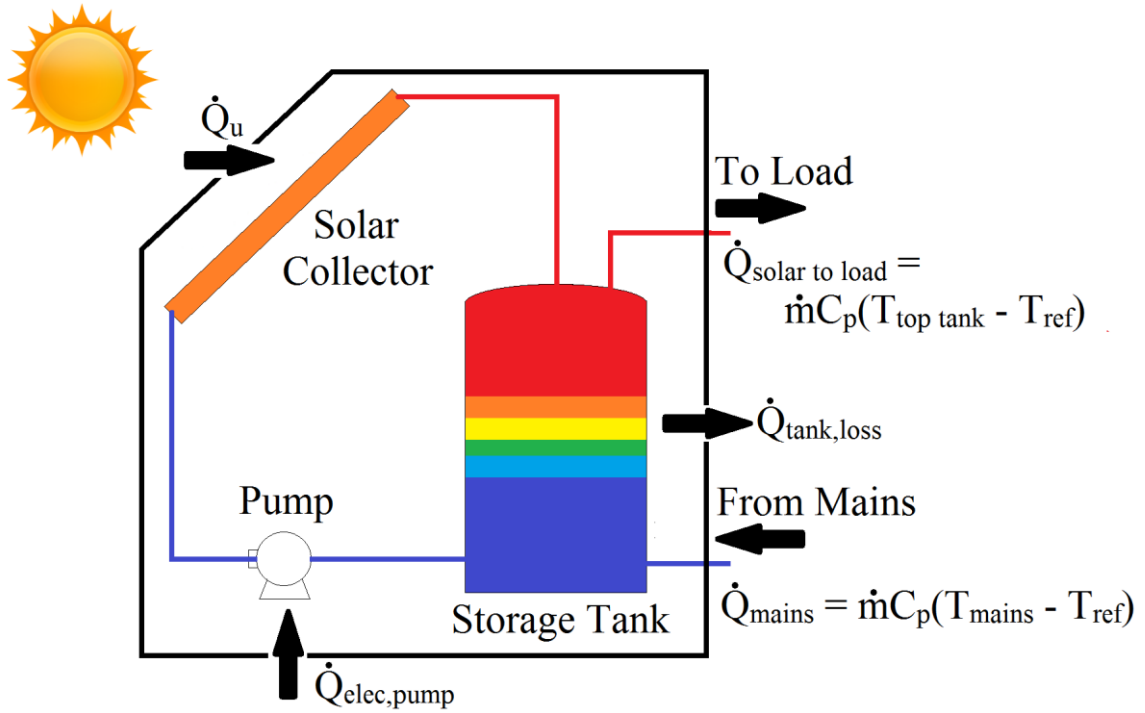


Figure 2.1 – Energy inputs and outputs for the overall solar thermal system.

The energy delivered by the system would depend on the temperature of the fluid at the top of the tank, as given by Eq. (2.2). Therefore, a higher solar fraction would be obtained if the temperature of the fluid at the top of the tank was high. When there is a lower level of stratification, the temperature of the fluid in the hot region would decrease, leading to a lower solar fraction since more auxiliary energy would be required to heat the outlet fluid to a useable temperature.

$$Q_{solar\ to\ load} = \int \dot{m} C_p (T_{top\ tank} - T_{ref}) dt \quad (2.2)$$

The level of stratification also effects the performance of the solar thermal collectors. The performance of the collector can be modeled with the Hottel-Whillier equation, Eq. (2.3), as used by Wuestling et al. [14]. This equation gives the rate of useful

energy gain from solar energy, Q_u , where A_c is the collector area, $F_R(\tau\alpha)$ is the intercept of the collector efficiency versus $(T_i - T_a)/G_T$ curve, G_T is the solar radiation per unit area incident on the collector plane, $F_R U_L$ is the negative of the slope of the collector efficiency versus $(T_i - T_a)/G_T$ curve, T_i is the collector inlet temperature, and T_a is the ambient temperature.

$$Q_u = A_c [F_R(\tau\alpha)G_T - F_R U_L(T_i - T_a)]^+ \quad (2.3)$$

This shows that the temperature of the fluid that enters the inlet of the solar collector, T_i , affects the performance of the collector. If T_i increases, the heat losses from the collector increase, which decreases the energy collected. Therefore, it is beneficial to keep the temperature of the fluid at the bottom of a storage low. With a lower level of stratification, the temperature of the fluid in the bottom tank region would increase, leading to a lower collector efficiency.

The following sections will discuss some of the major causes that act to reduce the level of stratification in a thermal storage tank. These can lead to additional mixing of the fluid inside the tank or heat losses of the hot fluid stored in the tank.

2.1.1 Inlet Jet Mixing

Inlet jet mixing is created as a result of the fluid entering the tank during charging or discharging. During charging, the tank initially contains cold fluid and a hot fluid would be introduced at the top with a flow rate equal to that of the fluid passing through the collectors. Since the tank fluid is initially stationary, the discontinuity in the velocity creates a zone of turbulent mixing [15]. The jet of fluid becomes turbulent at a short distance from

the inlet to the tank. Moreover, the adjacent, initially stagnant cold fluid will be entrained into the jet of hot fluid [16], as shown in Figure 2.2, causing an increase in the width of the turbulent mixing zone downstream from the inlet.

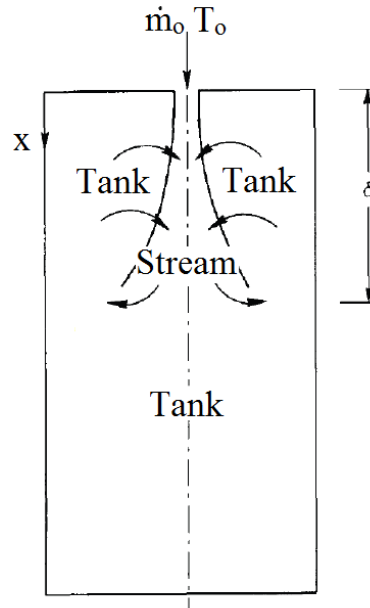


Figure 2.2 – Schematic of a storage tank showing the inlet jet mixing as the initial tank fluid is entrained into the jet stream [19]

The nature of the mixing will depend on the alignment of the buoyancy forces with the jet momentum. If the fluid entering the tank is hotter than the fluid adjacent to the inlet, the buoyancy force will direct the fluid upwards, thus opposing the momentum of the flow. This is known as a negative buoyant plume because the buoyancy forces that act on the inlet fluid and the momentum are in opposite directions. These types of flows have been studied by Nizami et al. [17] and Oliveski et al. [18]. As the jet penetrates deeper into the tank, the fluid will lose momentum as it mixes with the stagnant fluid.

Experimental data collected by Oliveski et al. [18] and Loerhke and Holzer [20] give examples of the effect that inlet jet mixing can have on the temperature profiles. Figure 2.3 shows experimental results from Oliveski et al. for a thermal storage tank that was initially at a temperature of 24.5°C and was charged at a constant flow rate ($Re = 1340$) with water entering at the top of the tank at 39.9°C . Thermocouples were positioned along the tank height close the wall to record the temperatures at different tank levels with time. The results showed a slightly different thermocline development than expected from a typical plug flow within the tank. It took a certain amount of time before the temperature of the water at the top of the tank reached the inlet water temperature. This occurred due to the inlet jet penetrating to a certain depth and creating a re-circulation zone that mixed the inlet fluid with the cold fluid that was initially in tank, as shown in the velocity vector plots in Figure 2.4.

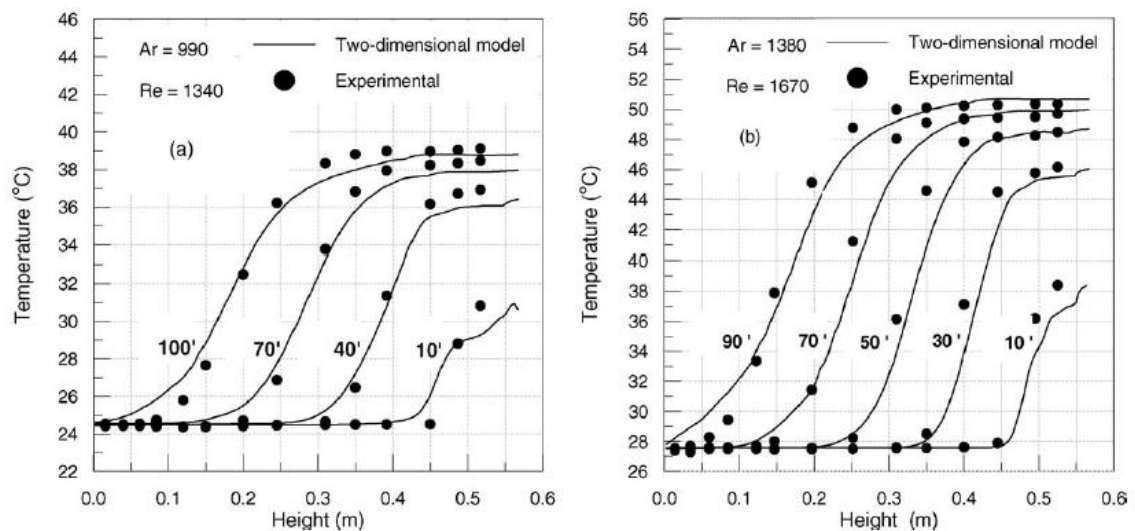


Figure 2.3 – Experimental temperature profile results obtained by Oliveski et al. [18] showing an increasing temperature at the top of the tank for two different cases at different times during the simulation (LEFT: 10, 40 70 and 100 minutes; RIGHT: 10, 30, 50, 70, and 90 minutes).

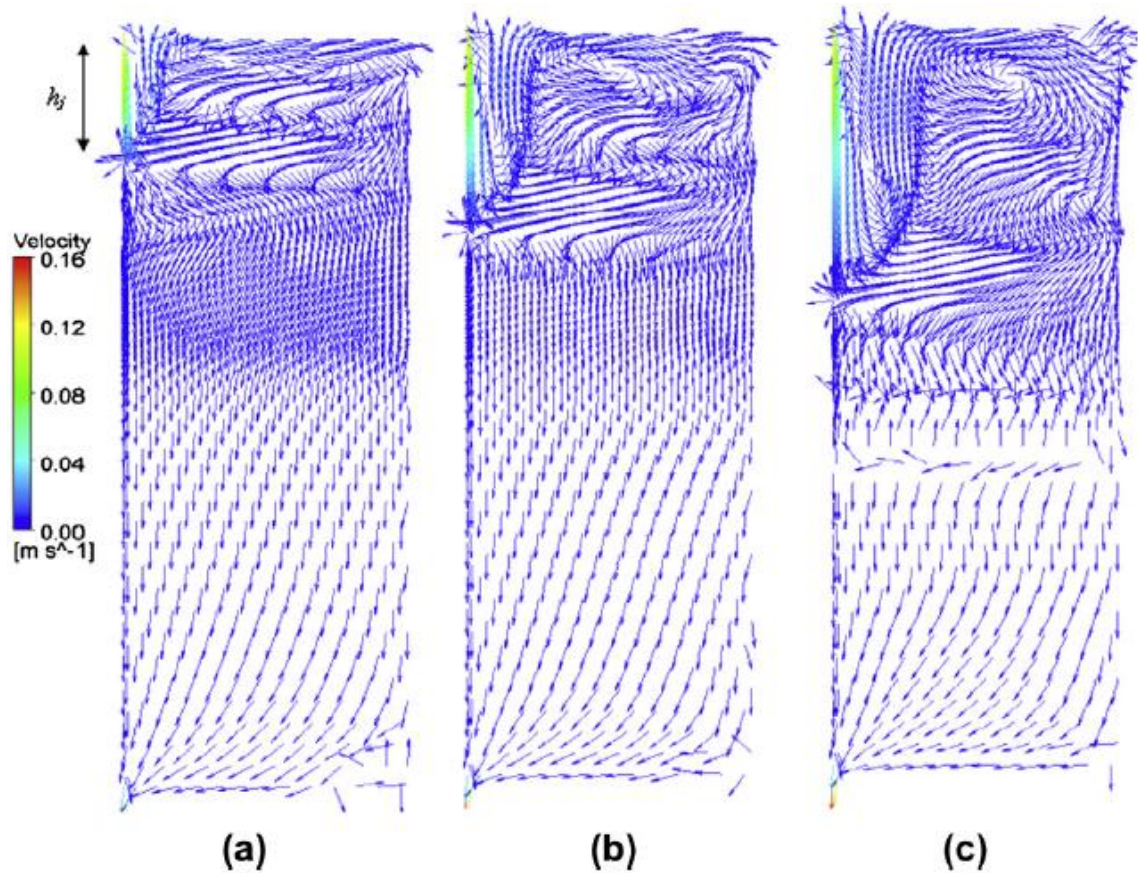


Figure 2.4 – Velocity vectors after (a) 10 min, (b) 40 min, and (c) 70 min predicted with CFD showing the inlet jet penetration depth and varying velocity patterns within the tank [17].

Many different researchers have developed methods to decrease the mixing that arises from the inlet jet penetration. Shah and Furbo [21] and Shaaraway [10] analyzed the entrance effects in solar thermal storage tanks with the use of baffles positioned in front of the inlet pipe. Results from simulations done by Shah and Furbo, Figure 2.5, show that a higher level of stratification was obtained with the use of large, flat baffles. This occurred because the baffles acted to reduce the incoming axial momentum of the fluid as it was redirected to the edges of the tank instead of penetrating down the center. Therefore, the inlet fluid does not mix as much with the cold tank fluid. Similar results were obtained with

the use of inlet diffusers, as shown by Zurigat et al. [22] and Chung et al. [23]. Different diffuser designs have been researched that distribute the inlet fluid flow over a much larger cross-sectional area. This reduces the depth the inlet fluid penetrates and prevents some of the mixing with the initial tank fluid.

Plume entrainment occurs when cooler fluid with a higher density enters the top of the tank with a lower density fluid, the inlet fluid will fall until it reaches a level in the tank that contains fluid with the same density [24]. This is described as a positive buoyant plume since the buoyancy and momentum forces are in the same direction. This typically occurs when a tank is being charged later in the day when there is less solar energy available. The fluid that is pumped through the collectors is not heated to as high of a temperature and is then sent to the top of the tank that is at a higher temperature from previous charging. This results in additional mixing as the cooler fluid falls through the higher temperature layers within the tank. The falling fluid will cool the hotter temperature regions and reduce the level of stratification.

Methods for preventing mixing due to plume entrainment have been developed. Different inlet stratifier designs were researched by Shah et al. [25] and Andersen et al. [26]. These stratifiers distribute the inlet flow to the level within the tank that has the same temperature. Shah et al. analysed the effects of a rigid pipe inlet stratifier with multiple outlets and Andersen et al. developed a fabric stratification pipe.

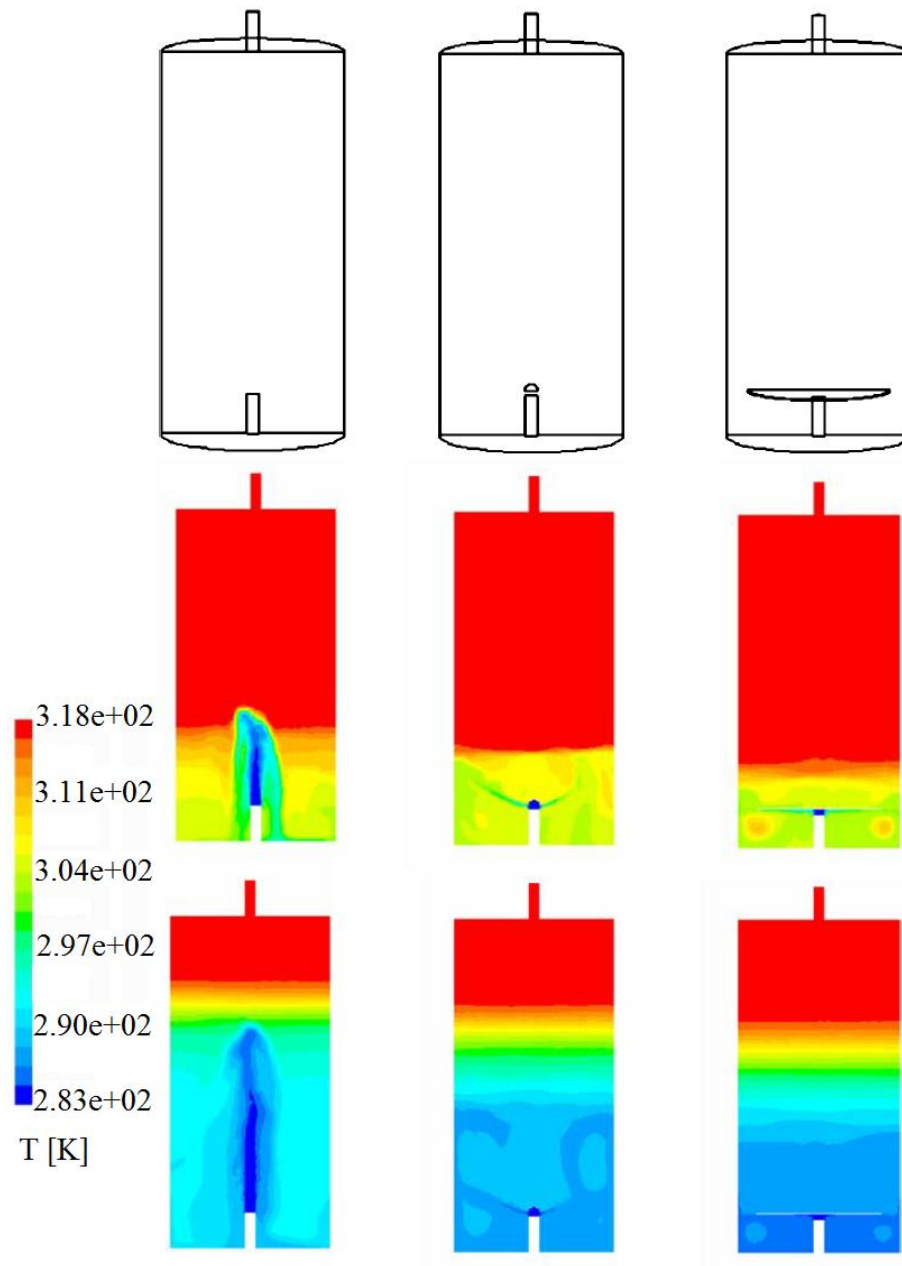


Figure 2.5 – Different inlet baffle designs tested by Shah and Furbo [21] and numerical results for tank discharging at 2 different times. LEFT – Raw pipe entering tank, MIDDLE – Metro, hemispherical baffle plate above inlet pipe, RIGHT – Large baffle plate above inlet pipe.

In conclusion, the additional mixing that is created by the inlet fluid jet can have a large effect on the level of stratification within the tank. The penetration of the inlet jet

causes entrainment with the surrounding fluid that is initially in the tank. Different researchers have developed storage tanks with baffles and diffusers that reduce the axial momentum of the inlet jet by spreading the inlet flow over a larger cross-sectional area. This helps to create more of a plug flow motion that reduces the amount of mixing with the initial tank fluid.

2.1.2 Fluid Conduction

Conduction occurs along the interface between the hot and cold temperature regions within the tank. Over time, energy will be diffused from the hot region to the cold region, which acts to thicken the thermocline region. Jaluria and Gupta [27] and Lavan and Thompson [28] studied the effects of the fluid conduction on the stratification in thermal storage tanks. Jaluria and Gupta performed experiments on storage tanks that were initially well stratified and allowed to cool with time. The temperature profiles plotted in Figure 2.6 show that the width of the thermocline increases as time increases. Temperatures of the isothermal hot region at the top of the tank decreased due to heat losses to the tank surroundings, but the main cause of the energy transfer between the hot and cold regions and the thermocline was the thermal diffusion.

This fluid conduction is similar to the behaviour of a semi-infinite wall being heating with a constant temperature boundary [29]. Over time, heat is diffused into the wall and the temperature will increase until it reaches a constant temperature, as shown in Figure 2.7. This is similar to what occurs along the interface between the hot and cold regions within a storage tank. The temperature at the center of the thermocline remains the same

with time as heat is diffused between the two regions. This comparison can be used to analytically predict the tank temperature profile for simple cases, as will be explored in the following chapters.

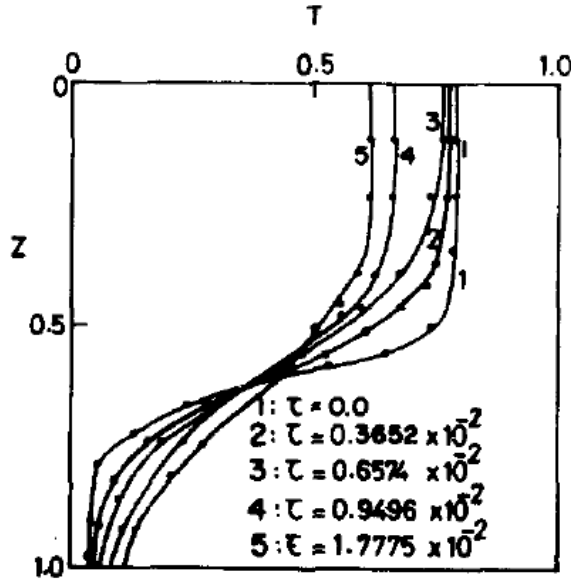


Figure 2.6 – Temperature profiles at different times showing an increasing thermocline width due to conduction between the hot and cold regions [27]

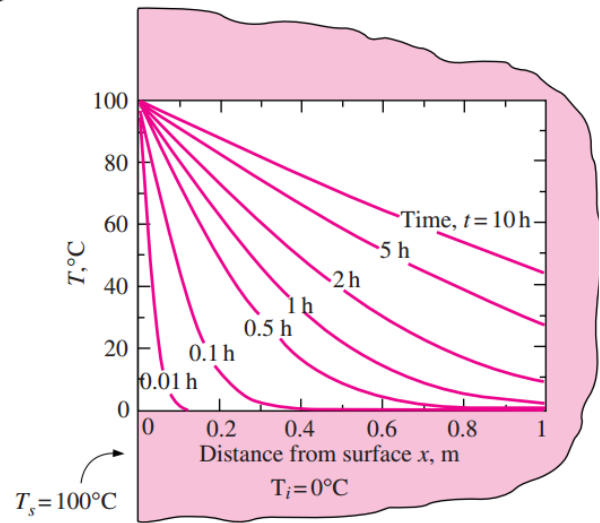


Figure 2.7 – Temperature profiles at different times showing the conduction of heat through a solid determined by the semi-infinite wall solution [29]

2.1.3 Tank Wall Heat Conduction

Axial heat conduction along the tank walls can also act as a mechanism for reducing stratification. The metals that are typically used for tank walls have a higher conductivity than water, which augments the axial heat conduction [19].

Lavan and Thompson [28] showed experimentally that the extraction efficiency (defined as $\eta = \dot{Q}t^*/V$ where t^* is the time at which the initial inlet-exit temperature difference, ΔT , has dropped to a 10 per cent drop of the initial ΔT , \dot{Q} is the volume flow

rate, and V is the tank volume) calculated for a tank that was constructed with steel was only 90%, which was lower than the efficiency obtained from a tank constructed with plexiglass (97%). This was the result of heat being transferred through the tank walls at a higher rate. It was concluded that better performance could be obtained with the use of a tank that was made out of an insulating material. Abdoly and Rapp [30] found similar results and stated that the wall heat transfer and heat losses to the surroundings can have a large effect on the overall temperature profile.

A methodology for determining the importance of wall heat conduction was provided by Lightstone [19]. Dimensionless groupings were developed to determine how the wall conductivity compares with other heat transfers within the tank. The first relates the rate of energy transferred down the wall to the rate of heat transfer by convection. Therefore, if the dimensionless group shown in Eq. (2.4) is much smaller than one, it can be said that the wall conduction has a very small effect on the stratification within the tank.

$$\frac{\dot{Q}_{cond,wall}}{\dot{Q}_{conv,fluid}} = \frac{k_{wall}A_{c,wall}}{\dot{m}C_{p,fluid}L} \ll 1 \quad (2.4)$$

The second dimensionless group compares an estimate of the heat transfer at the interface with the rate of heat transfer by convection in the tank fluid. For this comparison, the wall is treated as a fin in order to estimate the heat transfer. This assumes that the heat transfer coefficient is constant at the wall, the temperatures in regions 1 and 2, shown in Figure 2.8, are uniform, and the temperature of the wall is equal to the average in the thermocline. Therefore, the heat transfer to the wall would be given by Eq. (2.5).

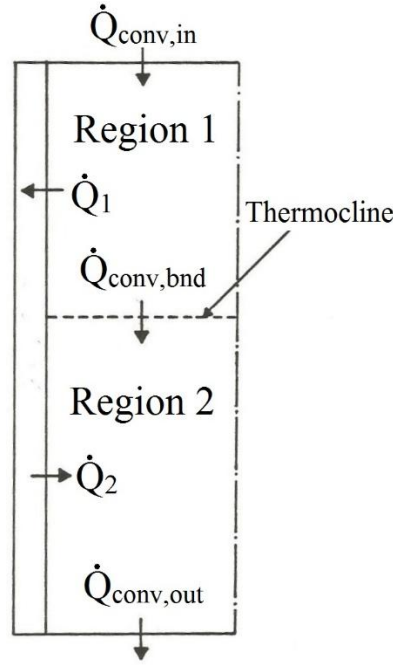


Figure 2.8 – Schematic of wall heat conduction showing heat entering the wall from the hot fluid region (Region 1) and leaving into the cold fluid region (Region 2) [19].

$$\dot{Q}_1 = \sqrt{hPk_{wall}A_{c,wall}} \frac{\Delta T}{2} \tanh \left(\sqrt{\frac{hP}{k_{wall}A_{c,wall}}} \frac{L}{2} \right) \quad (2.5)$$

Therefore, the dimensionless group is given in Eq. (2.6). Similar to the previous case, if this number is much smaller than one, the heat transfer transferred through the wall will be much smaller than the heat transfer in the fluid and would not have a significant effect on the stratification within the tank.

$$\frac{|\dot{Q}_1| + |\dot{Q}_2|}{\dot{Q}_{conv,fluid}} = \frac{\sqrt{hPk_{wall}A_{c,wall}} \tanh \left(\sqrt{\frac{hP}{k_{wall}A_{c,wall}}} \frac{L}{2} \right)}{\dot{m}C_{P,fluid}} \quad (2.6)$$

2.1.4 Heat Losses to Surroundings

Typical thermal storage tanks will have insulation within the walls of the tank to prevent energy loss to the surroundings which would lead to a decrease in the water temperature. However, even with the use of insulation, a significant amount of heat can be lost to the surroundings when storing high temperature fluid over long periods of time. This can become important when storage tanks are used to store hot fluid overnight.

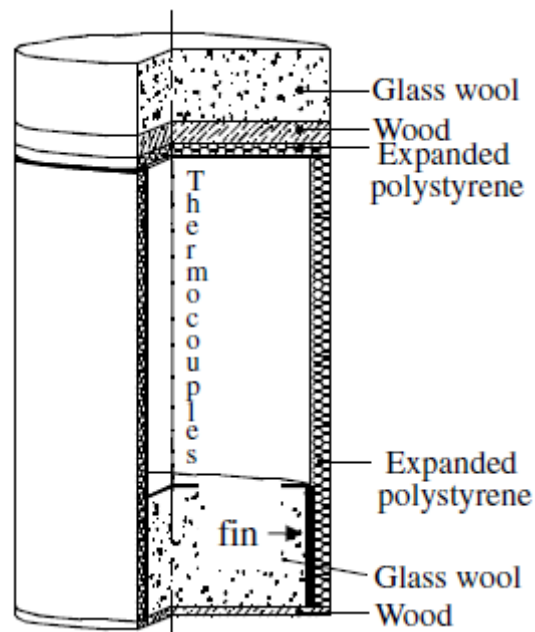


Figure 2.9 – Schematic of the thermal storage tank used by Oliveski et al. [18] to study the temperature profiles with time with the effects of heat losses to the surroundings.

Oliveski et al. [18] and Abdoly and Rapp [30] performed experiments to determine the amount of heat loss that occurred with the use of an insulated storage tank and how it affected the temperature profiles within the tank over time. A stainless steel tank, as shown in Figure 2.9, was used by Oliveski et al., which consisted of different types of insulation in each wall. Fourteen thermocouples were positioned along the central axis of the tank.

The experiments consisted of a storage tank that was initially at uniform temperatures of 51.5, 72.5, and 82°C. Cooling was allowed to occur over 15, 60, and 45 hours respectively and the ambient temperature was 17.3°C.

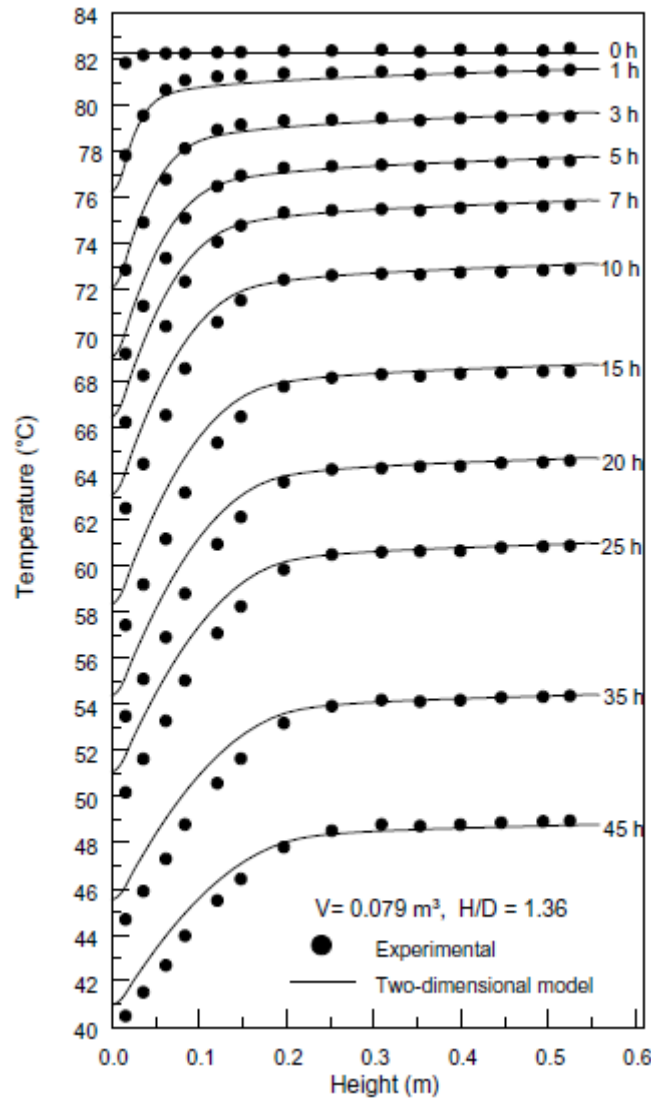


Figure 2.10 – Temperature profile results obtained by Oliveski et al. [18] showing the decrease in the temperature of an initially constant temperature tank with time as a result of the heat losses to the surroundings. Due to natural convection, colder fluid falls to the bottom of the tank.

Figure 2.10 shows the temperature profiles within the tank for the third case. At each time, the average temperature across the entire tank decreased as heat was lost to the surroundings. The results also showed that the temperature of the water at the bottom of the tank was lower than the water at the top of the tank at later times, which was a result of natural convection. Heat losses to the surroundings caused the temperature of the fluid in the near wall region to decrease, but fluid in the center of the tank was still at a higher temperature. Therefore, due to buoyancy forces, the cooled fluid near the walls falls, creating a cooler fluid region at the bottom of the tank. This process creates stratification within the tank as the hot fluid remains at the top of the tank and the cold fluid falls to the bottom.

These results show that heat losses to the surroundings can lead to significant changes in the temperature profiles that need to be considered in simulation models. However, the time scale of this phenomenon is much larger than the charging/discharging time of a storage tank, which can typically be 1-2 hours, depending on the size of the tank and the flow rate. Therefore, the heat losses to the surroundings may not significantly change the results during charging or discharging as the effects of other mixing mechanisms would be more dominant.

2.2 Dimensionless Numbers

There are a few different dimensionless groupings that arise from the analysis of thermal storage tanks that help to determine how a tank will perform. Each of these groupings help determine the behaviour of the fluid under different conditions, such as the

temperature difference and the fluid flow rate. The main dimensionless numbers are given below.

$$Ri = \frac{\text{Buoyancy Forces}}{\text{Inertial Forces}} = \frac{g\beta(T_{in} - T_{initial})H}{u_{in}^2} \quad (2.7)$$

$$Re = \frac{\text{Inertial Forces}}{\text{Viscous Forces}} = \frac{u_{in}D}{\nu} \quad (2.8)$$

$$Gr = \frac{\text{Buoyancy Forces}}{\text{Viscous Forces}} = \frac{g\beta(T_{in} - T_{initial})H^3}{\nu^2} \quad (2.9)$$

$$Fr = \frac{\text{Inertial Forces}}{\text{Gravitational Forces}} = \frac{u_{in}}{\sqrt{gH}} \quad (2.10)$$

The Richardson number, given by Eq. (2.7), is often used to predict the level of stratification that would be observed under certain conditions [28]. Generally, H represents the height of the tank. However, if the tank inlet and outlets are not at the top and bottom, H would be the vertical distance between the inlet and outlet pipes. The variable T_{in} is the temperature of the inlet fluid, $T_{initial}$ is the temperature of the fluid initially in the tank before charging/discharging, U_{in} is the velocity of the fluid entering the tank, and β is the thermal expansion coefficient of the fluid. The Richardson number determines the ratio between the buoyancy and inertial forces. If the Richardson number of the fluid entering the tank is large, a higher level of stratification would be expected because there would be lower inertial forces compared to the buoyancy forces. Therefore, the inlet jet would not penetrate as deep, which would reduce the amount of mixing.

Experiments performed by Holzer et al. [31] on a tank with an inlet at the top of the tank and an outlet at the bottom revealed that in order to achieve a high level of stratification, a Richardson number of at least 4.7 was required. This was slightly larger than the value obtained by Zurigat et al. [32], who proposed that stratification was not affected by the inlet conditions when Richardson number was 3.6 for a horizontal storage tank.

Other commonly used dimensionless groupings are the Reynolds number, which shows how the inertial forces compare with the viscous forces, the Grashof number for the ratio between the buoyancy and viscous forces, and the Froude number, which compares the inertial and gravitational forces. These numbers are most commonly used to indicate the characteristics of the inlet flow since it has a large effect on the tank stratification.

2.3 Summary

This chapter has explored different aspects of solar thermal systems while emphasizing the importance of the storage tanks. Storage is required in order to store excess thermal energy during the day such that it can be accessed at times where less solar energy is available. The design of these tanks is important because there are many causes of mixing, such as inlet jet mixing, fluid conduction, tank wall heat conduction, and heat losses to the surroundings, which lead to a loss of stratification and a decrease in the overall solar thermal system performance.

Chapter 3

Thermal Storage Tank Models for System Simulation

This chapter outlines some of the commonly used models for simulating the temperature profile within thermal storage tanks. Since three-dimensional modelling is not desired for long-term system simulations, these are simplified models that reduce the amount of computation. One-dimensional modelling techniques are shown as well as models that use a plug flow assumption.

3.1 One-Dimensional Multi-Node Models

System simulation codes, such as TRNSYS, typically approximate the temperature profiles in the tank as one-dimensional with no radial variation in temperature. These models thus discretize the problem into a set of one-dimensional, isothermal nodes along the height of the tank. A fully mixed tank is represented by a single node. As more nodes are used, a higher level of stratification can be simulated as more temperature layers are calculated [11]. This section reviews some of the one-dimensional models that have been previously developed.

3.1.1 TRNSYS One-Dimensional Models

TRNSYS contains a variety of different thermal storage tank models (also known as Types in TRNSYS). Most of these, such as Type 4, Type 60, and Type 534, are one-dimensional models. Figure 3.1 shows the set of n tank nodes and how they are arranged by the models to simulate the temperature distribution within the tank. Some of the models

allow for varying node sizes, Δx , that can be specified by the user. The single node shown in Figure 3.2 outlines the main energy flows that are calculated by the models for each time step. Descriptions for each of the terms in the energy balance are shown in Table 3.1.

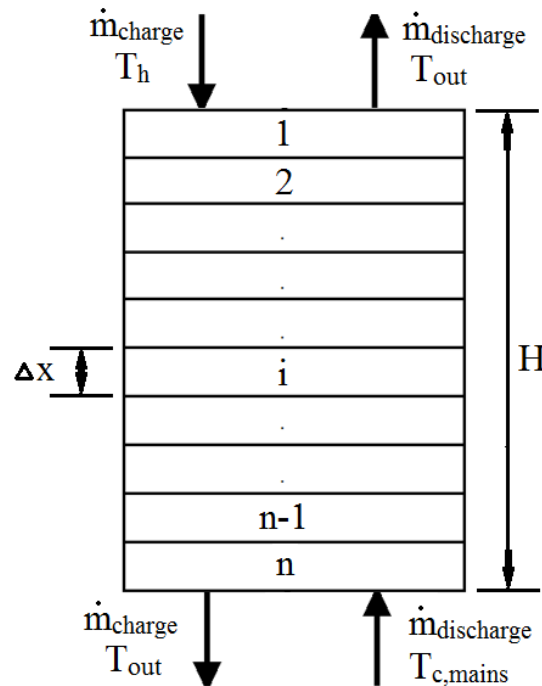


Figure 3.1 – One-dimensional node discretization of a thermal storage tank use by the TRNSYS models.

Table 3.1 – Descriptions of the energy terms used to calculate the node temperatures for the TRNSYS one-dimensional models.

Term	Description
$\dot{m}_{in} C_p (T_{in})$ or $\dot{m}_{out} C_p (T_i)$	Heat flow entering the tank from the solar collector or being delivered to the load. These terms are only used for the node that is specified as the inlet or outlet of the tank.

$\dot{m}_{\text{up}} C_p T_i$ or $\dot{m}_{\text{down}} C_p T_{i-1}$	Mass flow out of node i and into node $i - 1$ or the mass flow entering node i from node $i - 1$. The mass flows entering and leaving a node boundary are summed together at the beginning of each time step and used for the calculations.
$\frac{k + \Delta k}{\Delta x} A_c (T_{i-1} - T_i)$	Conduction of between the previous node and node i . Δk can be specified separately by the user to account for other conduction factors such as tank wall heat conduction.
$(U + \Delta U) A_s (T_{\text{env}} - T_i)$	Heat losses from the fluid in node i to the environment.
$UA_{\text{hx}} LMTD$	Heat flow into node i from an internal heat exchanger. The user specifies the dimensions of the heat exchanger, the temperature, and the flow rate of the fluid. Conductivities are also specified to account for heat exchanger material and walls. $LMTD$ is the log mean temperature difference between the tank fluid temperature and the fluid in the heat exchanger.
Q_{aux}	Heat input from an optional auxiliary heater. The location of the heaters can be specified by the user to deliver heat to any node within the tank.

Newton [33] developed a method used to account for heat conduction through the tank walls by calculating the total heat transfer as the sum of the fluid heat transfer and the wall conduction for a one-dimensional model. This assumes that the tank wall and the fluid are at the same temperature at each node location.

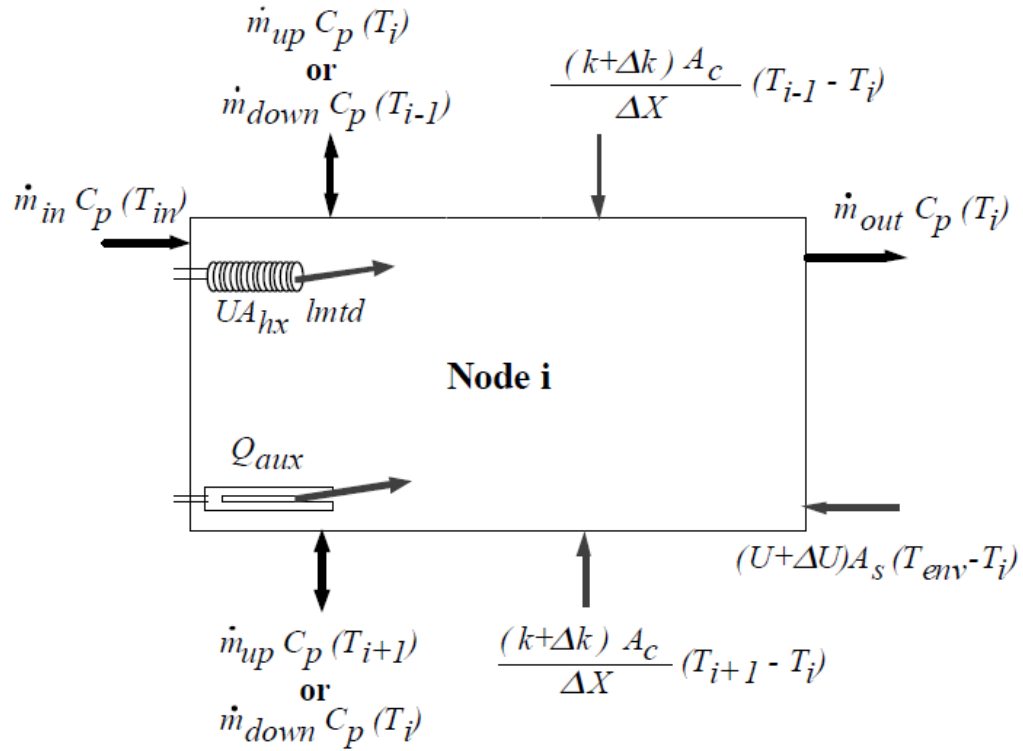


Figure 3.2 – Energy flows into and out of each node used to calculate the node temperatures for the TRNSYS one-dimensional models [33].

$$\begin{aligned}
 q_{total} &= q_{wall} + q_{fluid} \\
 &= \frac{k_{wall} A_{c,wall}}{\Delta x} (T_i + T_{i+1}) + \frac{k A_c}{\Delta x} (T_i + T_{i+1})
 \end{aligned} \tag{3.1}$$

Therefore, the total heat transfer can be written as Eq. (3.2) with a new conductivity equal to the sum of the fluid conductivity and Δk , which is the effect of the tank wall conductivity.

$$q_{total} = \frac{(k + \Delta k) A_c}{\Delta x} (T_i + T_{i+1}) \tag{3.2}$$

$$\Delta k = \frac{k_{wall} A_{c,wall}}{A_c} \quad (3.3)$$

Another method of calculating the additional conductivity created by conduction through the tank walls would be to use the fin concept shown by Lightstone [19], given by Eq. (2.5). Using Eq. (3.2) to calculate the total heat transfer as the sum of the fluid conduction and the tank wall heat conduction, the value of the additional conductivity, Δk , would be:

$$\Delta k = \sqrt{hP k_{wall} A_{c,wall}} \tanh \left(\sqrt{\frac{hP}{k_{wall} A_{c,wall}}} \frac{L}{2} \right) \frac{\Delta x}{A_c} \quad (3.4)$$

Once all of the required inputs for the one-dimensional models are determined, the temperature of node i would be calculated by combining all of the terms into the differential equation shown by Eq. (3.5).

$$\begin{aligned} (M_i C_p) \frac{dT_i}{dt} = & \dot{m}_{in} C_p (T_{in}) - \dot{m}_{out} C_p (T_i) + \dot{m}_{down} C_p (T_{i-1}) \\ & - \dot{m}_{up} C_p (T_i) - \dot{m}_{down} C_p (T_i) \\ & - \dot{m}_{up} C_p (T_{i+1}) + \frac{k + \Delta k}{\Delta x_{i+1 \rightarrow i}} A_{c,i} (T_{i+1} - T_i) \\ & + \frac{(k + \Delta k)}{\Delta x_{i-1 \rightarrow i}} A_{c,i} (T_{i-1} - T_i) \\ & + (U_{tank} + \Delta U_i) A_{s,i} (T_{env} - T_i) \\ & + UA_{hx} (LMTD) + \gamma_{htr} Q_{aux} \end{aligned} \quad (3.5)$$

This can be rewritten by collecting all of the terms with the same node temperatures together and combining the coefficients to get:

$$\frac{dT_i}{dt} = A_i T_{i-1} + B T_i + C_i T_{i+1} + D_i \quad (3.6)$$

The TRNSYS one-dimensional models are all discretized similarly. However, there are differences between them since some include more features and use different solutions schemes to solve the differential equations for each of the tank nodes. The main differences between the models used for this research are shown in Table 3.2, which was adapted from a study performed by Allard et al. [34] that looked at the differences between the results of some of the TRNSYS storage tank models.

Type 534 is able to simulate a tank with the largest number of nodes, which would increase the numerical accuracy of the model. However, the other models allow for unequal sized nodes to be specified, which can be used to obtain a better approximation of the temperature profile in certain tank locations. For example, a large number of nodes could be specified for the thermocline region to observe the changes in the level of stratification with time. However, this region with a large number of nodes could not be moved to follow the location of the thermocline during charging. It should also be mentioned that even though a larger number of nodes could be used for the Type 534 model, the default configuration of TRNSYS limits the number of derivatives for a simulation to 100. Therefore, the maximum number of nodes that could be used for the simulation of a single storage tank model would be 100.

Table 3.2 – Comparison of the TRNSYS Type 4, Type 60, and Type 534 one-dimensional model characteristics [34]. * indicates that the model includes the respective characteristic.

	Type 4	Type 60	Type 534
Nodes			
Maximum Nodes	100	100	500
Unequal Sized Nodes	*	*	
Inlet Modes			
Specified Nodes	*	*	*
Closest Temp. Node	*	*	*
Fractioned Inlet Nodes			*
Energy Balance			
Specified Node Loss Coeff.	*	*	*
Thermal Conductivity		*	*
Fully Mix Temp. Inversions	*	*	*
Temp. Inversion Mixing Flow Rate			*
Numerical Model			
Solution Scheme	DIFFEQ	Crank-Nicolson	Analytical
Internal Time Steps		*	

The models also contain different inlet modes that can be selected by the user. The first mode allows the user to specify any node as the inlet node. This allows for the model to account for different tank designs where the inlet could be located along the side of the tank instead of the top. For the second mode, the node which contains fluid with a temperature closest to the inlet fluid temperature is chosen by the model as the inlet location. This represents an ideal case and would simulate the highest level of stratification that could be obtained for the given inlet conditions. The three models researched here all

consider these two inlet modes. However, the Type 534 model also considers an inlet mode which allows the user to specify different fractions of the inlet flow to be delivered to different nodes. This could be used to account for higher inlet flow rates where the inlet fluid penetrates deeper into the tank than just the inlet node.

For the nodal energy balances, all of the models contain the terms summarized in Table 3.1 except for Type 4 which does not consider the conductivity between the nodes. This means that the third term in Table 3.1 is neglected in the Type 4 model.

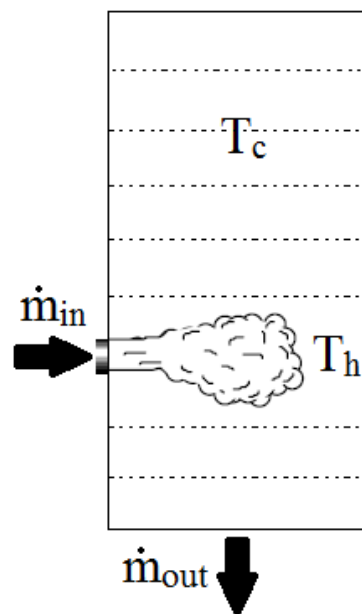


Figure 3.3 – Schematic of a storage tank showing hot fluid entering below cold fluid layers. A mixing algorithm is used to account for the rise of hot fluid due to buoyancy [33]

The models also account for temperature inversions between the nodes. Due to the buoyancy of the tank fluid, a higher temperature fluid should always be above a cooler fluid. However, this would not occur with these one-dimensional models if, for example,

the hot inlet was located somewhere along the side of the tank, as shown in Figure 3.3 [33], because they do not consider buoyancy. A short-circuit would be created where the initial cold tank fluid would always be contained at the top of the tank as the hot inlet fluid would move downwards towards the outlet. Therefore, to account for the buoyancy of the fluid, a mixing algorithm is used. When the temperature of the node above another is lower, the two nodes will be fully mixed to an average temperature between the two. This calculation is repeated for each node until no temperature inversions exist for the current time step. Type 534 also allows the user to specify a mixing flow rate for the temperature inversions [35].

The main difference between the one-dimensional models is the numerical scheme that is used to solve the differential equations for each node. Newton [33] discussed the numerical schemes used by Type 4 and Type 60. The Type 4 and Type 534 models both use a TRNSYS subroutine called DIFFEQ, which returns a solution to the simplified differential equation Eq. (3.7). For the case of a storage tank, coefficient a_i would be the same as B_i in Eq. (3.6) and b_i would be equal to the sum of the rest of the terms. The solution to the differential equation, given by Eq. (3.8), is iterated until the change in T_i is small. Coefficient b_i can vary over a simulation time step since, for example, it is a function of the heat exchanger temperature. Therefore, to solve the differential equation, the average value over the time step, $b_{avg} = b(T_{avg})$, is used [35].

The new node temperature, $T_{new,i}$ is calculated for each time step assuming that the surrounding nodes are at time-averaged temperatures. Time-averaged node temperatures are calculated using Eq. (3.9).

$$\frac{dT_i}{dt} = a_i T_i + b_i \quad (3.7)$$

$$T_{new,i} = \left(T_i(t) + \frac{b_i}{a_i} \right) e^{a_i \Delta t} - \frac{b_i}{a_i} \quad (3.8)$$

$$T_{avg,i} = \frac{T_i(t) + \frac{b_i}{a_i}}{a_i \Delta t} (e^{a_i \Delta t} - 1) - \frac{b_i}{a_i} \quad (3.9)$$

The Type 60 model uses the implicit Crank-Nicolson scheme to solve the original differential equation. The solution for the new node temperature after each iteration is given by Eq. (3.10). The node temperature is found by iterating until the change in $T_{new,i}$ is small [11]. The advantage of the Crank-Nicolson scheme is that much larger time steps can be used. However, the calculation of the average node temperatures in the Type 60 model are not as accurate since they are calculated using only the previous and current time step temperatures, Eq. (3.11).

$$T_{new,i} = \Delta t \left(\frac{A_i}{2} (T_{i-1} + T_{new,i-1}) + \frac{B_i}{2} (T_i + T_{new,i}) + \frac{C_i}{2} (T_{i+1} + T_{new,i+1}) \right) + T_i \quad (3.10)$$

$$T_{avg,i} = \frac{T_{new,i} + T_i}{2} \quad (3.11)$$

Type 60 also uses internal time steps to increase the accuracy of the solution [33]. This means that a time step size is chosen by the model that is smaller than the user defined time step and calculates the node temperatures for each internal time step. Therefore, the time-averaged node temperature would be more accurate since smaller time steps were considered.

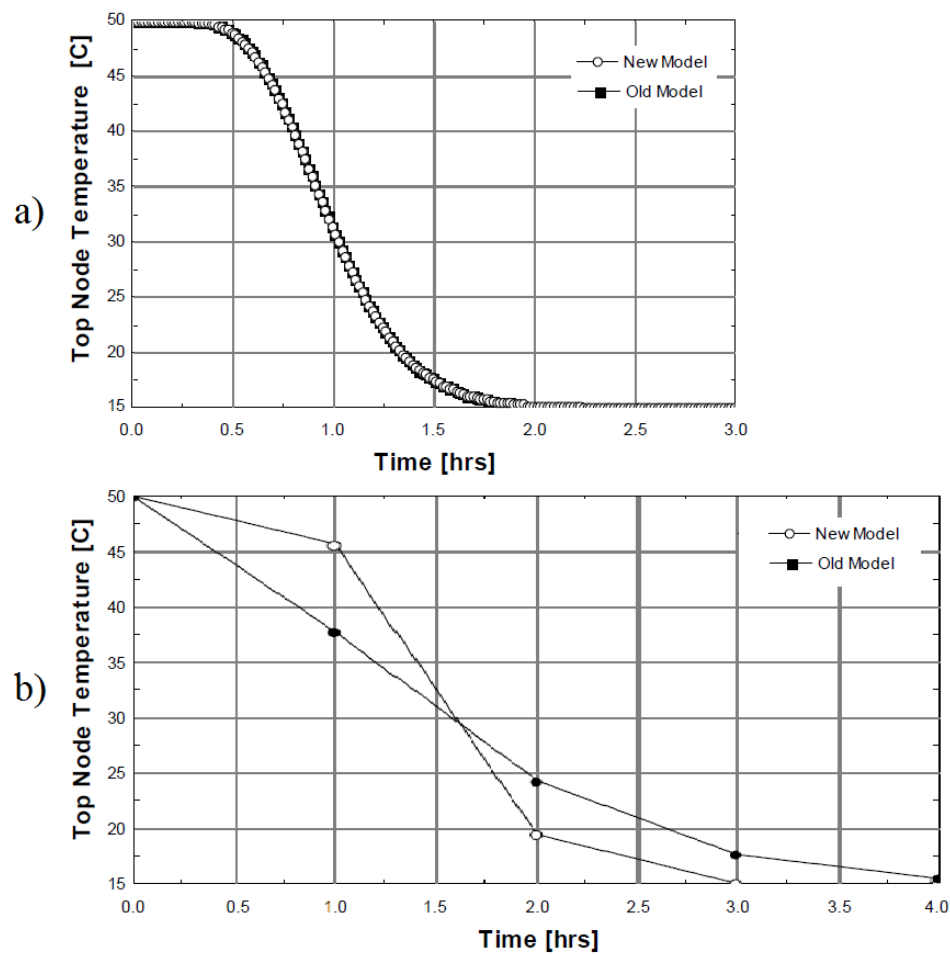


Figure 3.4 – Accuracy of two different TRNSYS one-dimensional models: Old Model (Type 4) and New Model (Type 60) [33]. (a) Temperature profile comparison for a small time step size (1 min), (b) Temperature profiles for a large time step (1 hour).

With the use of this method, the Type 60 model is able to obtain more accurate results when a much larger time step is chosen by the user. This was shown by Newton [33] by comparing the results of the Type 4 (old model) and Type 60 (new model) models with small and large time steps, as shown in Figure 3.4. Figure 3.4a) shows the results with a small time step size of one minute, which gives the actual temperature profile. Both of the models gave similar results for this case since the time step sizes were very small. Figure 3.4b) shows the results with a large time step size of one hour. The Type 4 model shows the incorrect temperature profile due to the increased time step size while the Type 60 model still predicts a similar shape.

It is also important to note that all of the TRNSYS one-dimensional models output the time-averaged nodal temperatures at the end of each time step. This can be observed from the results shown in Figure 3.4. With smaller time steps, the time-averaged temperature would be close to the actual node temperature at the end of the time step since the change in temperature would be smaller [33]. However, with larger time step sizes, the time-averaged temperatures that are determined, calculated with Eq. (3.11), would not be the same. The temperature after one hour shown in Figure 3.4b) is larger than the temperature after one hour in Figure 3.4b) because it would be the average temperature calculated between $t = 0$ and 1 hour.

3.1.2 Quasi One-Dimensional Model

Nizami [17] developed a quasi-one-dimensional model for a thermal storage tank. The model was developed to consider the turbulent mixing effects of a negative buoyant

plume on the temperature profiles within the tank. The inlet jet penetrates to a certain depth, which depends on the temperature difference between the inlet fluid and the fluid adjacent to the jet in the storage tank. A recirculation zone is created as fluid is entrained from the surrounding fluid into the plume, which rises due to buoyancy. As time progresses, the fluid adjacent to the jet will increase in temperature, causing the jet to penetrate deeper as there will be a lower buoyancy force. The inlet Richardson number can be calculated to determine this effect. A larger Ri would indicate a smaller penetration depth since the buoyancy forces are larger than the momentum forces.

Nizami divided the tank into four different regions to account for the different flow patterns experienced within the tank. As shown in Figure 3.5, region δ_1 is the inlet jet region that extends until the axial velocity of the jet reverses direction (when the momentum forces are equal to the buoyancy forces). Region δ_2 is the recirculation zone at the top of the tank that receives fluid from the inlet jet region. Region δ_3 contains the fluid that is entrained into the upward moving plume. Fluid from region δ_3 is also sent into region δ_4 which consists of the remainder of the tank and has an evenly distributed velocity profile over the tank cross-section. The depth of region δ_1 , which is equal to the jet penetration depth, h_j , will also increase with time during charging as the average temperature at the top of the tank increases.

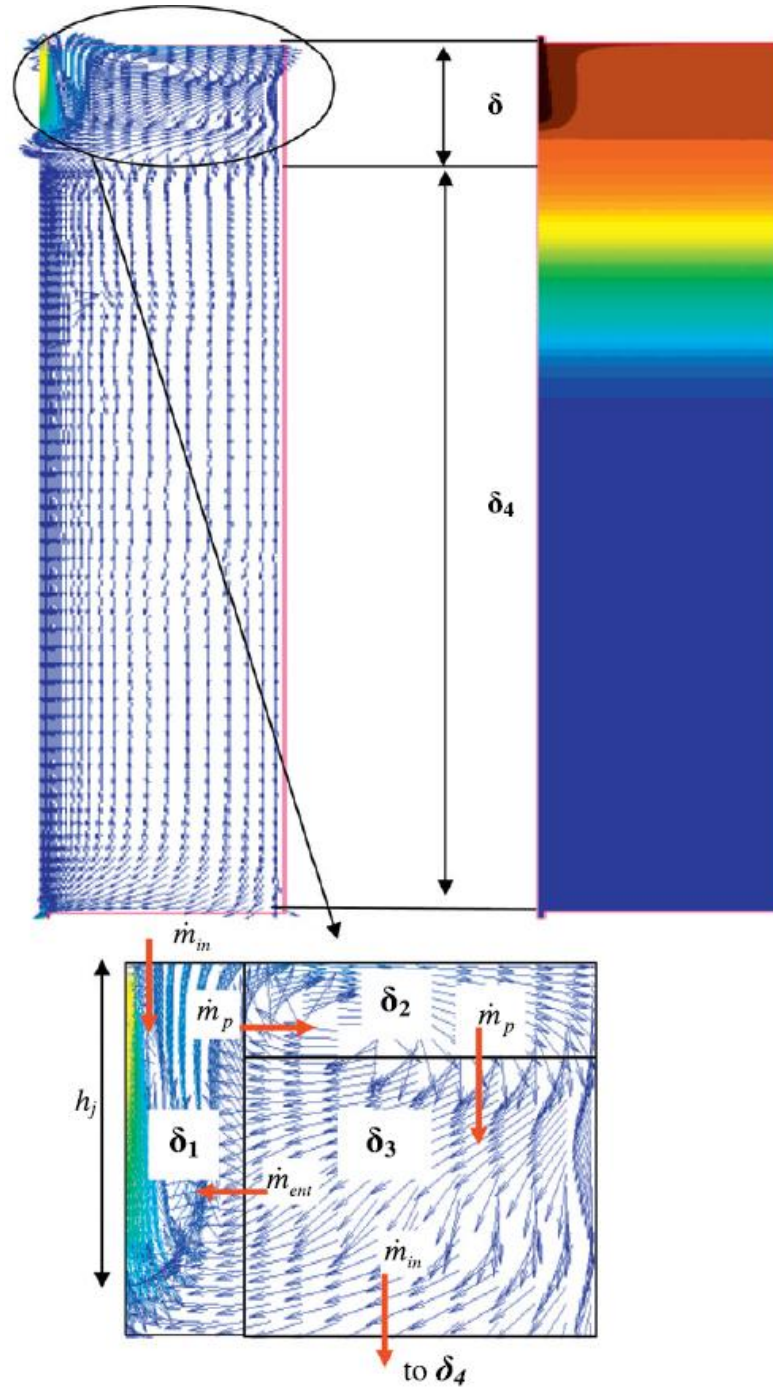


Figure 3.5 – Schematic of the modelling concept used by Nizami [17]. Region δ_1 consists of the inlet jet, region δ_2 involves the recirculation region where fluid enters from the jet region and is redirected downward due to the tank walls, and region δ_3 makes up the rest of the inlet mixing region where fluid enters from region δ_2 at the top and leaves due to the entrainment into the jet and out the bottom to the rest of the tank.

In Figure 3.5, \dot{m}_{in} is the mass flow rate of the hot inlet fluid, \dot{m}_{ent} is the entrainment mass flow rate of the fluid entering region δ_1 from region δ_3 , and \dot{m}_p is the mass flow rate of the plume of fluid entering region δ_2 from region δ_1 , which would be equal to the sum of \dot{m}_{in} and \dot{m}_{ent} .

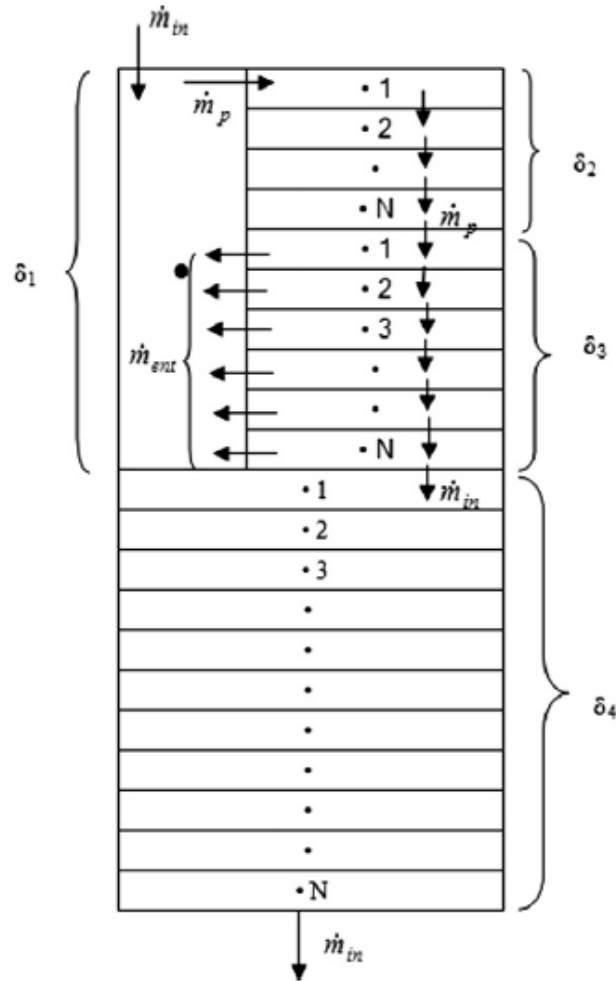


Figure 3.6 – Node discretization used by Nizami to model the inlet mixing effects with a quasi-one-dimensional model [17]. The jet region, δ_1 , is represented as a single node while regions δ_2 and δ_3 are divided into N one-dimensional nodes in the axial direction.

The distribution of the nodes used by this model is shown in Figure 3.6. The inlet jet region, δ_1 , is represented by a single node as the temperature is assumed to be the same

throughout the region. For regions δ_2 , and δ_3 , the flow varies both axially and radially. However, for this model, the flow was assumed to be vertically downwards across a set of one-dimensional nodes. Flow enters the top node of region δ_2 and travels downwards in the tank. Region δ_4 also contains one-dimensional nodes as the flow only occurs axially outside of the inlet mixing region. The extent of each of the regions vary with time as the jet penetration depth changes.

The energy equations for each of the regions are shown in Table 3.3. The quantity α' is the turbulent diffusivity created by the recirculation of the flow and is assumed to be spatially constant in regions δ_2 and δ_3 . The change in the axial mass flow rate in region δ_3 is assumed to be linear with a maximum at the top of the region and a minimum at the bottom, equal to the inlet flow rate. Therefore, the mass flow rate of the fluid leaving the side of each node would be equal to \dot{m}_{ent} .

Table 3.3 – Energy equations used by the model developed by Nizami [17] to calculate the temperatures of the nodes in each of the different tank regions.

Region	Energy Equation
δ_1	$\rho A_{\delta_1} \delta_1 \frac{dT_{\delta_1}}{dt} = \dot{m}_{in} T_{in} - (\dot{m}_{in} + \dot{m}_{ent}) T_{\delta_1} \quad (3.12)$ $+ \dot{m}_{ent} \bar{T}_{\delta_3}$
δ_2	$\rho A_{\delta_2} \frac{\partial T_{\delta_2}}{\partial t} = -\dot{m}_{\delta_2} \frac{\partial T_{\delta_2}}{\partial x} + \rho A_{\delta_2} (\alpha + \alpha') \frac{\partial^2 T_{\delta_2}}{\partial x^2} \quad (3.13)$

δ_3	$\rho A_{\delta_3} \frac{\partial T_{\delta_3}}{\partial t} = -\frac{\partial \dot{m}_{\delta_3} T_{\delta_3}}{\partial x} + T_{\delta_3} \frac{\partial \dot{m}_{\delta_3}}{\partial x} + \rho A_{\delta_3} (\alpha + \alpha') \frac{\partial^2 T_{\delta_3}}{\partial x^2} \quad (3.14)$
δ_4	$\rho A_{\delta_4} \frac{\partial T_{\delta_4}}{\partial t} = -\dot{m}_{\delta_4} \frac{\partial T_{\delta_4}}{\partial x} + \rho A_{\delta_4} (\alpha) \frac{\partial^2 T_{\delta_4}}{\partial x^2} \quad (3.15)$

In order to solve the equations for all of the regions, quantities for the entrainment mass flow rate, region sizes, and the turbulent diffusivity are required. Correlations for these were determined by Nizami by performing a parametric study. The following equations were found that are based on the inlet Richardson and Reynolds numbers where d_{pipe} is the inlet pipe diameter in millimeters, D is the inlet pipe diameter in meters, h_j is the inlet jet penetration depth which determines the extent of region δ_1 , \dot{m} is the non-dimensional entrainment into the plume region (\dot{m}_p/\dot{m}_{in}), and α' is the turbulent eddy diffusivity.

$$h_j = a_{h_j} Ri^{-b_{h_j}} \quad (3.16)$$

$$\dot{m} = a_{\dot{m}} Ri^{-\dot{m}} \quad (3.17)$$

$$\alpha' = a_{\alpha'} Ri^{-b_{\alpha'}} \quad (3.18)$$

$$a_{h_j} = -0.0150 d_{pipe}^2 + 1.40 d_{pipe} + 0.510 \quad (3.19)$$

$$b_{h_j} = 0.00535 d_{pipe} + 0.448 \quad (3.20)$$

$$a_m = 1.062 \quad (3.21)$$

$$b_m = 0.278 \quad (3.22)$$

$$a_{\alpha'} = (1.6 \times 10^{-9})Re - (8.42 \times 10^{-7}) \quad (3.23)$$

$$b_{\alpha'} = 0.2905 \quad (3.24)$$

$$Ri = \frac{\Delta \rho g D}{\rho_r u_{in}^2} \quad (3.25)$$

$$Re = \frac{\rho_{in} u_{in} D}{\mu} \quad (3.26)$$

$$\Delta \rho = \rho_r - \rho_{in} \quad (3.27)$$

Other researchers have found similar relationships for determining these quantities.

Table 3.4 shows the equations determined by different researchers for the jet penetration depth and their descriptions. All of the equations have a Richardson number dependence but were developed for different tank conditions.

Table 3.4 – Comparison of correlations developed by different researchers to determine the jet penetration distance for a fluid entering a medium with a different density.

Paper	Equation	Description
Nizami et al. [17]	$h_j = a_{h_j} Ri^{b_{h_j}}$ $a_{h_j} = -0.015d^2 + 1.4d + 0.51$ $b_{h_j} = 0.00535d + 0.448$	Determined for a negative buoyant plume discharged vertically at the center of the tank.

Pantzlaff and Lueptow [36]	$h = 1.6 M^{\frac{3}{4}} F ^{-\frac{1}{2}}$ $M = \pi r_o^2 U^2$ $F = \pi \left(\frac{g(\rho - \rho_o)}{\rho} \right) r_o^2 U$	$2500 < Re < 21000$ $0.98 < \rho^* < 1.04$ $\rho^* = \frac{\rho_{in}}{\rho_{initial}} = \frac{\rho_o}{\rho}$
Turner [37]	$z_m = 1.85 M^{\frac{3}{4}} F_2^{-\frac{1}{2}}$ $M = \pi r^2 u^2$ $F_2 = \pi g \left(\frac{\rho - \rho_1}{\rho_1} \right) r^2 u$	For $Ri < 1$
Friedman and Katz [38]	$\frac{h}{D_p} = \frac{C_n}{\left(\frac{Ri_p}{F^2} \right)^n}$ $(n, C_n) = \begin{cases} \left(\frac{1}{2}, 2.2 \right) & \text{for } \frac{Ri_p}{F^2} < 0.2 \\ (1, 1) & \text{for } \frac{Ri_p}{F^2} > 0.2 \\ \left(\frac{1}{3}, 0.72 \right) & \text{for } \frac{Ri_p}{F^2} > 2 \end{cases}$	Combined solution using results from different researchers. F is used to account for initial low density region.

A visual comparison of the results for the jet penetration depth at varying Richardson numbers was created by Friedman and Katz [38] and is shown in Figure 3.7. For this research, the correlation developed by Nizami was used since the storage tank conditions that were used to develop the correlation were the same as the cases studied.

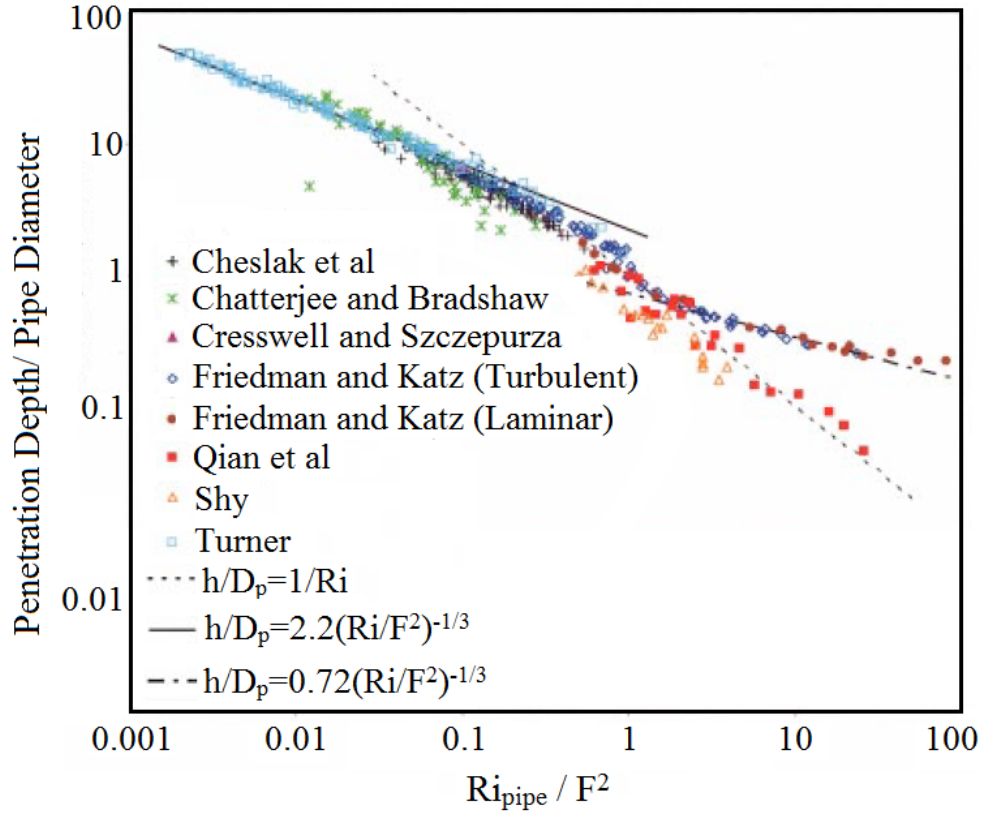


Figure 3.7 – Jet penetration depth calculated by models developed by different researchers for a range of Richardson numbers between 0.001 and 100 [38].

Table 3.5 compares different relationships developed to estimate the effective diffusivity created in the turbulent mixing zone. Zurigat et al. [22] developed a model that assumes the diffusivity varies over the entire tank height from a maximum at the top, where the inlet is located, to a minimum at the bottom. An eddy diffusivity factor was determined that is multiplied by the fluid diffusivity to determine an effective diffusivity value. The eddy diffusivity factor profile along the height of the tank was assumed to be hyperbolic with the maximum value, ϵ_{eff}^{in} , calculated using different correlations depending on the inlet conditions. N_{slt} is the total number of nodes (or “slabs”) that are considered for a one-dimensional representation and N_{sl} is the current node number.

Schlichting [15] also provides an equation to represent the eddy viscosity for a circular jet that is discharged into an infinite volume. Two different correlations were developed for the eddy viscosity in the jet and the eddy viscosity in the jet plume, as shown in Figure 3.8. The eddy viscosity for the jet depends on the jet half width at half depth, $b_{1/2}$, and the maximum jet velocity, v_{max} . The eddy viscosity in the plume changes depending on the depth considered. It is calculated using the jet half width and the maximum velocity at the considered depth.

Table 3.5 – Comparison of correlations developed by different researchers to calculate the turbulent diffusivity of the fluid in the proximity of at jet of fluid.

Paper	Equation	Description
Nizami et al. [12]	$\alpha' = a_{\alpha'} Ri^{-b_{\alpha'}}$ $a_{\alpha'} = (1.6 \times 10^{-9}) Re - (8.42 \times 10^{-7})$ $b_{\alpha'} = 0.2905$	Determined for a negative buoyant plume discharged vertically at the center of the tank.
Zurigat et al. [16]	$\alpha_{eff} = \epsilon_{eff} \alpha$ $\epsilon_{eff} = \frac{A}{N_{sl}} + B$ $A = \frac{\epsilon_{eff}^{in} - 1}{1 - \frac{1}{N_{slt}}}$ $B = \epsilon_{eff}^{in} - A$	Determined for tanks with side inlet. The diffusivity is assumed to vary along the entire tank height.
Schlichting [40]	Eddy Viscosity for Jet:	Determined for a circular jet discharged into an infinite volume.

	$\mu_t = 0.0256 b_1 \frac{1}{2} \rho v_{\max}^2$ <p>Eddy Viscosity in Plume:</p> $\mu_t = 0.068 b_1 \frac{1}{2} \rho v(j)_{\max}$ $b_1 = 0.0848x$	<p>Assuming $Pr_t = 1$:</p> $k = c_p \mu$ $\alpha_t = \frac{\mu_t}{\rho}$
--	---	--

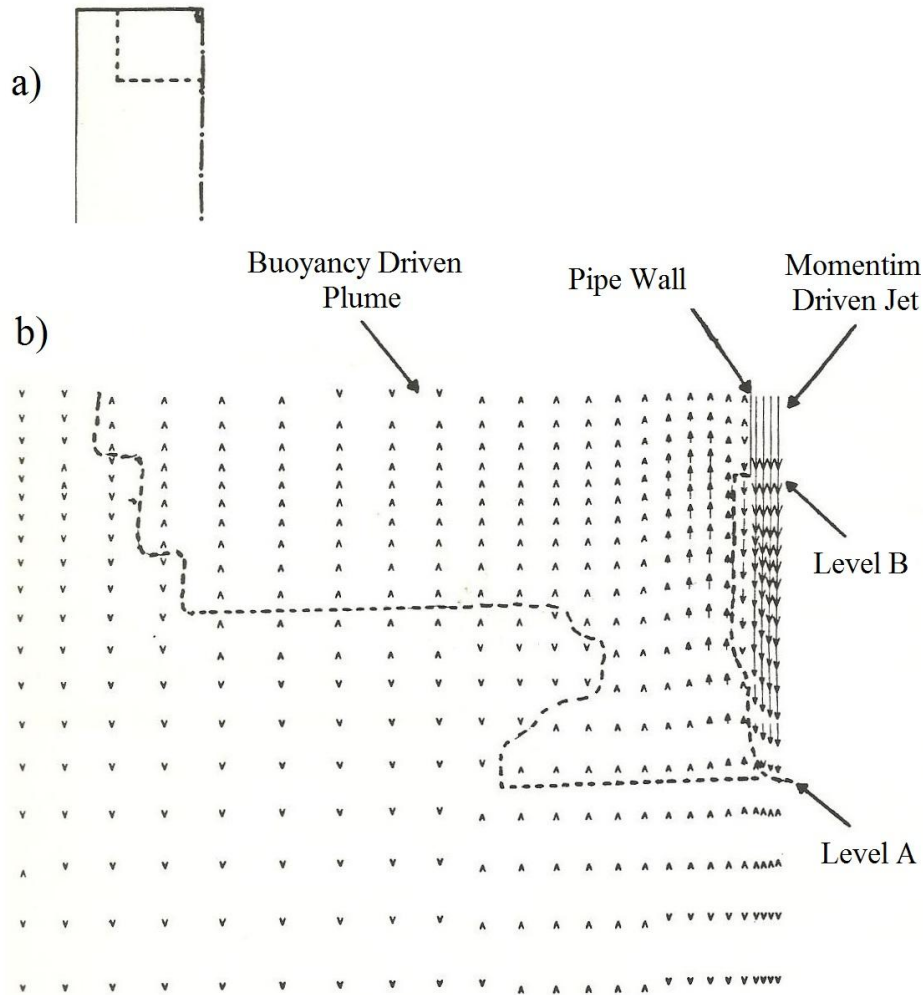


Figure 3.8 – Schematic of the different velocity regions near a circular jet [19]. The momentum driven jet region is indicated separately from the buoyancy drive plume region where there are different diffusion characteristics.

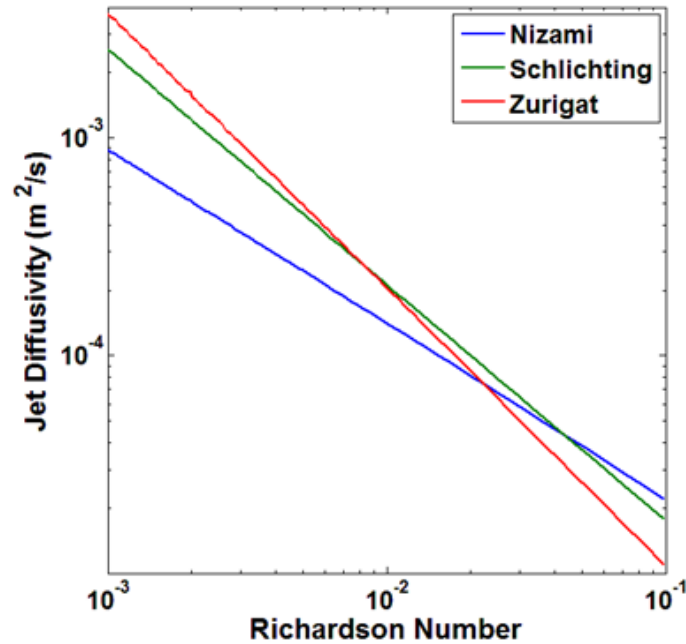


Figure 3.9 – Comparison of the results obtained by the different correlations for the turbulent jet diffusivity for a range of Richardson numbers from 0.001 to 0.1.

A comparison of these eddy diffusivity models is shown in Figure 3.9 for a range of Richardson numbers. All of the equations gave fairly similar results. The main cause for the differences in the profiles would be due to the different conditions they were developed for. The equation developed by Nizami was used for the modelling done for the current research as the conditions match with the cases studied. A storage tank was tested with the inlet at the top of a vertical tank and an outlet at the bottom.

3.2 Numerical Diffusion in One-Dimensional Models

Powell and Edgar [39] discussed a few of the issues with using one-dimensional models for the simulation of thermal storage tanks. Figure 3.10 shows how the solution of a temperature profile is affected by the number of nodes that are used to discretize the domain within a storage tank. As seen in the figure, the temperature profile showed

significant diffusion when a coarse grid was applied. As the number of nodes was increased, the solution began to converge to a profile with a higher level of stratification. However, a fine grid with a large number of nodes (10,000) was required to reproduce the step-function behaviour. This is not desirable for a systems code because of the high computational cost.

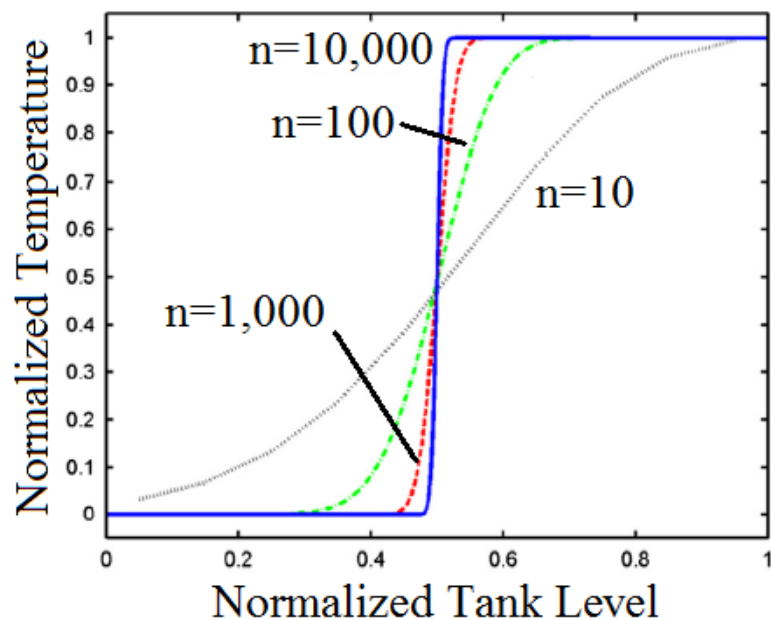


Figure 3.10 – Variation in the amount of diffusion shown by the temperature profiles determined by a one-dimensional model of a storage tank with different amounts of nodes [39].

The numerical diffusion shown by the profiles in Figure 3.10 is a result of the discretization process. This arises from the assumption that each of the nodes is fully mixed, which is used to approximate the temperature of the convected fluid that enters each adjacent node. This phenomenon is shown in Figure 3.11. There is initially a perfectly stratified tank with the top two nodes at a hot temperature and the bottom three nodes at a cold temperature. After a single time step, hot fluid is convected into a portion the middle

node from the node above while the rest of the node still contains cold fluid. The middle image shows what would occur in an actual storage tank, assuming a plug flow with no conduction along the hot and cold region interface. However, the one-dimensional models would output a fully mixed average temperature for the entire node after the time step, as shown by the image on the right. This reduces the expected temperature of the portion of the node that was filled with hot fluid and creates the effect of additional (numerical) diffusion.

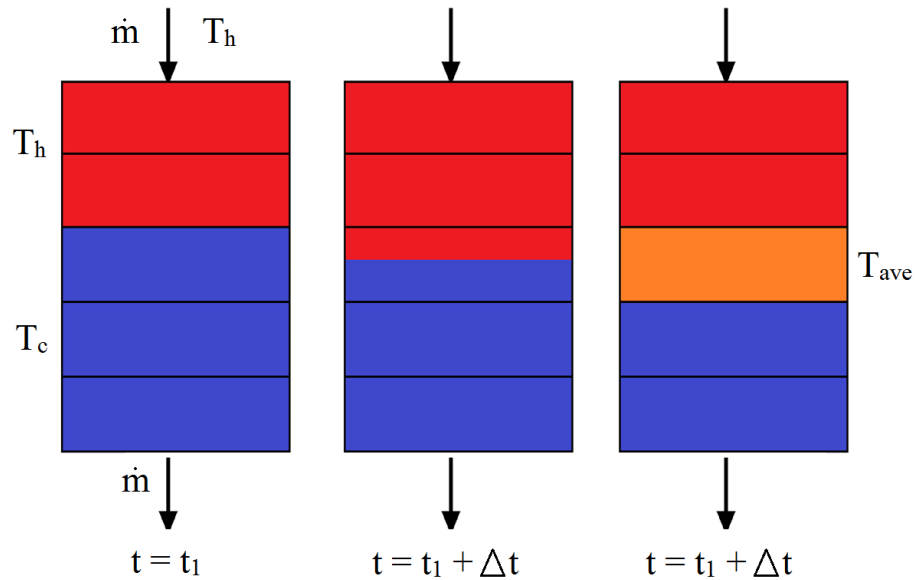


Figure 3.11 – Visualization of numerical diffusion after a single time step. (a) shows the initial temperature profile, (b) shows the actual profile after a single time step where hot fluid has filled a portion of the next node, and (c) shows the profile output by a one-dimensional model with a fully mixed temperature for the middle node.

The definition of the Courant number, Eq. (3.28), gives a method of determining the simulation parameters that lead to a more accurate solution. For explicit solvers, the Courant number should be close to one to reduce the amount of numerical diffusion. This would mean that the volume of fluid that enters a node after a single time step would be

equal to the volume of the node. For the case shown in Figure 3.11, the Courant number would be around 0.5 since about half the node is filled with hot fluid after one time step. As shown by Powell and Edgar [39], the numerical diffusion can be reduced by increasing the number of nodes (ie. decreasing Δx) because the volume of the nodes become smaller. The Courant number definition shows that increasing the time step size would also lead to less numerical diffusion. Implicit solvers, such as the ones used by the TRNSYS models are typically less sensitive to numerical instability and a larger Courant number could be used.

$$\text{Courant Number} = \frac{u\Delta t}{\Delta x} \approx 1 \quad (3.28)$$

Kleinbach et al. [40] developed correlations from experimental data to determine the number of nodes that should be used for these one-dimensional models to obtain results that agree with experimental results. To determine these correlations, solar thermal system experiments were performed with varying heat source flow rates, load draw profiles, collector areas, and collector flow rates. Results from one-dimensional simulations using the same conditions and varying numbers of nodes were compared with the experimental data. It was found that the collector area and collector flow rate did not have much effect on the results of the one-dimensional models. Therefore, the correlations were developed to relate the number of nodes required with the mean number of tank turnovers, T , for fixed and variable inlet conditions, Eq. (3.29) and Eq. (3.30) respectively.

$$N_{fixed} = 45.8T^{-1.218} \quad (3.29)$$

$$N_{variable} = 23.1T^{-0.966} \quad (3.30)$$

The recommended number of nodes was determined to be the smallest amount of nodes that produced relative errors in the energy quantities QI and QD below 5%. QI and QD represent the ability of the model to output the correct temperature of the fluid that is returned to the heat source, Eq. (3.31), and the fluid that is delivered to the load, Eq. (3.32).

$$QI = \frac{Q_{in,sim} - Q_{in,exp}}{Q_{in,exp}} \quad (3.31)$$

$$QD = \frac{Q_{del,sim} - Q_{del,exp}}{Q_{del,exp}} \quad (3.32)$$

Where:

$$Q_{in} = \int_{day} \dot{m}_{heat} C_f (T_{heat} - T_{ret}) dt \quad (3.33)$$

$$Q_{del} = \int_{day} \dot{m}_{load} C_f (T_{del} - T_{mains}) dt \quad (3.34)$$

While these correlations may give a good approximation of the recommended number of nodes to represent a realistic thermal storage tank for some cases, they do not provide the number of nodes required to eliminate numerical error. The simulations would still contain a significant amount of numerical diffusion, but at a level that would produce results similar to actual experimental cases. Therefore, the numerical diffusion created due to the use of the suggested number of nodes is used to account for the loss of stratification due to additional mixing mechanisms within a storage tank. However, adding additional diffusion will not solve some of the problems when trying to replicate some mixing

mechanisms, such as inlet jet mixing. As discussed in section 2.1.1. Experimental results obtained by Oliveski et al. [18] and Leohrke and Holzer [20] show that certain conditions will lead to very different temperature profiles than expected due to inlet jet mixing.

3.3 Alternative Modelling Techniques

To address some of the issues that are experienced with one-dimensional, multi-node models, alternative strategies have been developed to model the temperature profile within a storage tank. TRNSYS includes a plug flow storage tank model which allows the node volumes to increase/decrease, depending on the amount of fluid being added to the tank. An adaptive-grid plug flow model was also developed to allow for a larger number of nodes to be considered for the thermocline region as it moves throughout the tank.

3.3.1 TRNSYS Plug Flow Model

An alternative strategy used to model the temperature profiles in thermal storage tanks is to assume that the inlet fluid fills the tank in a plug flow motion. The TRNSYS Type 38 model predicts the temperature profiles in a thermal storage tank by using variable sized segments of fluid [11]. The size of each of the segments depends on the velocity of the fluid within the tank and the temperature of the fluid entering. Since the sizes of the segments can vary with time, the Type 38 model has the ability to represent the temperature in the thermocline with a higher accuracy than the one-dimensional models.

The process that is used to simulate the plug flow within a tank is shown in Figure 3.12. This example shows a tank that initially contains four temperature regions. Hot water

is entering the tank at the top (collector flow) and cold water is entering the bottom (load flow) as it is simultaneously charged and discharged.

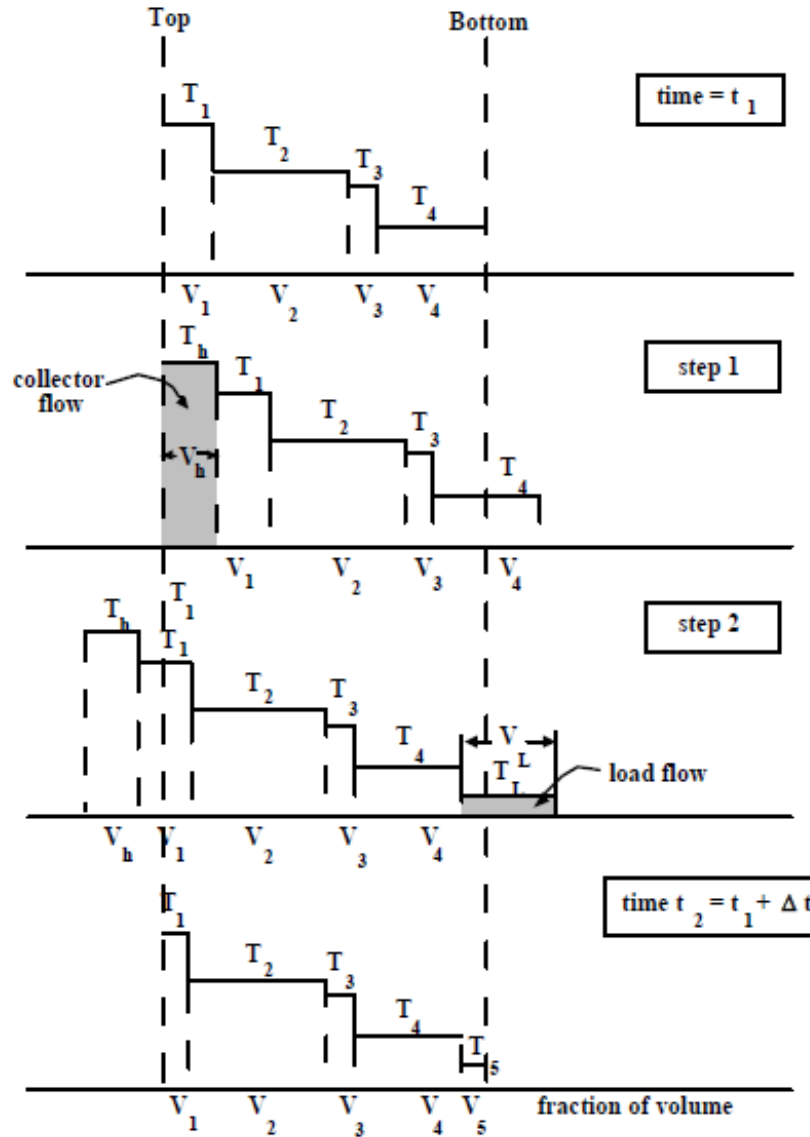


Figure 3.12 – Description of the process used to calculate the temperature profile in a storage tank using the TRNSYS plug flow model (Type 38) [11].

The first step shows the amount of hot water that enters the tank after one time step.

The volume that enters is V_h , which is equal to $\dot{m}_h \Delta t / \rho$. If T_h is greater than T_1 , a new

segment is created at the top. During the same time step, a volume of cold water, V_L , enters the bottom of the tank, equal to $\dot{m}_L \Delta t / \rho$. If T_L is less than T_4 , a new segment is created at the bottom. The overall shift in the segment locations are determined from the difference between the inlet and outlet flow volumes $(\dot{m}_h - \dot{m}_L) \Delta t / \rho$. The partial volumes that are outside of the tank regions at the end of the time step are returned to the heat source and load.

The concept of the TRNSYS plug flow model was to allow for a variable number of nodes to be created to obtain a better representation of the temperature profile within the tank compared to the one-dimensional multi-node models which contained a static amount of nodes. However, as found by Allard et al. [34], the number of nodes generated by the model for the tested conditions was never large enough to give results that matched with the level of stratification obtained in the experiments.

3.3.2 One-Dimensional Adaptive-Grid Model

Powell and Edgar [39] presented a one-dimensional, adaptive-grid model that reduced the number of nodes in the regions of the tank with a more uniform temperature and used a larger number of nodes in the thermocline region. Therefore, the hot and cold regions above and below the thermocline are modelled as single nodes while the thermocline region contains enough nodes to accurately predict thermocline temperature profile. These nodes move with the thermocline location, similar to the movement of the nodes in the plug flow model.

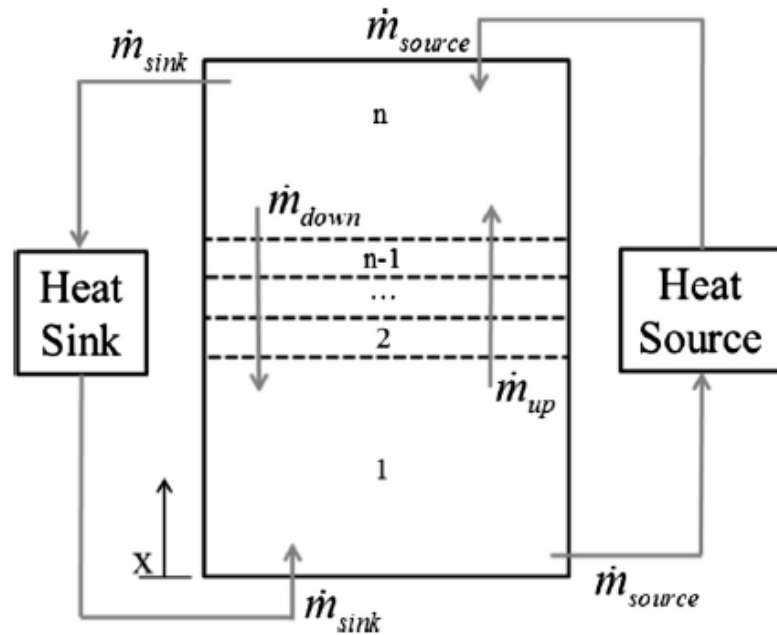


Figure 3.13 – Schematic of the node distribution used for the adaptive-grid plug flow model developed by Powell and Edgar [39].

The distribution and movement of the nodes within the tank over time is described in Figure 3.13. At the beginning of a charging cycle, there is a large number of nodes at the top of the tank. These nodes do not move until the center of the thermocline reaches the middle node (mid). Once this occurs, the volume of node n will increase and the volume of node 1 will decrease as the thermocline nodes move downwards in the tank, keeping the thermocline centered within the middle nodes. When the nodes reach the bottom of the tank, node movement stops as the thermocline continues to move to the bottom of the tank as charging progresses.

Visualizations of the different events are shown in Figure 3.14. The initial charging phase, where the nodes do not move, occurs while the average thermocline temperature, T_{avg} , is above the middle node temperature, T_{mid} . The temperatures of the nodes during

this phase are calculated similarly to the one-dimensional, multi-node models. The second phase occurs when the average thermocline temperature equals the middle node temperature, indicating that the center of the thermocline has reached the middle node location. The nodes would then move with the thermocline until the volume of the node at the bottom of the tank, V_1 , equals the minimum node volume, V_{min} . Once this occurs, the nodes will remain stationary for the rest of the simulation as the thermocline progresses downwards in the tank.

The model developed by Powell combines the advantages of the one-dimensional models and the plug flow models while eliminating some of the challenges. One-dimensional models become computationally expensive with a large number of nodes. However, the model developed by Powell only allocates a larger number of nodes in the region of the tank that requires a higher accuracy, which in this case is the thermocline. The regions where the thermocline does not exist only contain a single node as the rest of the nodes move with the thermocline through the tank.

This helps to eliminate some of the computational complexity and a higher accuracy can be obtained. However, the model cannot account for mixing effects caused by the inlet jet since the top of the tank is represented by a single node. The user of the model must also predict the number of nodes that would be required to represent the thermocline throughout the simulation. Therefore, the growth of the thermocline must be considered to ensure that enough nodes are used.

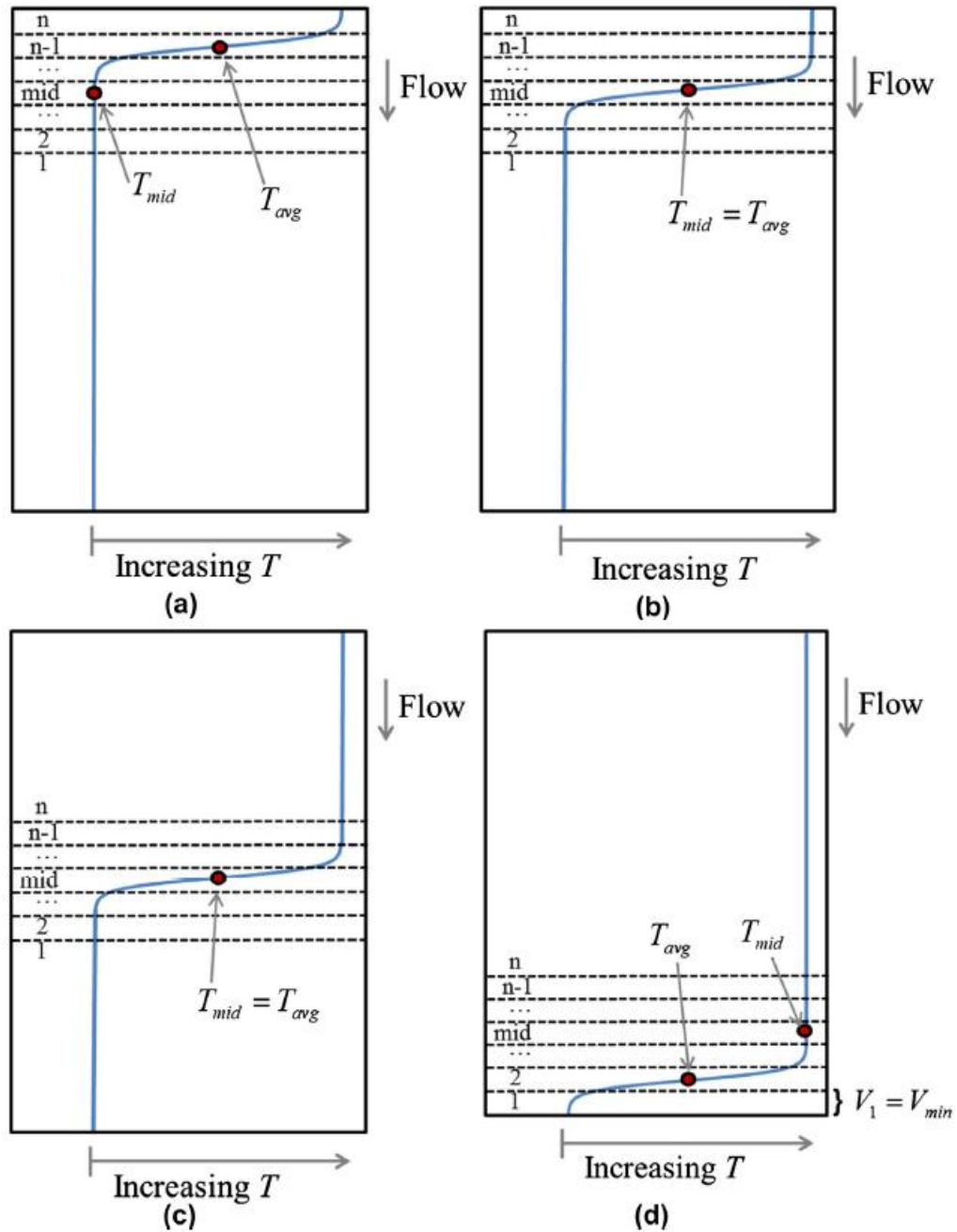


Figure 3.14 – Visualization of the different events determined by the adaptive-grid plug flow model. (a) Initial charging phase with stationary nodes as the thermocline moves downwards, (b) tank nodes move downwards with the thermocline when the center reaches the middle node, (c) the thermocline center is kept at the middle node as the volumes of node n and node 1 change, (d) when the nodes reach the bottom of the tank, they become stationary as the thermocline continues downwards [39].

3.4 Summary

An overview of some of the simple storage tank modelling strategies was included in this chapter. While these models provide a quick estimation of the temperature profiles within the storage tank during a simulation, significant errors have been previously observed by multiple researchers. With the one-dimensional assumption used by these models, the results should show a higher level of stratification than experimental data since they do not account for additional mixing mechanisms such as inlet jet mixing. However, they have been shown to give lower levels of stratification, indicating more mixing than the experimental cases.

This error can be reduced by increasing the number of nodes, but this would lead to increasing computational times, which is not desired. Therefore, this led to the research proposed in this thesis. The TRNSYS one-dimensional models are analyzed to discover the deficiencies of the numerical schemes and new analytical models were developed that give simplified models which can be used for long term solar thermal system simulations while giving a higher accuracy prediction than the one-dimensional models.

Chapter 4

Analysis of TRNSYS One-Dimensional Storage Tank

Models

The TRNSYS system simulation tool is frequently used to simulate solar thermal systems, which typically contain one or more thermal storage tanks. Therefore, to obtain meaningful results, the TRNSYS storage tank models must be able to accurately predict the temperature profiles within a tank for a variety of operating conditions. However, previous experimental tests have shown that these models do not always provide a sufficient level of accuracy since the predictions did not agree with the experimental temperature profiles.

The most commonly used storage tank models are the TRNSYS Type 4, Type 60, and Type 534 one-dimensional models. Therefore, this chapter includes the analysis of these three models to determine how the results compare with an idealized analytical solution developed from the semi-finite wall solution. Two different cases were developed to determine the ability of the models to predict typical scenarios that can occur in an actual thermal storage tank. This helped reveal the conditions that lead to significant numerical error within the simulations. A Taylor series expansion was also implemented to develop a correlation for the numerical error that depends on the important simulation parameters, such as the time step size and the node size.

4.1 Simple Case Analysis

In this work, two cases were used to assess the accuracy of the TRNSYS one-dimensional models. The characteristics of these cases are shown in Table 4.1. Case 1 was used to evaluate how accurately the one-dimensional models could simulate simple conduction between the hot and cold regions within the tank when no fluid motion was considered. The simulated tank was initially set to a perfectly stratified state with the water in the top half of the tank at a uniform hot temperature and the bottom half at a uniform cold temperature. As time progressed, conduction between the layers occurred which created a thermocline that increased in size until the tank reached a fully mixed, uniform temperature.

Table 4.1 – Description of the cases used to study the TRNSYS one-dimensional models.

Case 1 – Stagnant Fluid Conduction	
Initial Conditions	Initially perfectly stratified tank with the top at a hot temperature and the bottom at a cold temperature
Mass Flow Rate (\dot{m})	0 kg/s
Initial Hot Region Temperature (T_h)	50°C
Initial Cold Region Temperature (T_c)	20°C
Case 2 – Plug Flow with Diffusion	
Initial Conditions	Initially cold storage tank
Mass Flow Rate (\dot{m})	0.01 kg/s

Inlet Fluid Temperature (T_{inlet})	$50^{\circ}C$
Initial Tank Fluid Temperature ($T_{initial}$)	$20^{\circ}C$

The effects of fluid motion were included in Case 2. A typical charging cycle was simulated that consisted of an initially discharged tank at a uniform cold temperature. Hot water was introduced at the top of the tank as the charging commenced. Therefore, a thermocline formed along the hot and cold region interface and was advected downwards at the mean fluid flow rate within the tank. Numerical error was expected to occur in this case due to the fluid motion within the tank and the numerical diffusion that would be created.

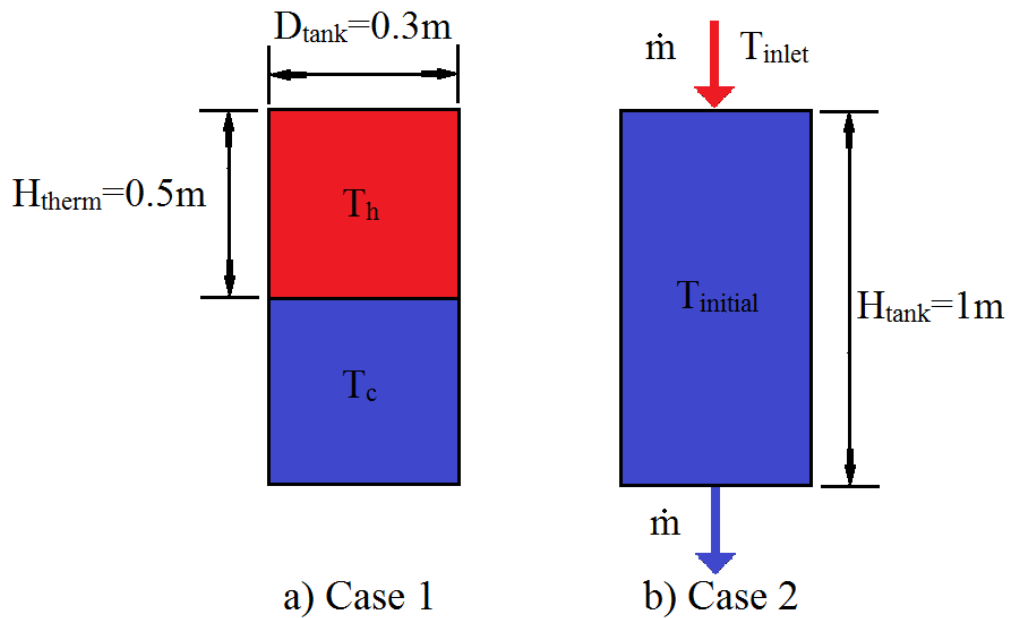


Figure 4.1 – Tank dimensions and initial conditions used for (a) Case 1 and (b) Case 2 to study the TRNSYS one-dimensional models.

The storage tank dimensions and initial conditions used for these two cases are shown in Figure 4.1. The tank had a diameter of $0.3m$ and a height of $1m$ and was

discretized axially into N equally sized nodes. The hot and cold temperatures that were considered in both cases were 50°C and 20°C . For these simple cases, heat losses to the surroundings were neglected. Therefore, the heat transfer coefficient was set to $0\text{ W/m}^2\text{K}$ for each node. The fluid properties for the simulations were determined at the average water temperature, 35°C , as given in Table 4.2

Table 4.2 – Water properties used for one-dimensional simulations of Case 1 and Case 2.

Density, ρ (kg/m^3)	992.73
Thermal Conductivity, k (W/mK)	0.62614
Specific Heat Capacity, C_p (J/kgK)	4068.5
Dynamic Viscosity, μ (m^2/s)	7.0057×10^{-4}
Thermal Expansion Coefficient, β ($1/\text{K}$)	3.245×10^{-4}

To test the performance of the models for these cases, simulations were done with varying numbers of nodes (varying grid spacing) and time step sizes. This helped show how the numerical errors were affected by the simulation parameters and how much refinement was required to reduce this error. The number of nodes was first varied between 10 and 100 (where 100 nodes was the maximum amount allowed by the default configuration of TRNSYS) while keeping the time step size constant at 1 second. Simulations were then run for time step sizes of 1 second, 1 minute, 5 minutes, 10 minutes, and 20 minutes with the use of 50 tank nodes. RMS errors for each case were plotted and are shown in Appendix B.

4.2 Analytical Solution

To evaluate the accuracy of the models, the analytical solution for a semi-infinite wall, heat conduction problem, as shown previously in Figure 2.10, was implemented to determine the temperature profiles that the one-dimensional models should output if no numerical error was involved. The solution to the diffusion equation, Eq. (4.1), for a semi-infinite wall with a constant temperature boundary is given by Eq. (4.2), where T_o is the hot boundary temperature, $T_{initial}$ is the initial wall temperature, α is the thermal diffusivity of the wall, x is the wall depth, and t is the simulation time.

$$\frac{\partial^2 T}{\partial x^2} = \frac{1}{\alpha} \frac{\partial T}{\partial t} \quad (4.1)$$

$$\frac{T - T_o}{T_{initial} - T_o} = \text{erf}\left(\frac{x}{\sqrt{4\alpha t}}\right) \quad (4.2)$$

Additional details of the semi-infinite wall solution and its analogy with the heat conduction through a thermocline is presented in Appendix A. Thus, this solution can be used to model the diffusion between the hot and cold regions within a thermal storage tank and calculate the temperature profiles of the thermocline over time for a simple conduction case with no flow. This was done by splitting the solution into two separate equations: one for the bottom half of the thermocline, Eq. (4.3), and one for the top half, Eq. (4.4). For these equations, the hot boundary temperature in the semi-infinite wall solution, T_o , was set to the average thermocline temperature ($T_{ave} = 0.5(T_c + T_h)$) and $T_{initial}$ was the cold region temperature (T_c). The quantity C represents the location of the thermocline center with time as the diffusion occurs. For Case, 1 with stagnant fluid conduction, the hot and

cold regions meet at the center of the tank. Therefore the thermocline location, C , would be equal to $H/2$.

$$T_{bottom}(x, t) = T_{ave} + (T_c - T_{ave}) \operatorname{erf}\left(\frac{x - C}{\sqrt{4\alpha t}}\right) \quad (4.3)$$

$$T_{top}(x, t) = (T_c + T_h) - \left(T_{ave} + (T_c - T_{ave}) \operatorname{erf}\left(\frac{C - x}{\sqrt{4\alpha t}}\right)\right) \quad (4.4)$$

This solution method can also be applied to model the temperature profiles for a case with fluid flow, such as for Case 2. This was done by assuming that the water in the tank moves one-dimensionally as a plug flow. Therefore, the center of the thermocline would also move at a plug flow velocity and the location of the center of the thermocline can be determined from integration of that velocity with time, Eq. (4.5). Therefore, the value of C in Eq. (4.3) and Eq. (4.4) can be increased for each time step of the simulation.

$$C(t) = \int_0^t \frac{\dot{m}_{in}(t^*)}{\rho A_C} dt^* \quad (4.5)$$

This analytical solution provides the theoretical maximum level of stratification within the tank since the only mechanism considered that would lead to mixing between the hot and cold regions was diffusion. There was no inlet mixing or heat losses considered in the calculation. Therefore, this should be the result of the one-dimensional models, for the simple cases tested in this research, if there was no numerical error. The MATLAB code used to calculate the analytical solutions for these two test cases is provided in Appendix D.1.

In addition to calculating the temperature profiles, this analytical model can also be used to calculate the thickness of the thermocline with time. Eq. (4.3) was rearranged to obtain an equation for the x -location as a function of temperature and time. Therefore, the location within the tank that experiences a particular temperature at a certain point in time can be determined, using Eq. (4.6). The location of the edge of the thermocline would occur where the temperature was equal to the cold region temperature. However, the cold temperature, T_c , cannot be used to calculate the edge of the thermocline using this equation because the temperature profile is asymptotic and a very large value of x would be required before the exact value of T_c was found. This was due to the use of the error function derived from the semi-infinite wall solution. Therefore, a cut-off value, X , was required to define a temperature close to the cold region temperature for the edge of the thermocline. Eq. (4.7) gives the solution for half of the thermocline thickness since the semi-infinite wall solution only models half of the thermocline.

$$x - C = \sqrt{4\alpha t} \operatorname{erfinv} \left(\frac{T - T_{ave}}{T_c - T_{ave}} \right) \quad (4.6)$$

$$\frac{W_{therm}}{2} = x_{therm} - C = \sqrt{4\alpha t} \operatorname{erfinv} \left(\frac{XT_c - T_{ave}}{T_c - T_{ave}} \right) \quad (4.7)$$

Previous researchers have used a non-dimensional temperature cut-off value, $\theta = \frac{T - T_c}{T_h - T_c}$, to define the edge of a thermocline for experimental data ([41], [42]). A θ value of 0.1 has been suggested, which means 90% of the thermocline profile is considered when determining the thermocline thickness and 10% is discarded. This worked well for temperature profiles obtained experimentally because the “tails” of the profile will

experience small changes in temperature as the distance from the center of the thermocline increases, as shown in Figure 4.2.

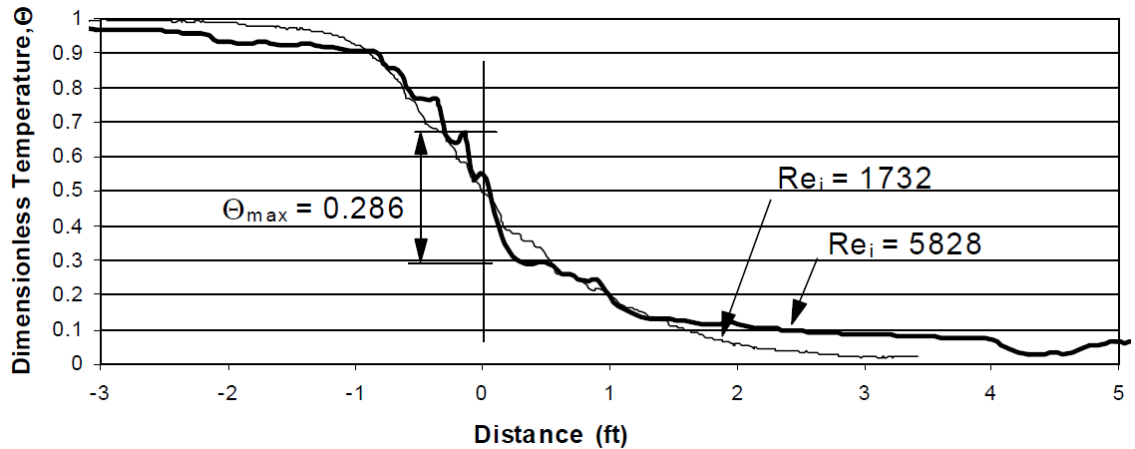


Figure 4.2 – Experimental temperature profile showing a large variation in the temperature of the hot and cold regions above and below the thermocline [41].

However, considering only 90% does not provide an accurate representation of the thermocline thickness for an analytical temperature profile since there is less variation in the hot and cold regions above and below the thermocline. Figure 4.3 shows a comparison of the thermocline thicknesses calculated using Eq. (4.7) for different cut-off values. The thermocline thickness found using a X value of 1.1, which considers 90% of the thermocline as suggested, ignores a large region where the temperature varies and the thermocline thickness is not represented accurately. Therefore, a cut-off value of 1.01 was used to determine the thermocline thickness of an analytical temperature profile. This was similar to the method used to calculate boundary layer disturbance thickness [43] since 99% of the thermocline profile is considered.

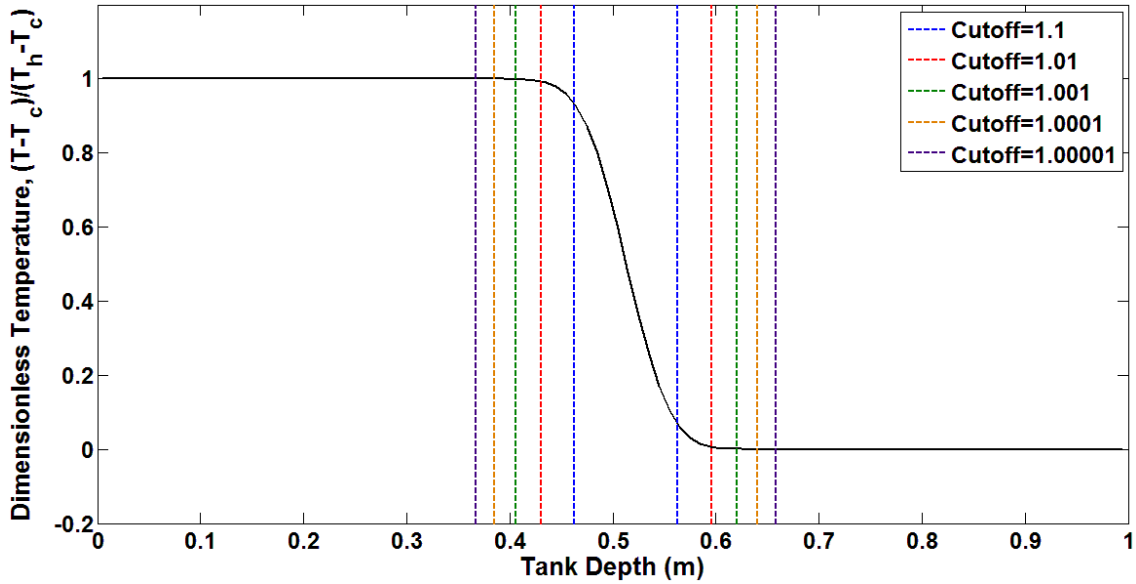


Figure 4.3 – Limits of the thermocline thicknesses determined using Eq. (4.7) for different cut-off values, X .

It is useful to be able to determine the theoretical thermocline thickness using this analytical solution because the calculated value could be compared to the thermocline thickness determined from simulation results. This is a good way of determining if there is error in the simulations because numerical error would lead to more diffusion and a larger thermocline thickness. Knowing the thermocline thickness at the end of the time step can also help when modelling different mixing behaviours, which will be explored later in Chapter 5.

4.3 Simulation Results and Discussion

This section summarizes the results of the case analysis described in Section 4.1. Temperature profiles were plotted for a varying numbers of nodes and time step sizes. Predictions are compared to the analytical solution described above. These comparisons

showed which simulation parameter had the largest effect on the error and how much refinement was required to obtain a more accurate solution.

4.3.1 Case 1 Results

1) Sensitivity to Grid Spacing

The results obtained from the TRNSYS models (Type 4, Type 60, and Type 534) for Case 1 with a varying number of nodes are shown in Figure 4.4. The axial temperature profiles were plotted after 4 hours into the simulation, which provided enough time for a significant amount of diffusion to occur. The comparisons show that with a large number of nodes, excellent agreement between the analytical solution and numerical solution using Types 534 and 60 was obtained.

However, as the number of nodes was decreased, there were some differences between the models and the analytical solution. The one-dimensional models estimate the heat flux between the nodes by assuming a linear temperature profile between the node centers. Therefore, when a coarser grid was used, the linear temperature profile was determined over a larger distance, which resulted in a poor estimation of the heat flux. Therefore, the change in the node temperatures with time were not represented accurately by the models. A maximum RMS error of about 0.97°C was obtained with the coarsest grid.

Very different results were given by the Type 4 model for Case 1. Figure 4.4c shows that the same profile was obtained for the temperature within the tank for all of the simulations. This step-function profile given by each simulation shows the same initial

temperature distribution used for the simulations with the hot water in the top half of the tank and the cold water in the bottom. These results occurred because the Type 4 model does not consider conduction between the nodes. Therefore, for this case involving only diffusion between the hot and cold regions, the model was not able to calculate the growth of the thermocline with time. Simulations using this model for a stagnant flow would therefore predict an idealized, perfectly stratified tank with no diffusion or mixing mechanisms. This model is therefore not capable of predicting the diffusion-based test case.

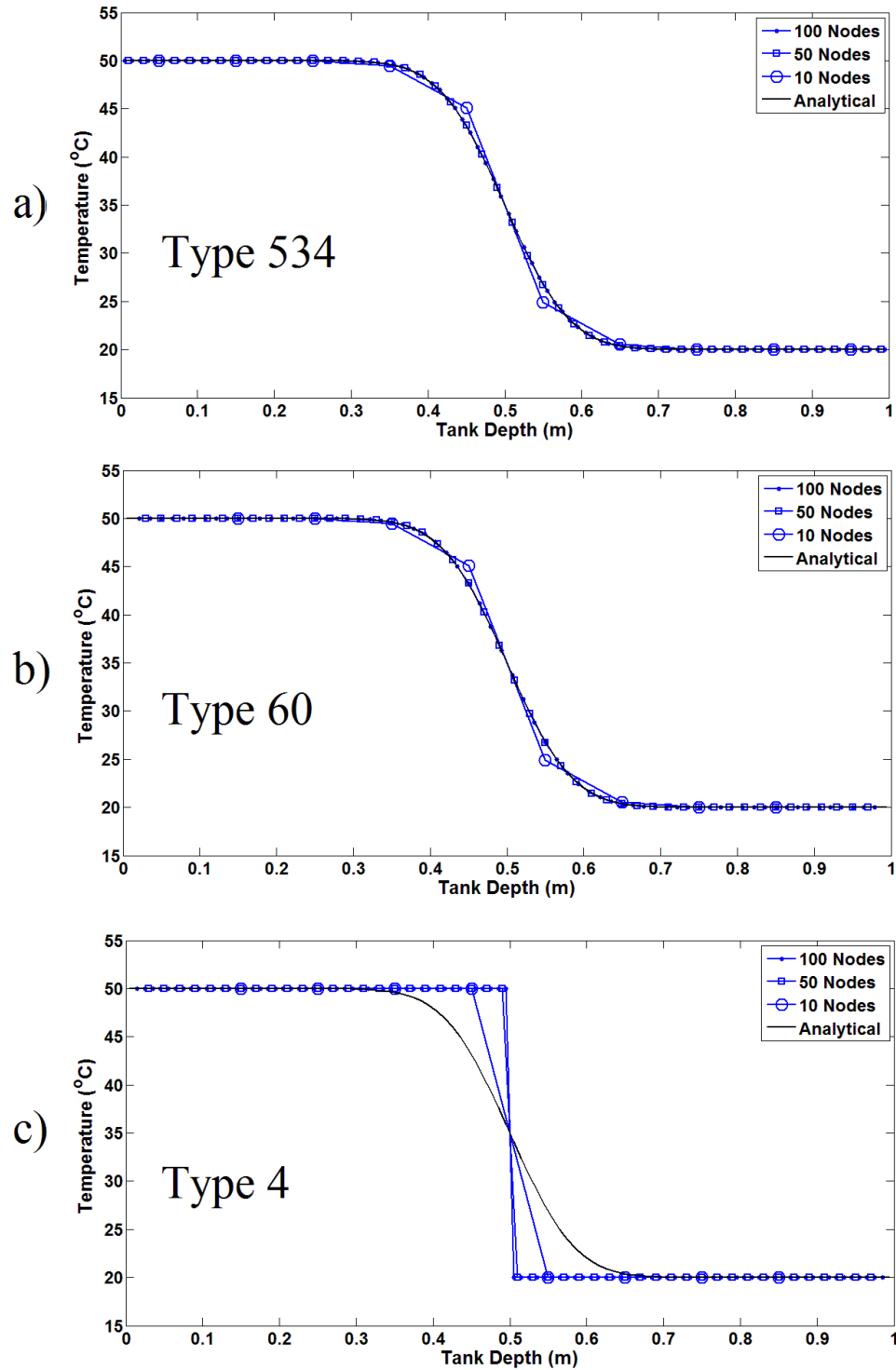


Figure 4.4 – Temperature vs tank depth results for Case 1 after 4 hours into the simulation with varying numbers of nodes and 1 second time steps. (a) Type 534 model, (b) Type 60 model, (c) Type 4 model.

2) Sensitivity to Time Step Size

Figure 4.5 shows the simulation results for Case 1 after 4 hours with varying time step sizes. Again, the Type 534 and Type 60 models gave similar results that agreed with the analytical solution. The temperature profiles did not change significantly with an increasing time step size for all of the tested models. Since 50 nodes were used for all of the simulations, the grid spacing used was constant and the results all showed the correct temperature profiles.

This revealed that the time step size had a very small effect on the results when no flow was considered. The RMS errors for all of the tested time step sizes were very small and only varied by about $0.06^{\circ}C$ with a maximum of $0.1^{\circ}C$. The conduction between the hot and cold regions occurred over a larger time scale than the time step sizes that were tested for this case. The RMS error plots in Appendix B show that the Type 60 model produced less error than the Type 534 model for the time step sizes tested because it used internal time steps to calculate the node temperatures. However, the difference between the two models was very small and both models showed good agreement with the analytical profiles. Therefore, larger time step sizes could be implemented for a simple conduction case while keeping a good level of accuracy.

As expected, the Type 4 model predictions were insensitive to the time step. The initial profile was again maintained for all of the simulations since no conduction was calculated between the hot and cold fluid regions.

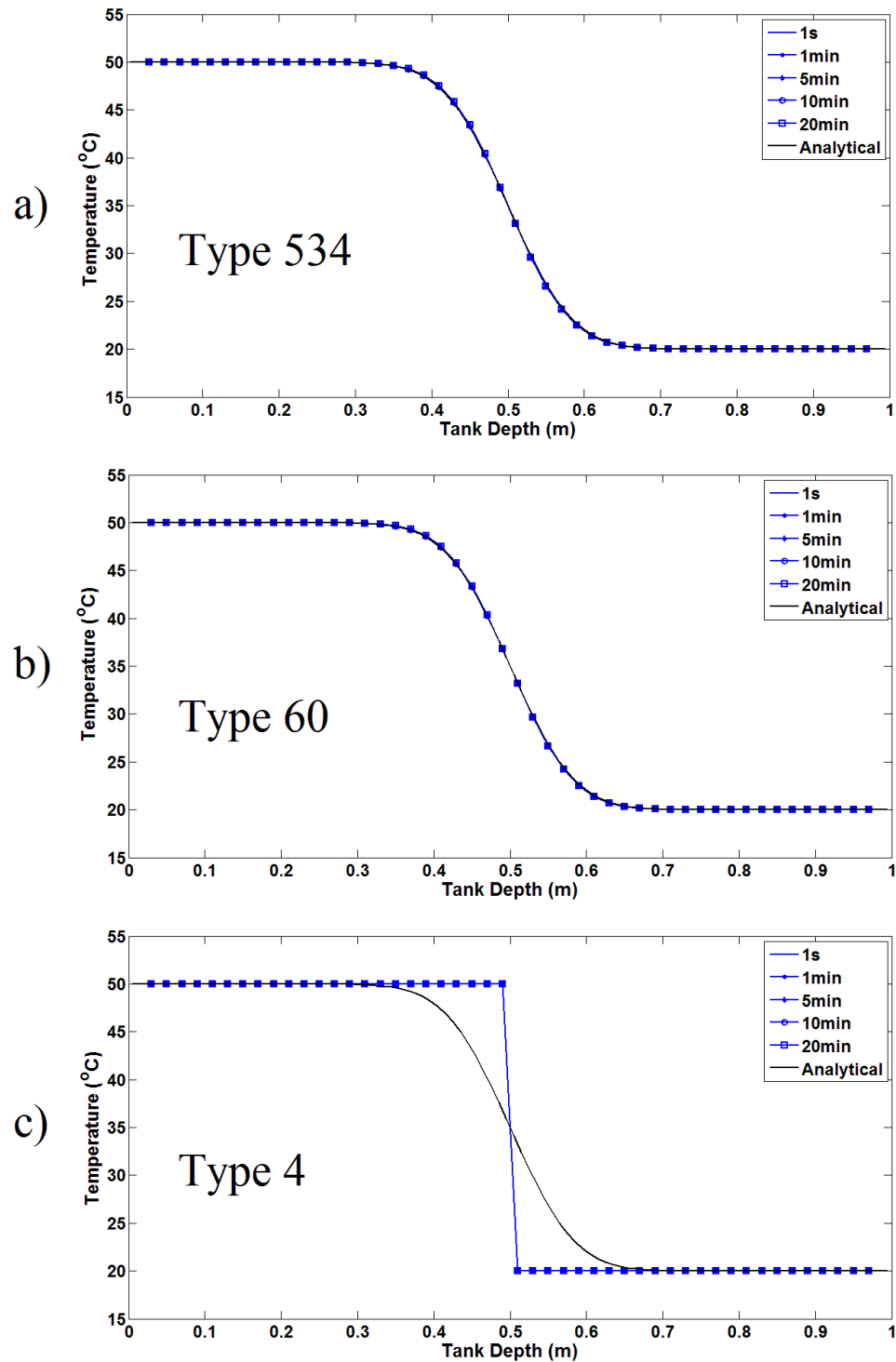


Figure 4.5 – Temperature vs tank depth results for Case 2 after 4 hours with varying time step sizes and 50 nodes. (a) Type 534 model, (b) Type 60 model, (c) Type 4 model.

4.3.2 Case 2 Results

1) Sensitivity to Grid Spacing

Results for Case 2 with varying numbers of nodes are shown in Figure 4.6. The temperature profiles were plotted after 1 hour, which was when the center of the thermocline approached the middle of the tank. Therefore, the position of the thermoclines shown for Case 2 were roughly the same as Case 1. However, less time had passed, and thus less diffusion would have occurred. The analytical results show a steeper temperature profile with a smaller thermocline thickness.

The results from the three TRNSYS models show that when a flow was considered, numerical error was present and poor predictions were obtained from all of the models. The location of the thermocline was predicted correctly, since a plug flow is assumed by both the analytical and one-dimensional models, but the thermocline thicknesses were over predicted. This error increased as the number of nodes was reduced.

The over prediction of the thermocline thickness was a result of the errors that were introduced due to the numerical scheme. As the number of nodes increased, this error was reduced as the predicted thermocline thickness approached the analytical solution. The maximum RMS error found with the coarsest grid (10 nodes) was about 6.7°C and was reduced to 2.1°C with the smallest grid spacing (100 nodes). However, even when the maximum number of nodes allowed by TRNSYS was used (100 by default), there was still a significant amount of numerical error. The results also showed that the decrease in the error for 10 to 50 nodes appeared to be larger than the decrease for 50 to 100 nodes.

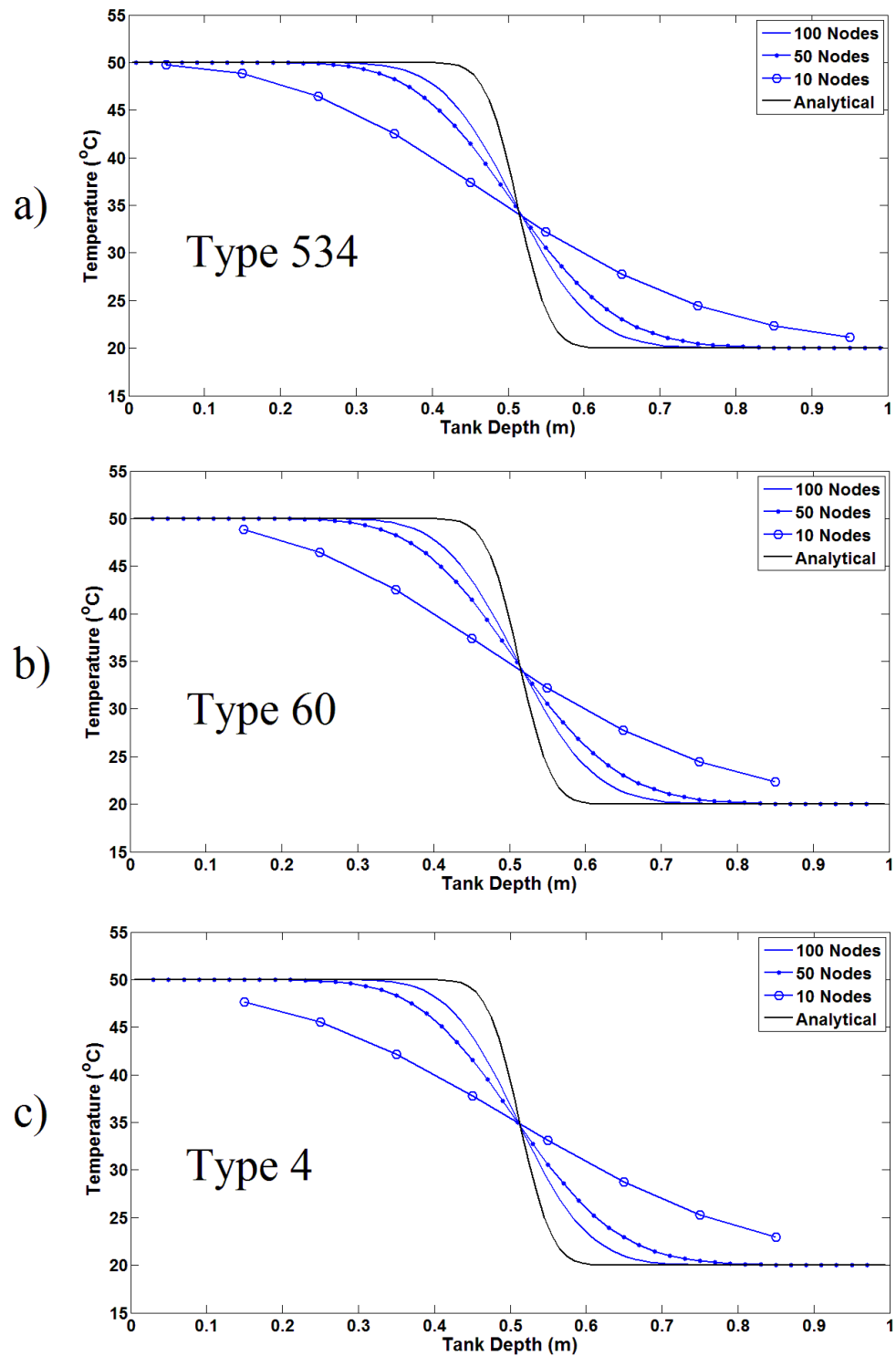


Figure 4.6 – Temperature vs tank depth results for Case 2 after 1 hour with varying numbers of nodes and 1 second time steps. (a) Type 534 model, (b) Type 60 model, (c) Type 4 model.

Therefore, since the error appears to follow a square root function, as given in Table B.1, in order to eliminate the numerical error, the number of nodes would likely have to be increased to a much larger value.

For this case, the Type 4 model also showed similar results as the other TRNSYS models, as shown in Figure 4.6c. However, when considering the assumptions inherent in the Type 4 model (plug flow with negligible conduction), a perfectly stratified profile, as seen in the previous case was anticipated. Therefore, even though the results of the Type 4 model resemble the type of solution that would be expected from a one-dimensional model, the temperature profiles obtained were a result of the numerical error created by the solution scheme. This was also found from the RMS errors plotted in Appendix B. When a smaller grid spacing was used, the Type 4 model showed lower RMS errors because less diffusion was experienced. If enough nodes were used with the Type 4 model, the results would resemble a step-function.

2) Sensitivity to Time Step Size

It was mentioned previously that the TRNSYS one-dimensional models all output time-averaged node temperatures at the end of each time step, rather than the exact nodal temperature at the end of the time step. For small time steps, the difference between those temperatures is small, but at larger time steps, there may be a significant difference. Therefore the simulated profiles would not match with the theoretical profiles plotted with the analytical model when larger time steps were considered.

Figure 4.7 shows a comparison of the analytical and simulated results for Case 2 with varying time step sizes after 1 hour. At the smaller time steps of 1 second and 1 minute, the locations of the thermoclines matched with the theoretical profile because the plotted temperatures were averaged over a very small amount of time. However, as the time step size increased, the locations of the simulated thermoclines were incorrect.

These incorrect profiles were not experienced in the previous simulations because of the simulation conditions. For Case 1, only diffusion was considered with no flow through the tank. Therefore, the thermocline was not moving with each time step and the change in temperature of each node was much smaller for each time step. The results for Case 2 with varying numbers of nodes did not show this error because the selected time step size of 1 second was very small.

In order to visualize the effect of the time step size on the simulation accuracy, the temperature profiles were plotted at half of a time step ahead of the actual time. This was calculated using Eq. (4.8) where i represents the considered node, k represents the current time step, T is the desired node temperature, and $T_{average}$ is the time-averaged node temperature obtained from the TRNSYS results. This equation does not give the actual node temperature after the time step, but it provided a simple method to align the thermoclines for each of the simulations such that the temperature profiles could be compared and inspected for numerical error.

$$T_i^k = \frac{1}{2} (T_{average,i}^k + T_{average,i}^{k+1}) \quad (4.8)$$

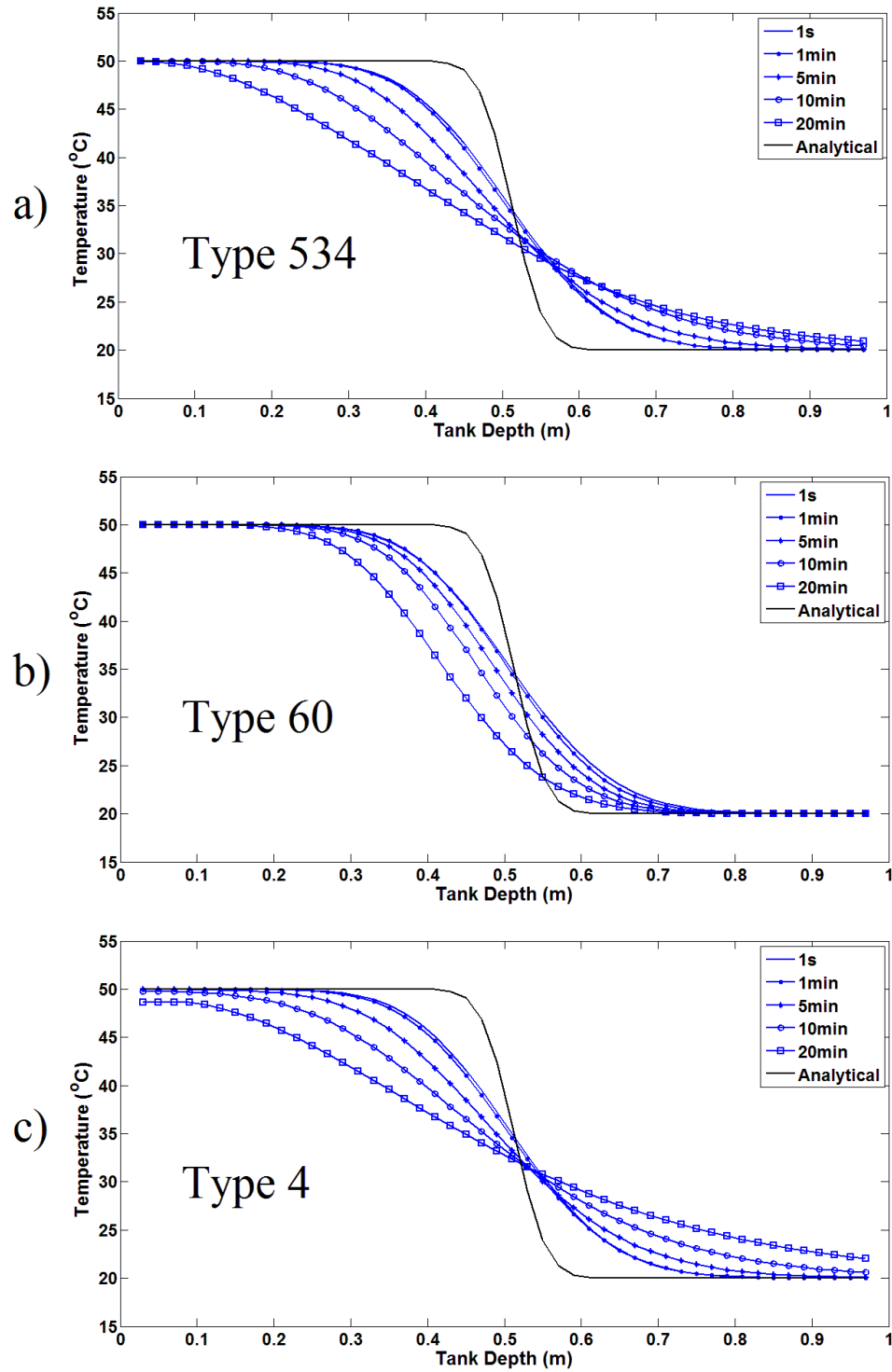


Figure 4.7 – Temperature vs tank depth results for Case 2 after 1 hour for varying time step sizes and 50 nodes. Plotted model results show the time-averaged nodal temperatures. (a) Type 534 model, (b) Type 60 model, (c) Type 4 model.

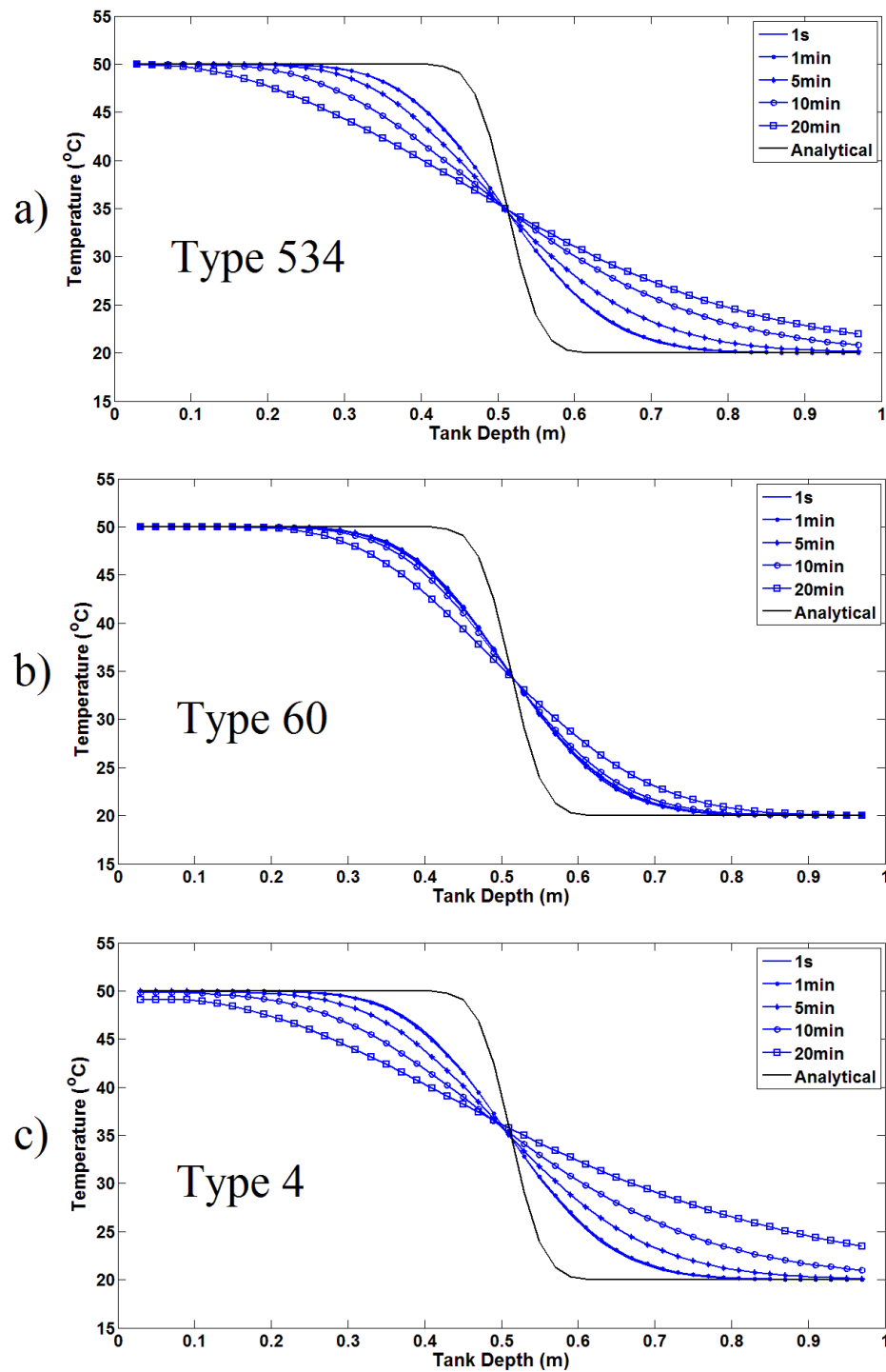


Figure 4.8 – Temperature vs tank depth results for Case 2 after 1 hour with varying time step sizes and 50 nodes. Plotted model results are time-average nodal temperatures at half a time step ahead to compare with analytical results. (a) Type 534 model, (b) Type 60 model, (c) Type 4

Figure 4.8 shows the predicted results for varying time step sizes after 1 hour. The Type 534 and Type 4 models showed that as the time step size decreased, a higher level of accuracy was obtained. Maximum RMS errors of 6.4°C and 7°C were found for the Type 534 and Type 4 models, respectively, with the largest time step size. The results also show that there was a very small change in the profiles between time step sizes of 1 minute and 1 second. This means that a time step convergence was obtained such that further refinement would have led to a very small decrease in the error. The results did not match with the analytical results after time step convergence was obtained because the simulations all used 50 nodes. Therefore, the minimum RMS error experienced for these two models was about 3°C due to the lack of grid convergence.

Different results were observed with varying time step sizes for the Type 60 model, as shown in Figure 4.8b. The temperature profiles were very similar for most of the tested time step sizes. This was because the Type 60 model used internal time steps to calculate the time averaged temperature values for each node at the end of the time steps, as described in section 3.1.1. Even when a larger time step size was used, the model calculated the temperatures after each internal time step between the specified simulation time steps. Therefore, a better approximation of the time-averaged node temperatures at the end of the simulation time steps was obtained and the use of internal time steps resulted in an overall reduction in time step sensitivity.

4.4 Numerical Diffusion Analysis

Since the TRNSYS models were not able to produce results that agreed with the analytical solution for Case 2 with a fluid flow, a more in-depth analysis of the solution schemes was required in order to determine the main causes for the numerical error that occurred. In particular, the sensitivity to grid spacing was analyzed. An in-house one-dimensional code was used to simulate Case 2 with more nodes than the amount that was allowed with the TRNSYS simulations. A Taylor series expansion was also performed on the energy equation to determine an expression for the numerical error experienced.

4.4.1 In-House One-Dimensional Code Comparison

The one-dimensional code used to simulate Case 2 with more nodes was similar to the TRNSYS models. It was a multi-node model which used an implicit scheme to solve for the temperatures at each node location with time. This code allowed for Case 2 to be simulated with an unlimited number of nodes. Therefore, the number of nodes required to obtain an accurate solution with grid convergence could be observed.

Simulation results using this code are shown in Figure 4.9. Figure 4.9a) shows a comparison of the in-house code results and the TRNSYS Type 60 model for 50 and 100 nodes after one hour into the simulation. Both of the models used a time step size of 1 second. The figure shows excellent agreement between the in-house code predictions and that obtained from TRNSYS using the same time step and grid spacing. This indicates that the in-house code used for these simulations could be used to explore the performance of

the TRNSYS Type 60 tank model without the node limitation imposed by the commercial code.

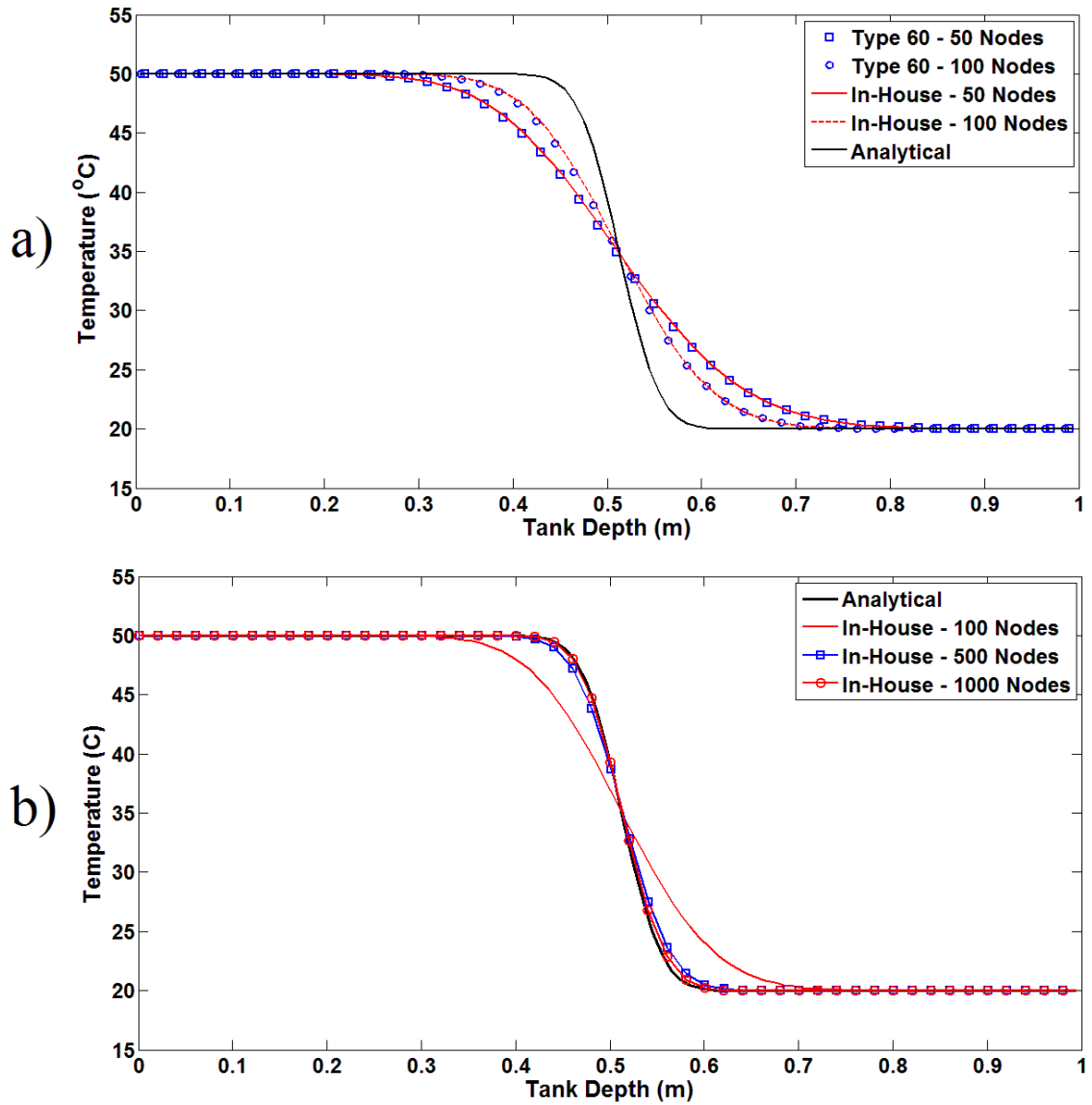


Figure 4.9 – Temperature vs tank depth results for Case 2 after 1 hour with an increasing amount of nodes and 1 second time steps. (a) shows the comparison between the TRNSYS Type 534 model and the in-house code up to the maximum of 100 nodes allowed by TRNSYS. (b) shows the in-house code results for 100 to 1000 nodes.

Figure 4.9b) shows the results of the in-house code for Case 2 using 100, 500, and 1000 nodes. A similar trend was shown as the amount of error between the numerical and analytical results decreased as the number of nodes was increased. However, 1000 nodes was required to obtain results that matched well with the analytical solution. This number of nodes would not be feasible for a larger system simulation because the computational cost would be too large.

In conclusion, the TRNSYS one-dimensional models would be able to predict the theoretical temperature profiles if the maximum number of nodes allowed by TRNSYS was increased. However, the use of more nodes would lead to increased computational time, which is not desired in the context of performing annual simulations of solar thermal systems, particularly if multiple tanks are included in the system.

4.4.2 Taylor Series Expansion of the Discretized Energy Equation

To determine the dependence of the numerical error on the simulation parameters, a Taylor series expansion was performed on the one-dimensional, unsteady, convection/diffusion energy equation, Eq. (4.9), using the discretization methods implemented by the TRNSYS Type 60 model. The discretizations for each of the terms using the Crank-Nicolson scheme with central differencing are shown in Table 4.3. In these equations, i represents the current node, k represents the current time step, α represents the fluid diffusivity, and u represents the mean velocity of the fluid over the tank cross-section ($u = \dot{m}_{in}/\rho A_c$).

$$\frac{\partial T}{\partial t} = \alpha \frac{\partial^2 T}{\partial x^2} - u \frac{\partial T}{\partial x} \quad (4.9)$$

Table 4.3 – Discretizations used by the Type 60 model for each of the terms in the one-dimensional, unsteady, convection/diffusion energy equation. The Crank-Nicolson scheme was implemented for each node.

Term	Discretization
$\frac{\partial T}{\partial t}$	$\frac{T_i^{k+1} - T_i^k}{\Delta t}$
$\alpha \frac{\partial^2 T}{\partial x^2}$	$\frac{\alpha}{2\Delta x^2} (T_{i+1}^{k+1} - 2T_i^{k+1} + T_{i-1}^{k+1} + T_{i+1}^k - 2T_i^k + T_{i-1}^k)$
$u \frac{\partial T}{\partial x}$	$\frac{u}{2\Delta x} (T_i^{k+1} - T_{i-1}^{k+1} + T_i^k - T_{i-1}^k)$

These discretized terms were combined together and Taylor series expansions were used to convert all of the temperatures to be in terms of the current node, i , and the current time step, k . The original energy equation terms were then extracted such that the remaining terms made up the numerical error created by the discretization method. Additional details of this process are shown in Appendix C. Therefore, the error for the current node at the current time step is given by Eq. (4.10) in terms of the fluid velocity (u), diffusivity (α), node size (Δx), time step size (Δt), and the derivative terms.

$$\begin{aligned}
 E_i^k = & -\left(\frac{u\Delta x}{2}\right) \frac{\partial^2 T}{\partial x^2} \Big|_i^k + \left(\frac{u\Delta x^2}{6} + \frac{u^3\Delta t^2}{12}\right) \frac{\partial^3 T}{\partial x^3} \Big|_i^k \\
 & - \left(\frac{\alpha\Delta x^2}{12} + \frac{\alpha u^2\Delta t^2}{2} + \frac{\alpha u\Delta x\Delta t}{4} + \frac{u^3\Delta x\Delta t^2}{8} \right. \\
 & \left. + \frac{u^2\Delta x^2\Delta t}{12}\right) \frac{\partial^4 T}{\partial x^4} \Big|_i^k + \dots
 \end{aligned} \quad (4.10)$$

The first term in Eq. (4.10), which involves the second derivative of the temperature with respect to position, would have a large effect on the overall numerical error and the only variables that effected this term were the velocity and the grid spacing, Δx . This makes sense because if the fluid velocity was reduced, less fluid from the previous node would enter the current node after a single time step and less numerical diffusion would occur. Also, as seen from the case study results, when the number of nodes was increased, which would lead to a smaller Δx , the numerical error was reduced.

The dependence on the time step size was also shown in Eq. (4.10). The second term contains an expression with Δt^2 . The solution scheme is therefore second order accurate in time, meaning that as the time step is reduced by half, the numerical error present in the energy equation prediction is expected to be reduced by one-quarter. As such, the grid spacing is expected to have a larger impact on the error in comparison to the time step. These conclusions are consistent with the observations from Case 2 since larger errors were experienced with varying grid spacing.

The first term also revealed information about how much additional diffusion was experienced from the simulation results. This term involved the second derivative of the node temperature, T , with respect to position, x . Therefore, it could be considered as an additional diffusion term that was added to the fluid diffusion in the energy equation, as shown in Eq. (4.12). The variables in front of the first term, $u\Delta x/2$, would then become the additional, numerical diffusivity, $\alpha_{numerical}$, as shown in Eq. (4.13). The actual diffusivity experienced in the one-dimensional model simulations would be the sum of the fluid diffusivity and the numerical diffusivity obtained from the solution scheme of the

Type 60 model. A similar term could be obtained with a Taylor series expansion of the other models.

$$\alpha_{numerical} = \frac{u\Delta x}{2} \quad (4.11)$$

$$\frac{\partial T}{\partial t} = \alpha \frac{\partial^2 T}{\partial x^2} - u \frac{\partial T}{\partial x} + \left(\frac{u\Delta x}{2} \right) \frac{\partial^2 T}{\partial x^2} = \alpha_{simulation} \frac{\partial^2 T}{\partial x^2} - u \frac{\partial T}{\partial x} \quad (4.12)$$

$$\alpha_{simulation} = \alpha_{fluid} + \alpha_{numerical} = \alpha + \frac{u\Delta x}{2} \quad (4.13)$$

The importance of this numerical diffusivity on the accuracy of the results can be determined using the nodal Peclet number, Eq. (4.14). This dimensionless grouping represents the ratio between the amount of diffusion created by the numerical scheme and the diffusion created by the fluid. Ideally, the nodal Peclet number would be small (~ 1) to reduce the effect of numerical diffusion. However, for Case 2 studied previously, the Peclet number for all of the tests was large (~ 10 with the use of 100 nodes). Therefore, the numerical diffusivity had a much larger effect on the results than the fluid diffusivity, causing a significant amount of additional diffusion. This also explains why the Case 2 results for the Type 4 model were similar to the other models while for Case 1, the results were different. The effect of the numerical diffusion was larger than the effect of diffusion caused by the fluid conductivity. Therefore, even though the Type 4 model did not consider conduction, similar results were obtained since the amount of numerical diffusion that had occurred after 1 hour was much more than the diffusion caused by the conduction between the hot and cold regions.

$$Pe = \frac{\alpha_{\text{numerical}}}{\alpha} = \frac{u\Delta x}{\alpha} \quad (4.14)$$

To evaluate the validity of this numerical diffusivity analysis, Eq. (4.13) was used to determine a new diffusivity which represented the diffusion experienced by the one-dimensional models for varying amounts of nodes. This diffusivity was used for simulations of Case 2 with the analytical model and the results were compared with the TRNSYS Type 60 model for varying numbers of nodes to determine if Eq. (4.13) gives that actual amount of diffusivity that was experienced by the one-dimensional models. The values of the diffusivities that were used for each of the simulations are shown in Table 4.4, where the mean fluid velocity for Case 2 was:

$$u = \frac{\dot{m}_{in}}{\rho A_c} = 1.425 \times 10^{-4} \text{ m/s} \quad (4.15)$$

Table 4.4 – Numerical and simulation diffusivities calculated for the use with the analytical model to show the additional diffusion created from the numerical error in the one-dimensional models.

Number of Nodes	Numerical Diffusivity (m^2/s) $\alpha_{\text{numerical}} = \frac{u\Delta x}{2}$	Simulation Diffusivity (m^2/s) $\alpha_{\text{simulation}} = \alpha_{\text{fluid}} + \frac{u\Delta x}{2}$
10	7.125×10^{-6}	7.280×10^{-6}
50	1.425×10^{-6}	1.580×10^{-6}
100	7.125×10^{-7}	8.675×10^{-6}

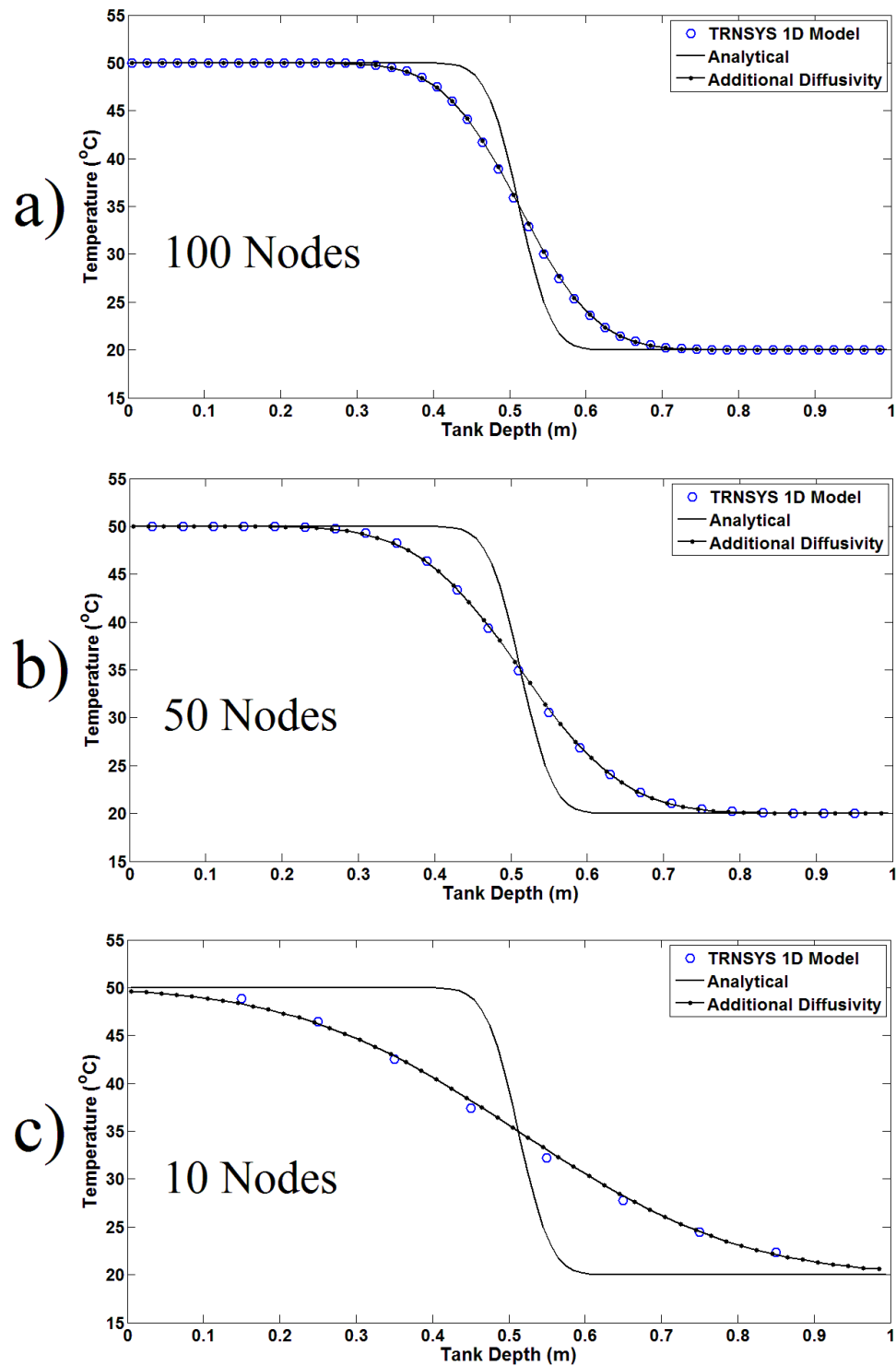


Figure 4.10 – Temperature vs tank depth results for Case 2 after 1 hour using 1 second time steps. The TRNSYS Type 60 results are compared with the analytical solution and the analytical solution with the additional diffusion. (a) 100, (b) 50, (c) 10 Nodes.

The results of these simulations are shown in Figure 4.10. These show that when the numerical diffusivity was added to the fluid diffusivity, and the analytical solution recalculated, the analytical temperature profiles agreed with the TRNSYS one-dimensional results. This confirmed that the errors that were experienced with the TRNSYS models were mostly a result of the numerical diffusion, given by the error equation obtained from the Taylor series expansion.

This also explains the results obtained by Chu [12] and Baldwin [13] where temperature profiles simulated with the TRNSYS models showed a lower level of stratification when compared with the experimental data. The expression for the numerical error shows that the errors can be reduced by increasing the amount of nodes used for the simulations. However, as discussed previously, a very large number of nodes would be required before an acceptable level of error was obtained. With the use of 100 nodes, the nodal Peclet number was about 10. Therefore, at least 1000 nodes would be required to reduce the numerical diffusivity to a similar order of magnitude as the fluid diffusivity, which is consistent with the findings shown in Figure 4.9 using the in-house code to model the tank with more nodes.

4.4.3 Comparison with Experimental Data (Chu [12])

The initial motivation for this research arose from the results of Chu [12] showing the differences between the experimental and simulation temperature profiles using a TRNSYS one-dimensional storage tank model. As discussed earlier, the TRNSYS simulations predicted less stratification than what was shown by the experimental results.

Therefore, the numerical error analysis proposed in this chapter was applied to the experimental conditions studied by Chu to determine if the results obtained from the TRNSYS models would be able to accurately predict the temperature profiles inside the tank if there was no numerical diffusion. The simulation parameters used are shown in Table 4.5. The inlet temperature was assumed to be constant for the analytical model simulations. However, the fluid entering the actual storage tank in the simulations performed by Chu came from the output of a heat pump. Therefore, the temperature of the inlet fluid would have varied slightly over the duration of the simulation.

Table 4.5 – Simulation conditions used for the analytical model to replicate the conditions tested by Chu [12].

Inlet Temperature, T_{in} ($^{\circ}C$)	50
Initial Temperature $T_{initial}$ ($^{\circ}C$)	20
Inlet Mass Flow Rate, \dot{m}_{in} (kg/s)	0.04875
Tank Height, H (m)	1.575
Tank Volume, V (m^3)	0.454
Inlet Pipe Diameter, D_p (m)	0.0254

The analytical solution, based on the semi-infinite wall solution, was shown earlier to be equivalent to the results that could be obtained by the TRNSYS models with a large number of nodes for conditions in which the semi-infinite wall solution was valid. Therefore it was used to compare the predicted temperature profiles with the experimental results. Figure 4.11 shows the comparison of the analytical results with the experimental and simulation results obtained by Chu. The temperatures were plotted at 5 different tank

heights for the duration of a single charging cycle (about 2.5 hours for this case). The highest location was at a depth of about 0.0788m and the distance between each location was about 0.3m. The black, dashed line indicates the thermocline center temperature such that the time at which the thermocline passes through each location could be observed. The purpose of this comparison was to assess the level of mixing seen in the experiments in comparison to an idealized case in which diffusion was the only heat transfer mechanism.

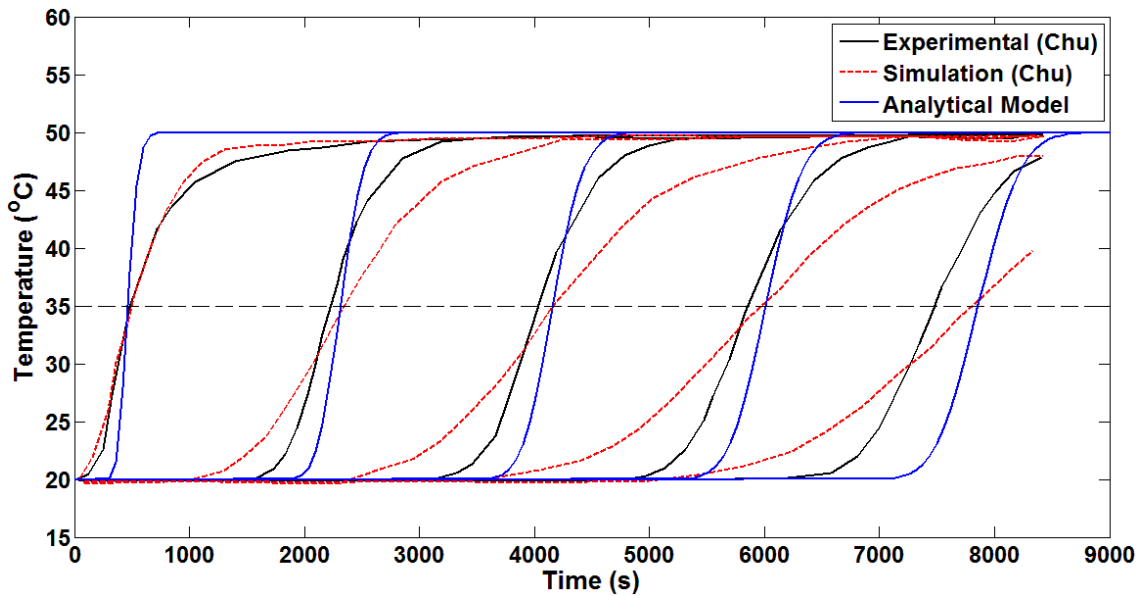


Figure 4.11 – Temperature vs time results at 5 different tank depths. The idealized analytical model results are compared with the experimental and simulation results obtained by Chu [12].

The analytical model results showed a higher level of stratification as the temperature at each location increased faster compared to the experimental and simulation results. The experimental results at the top of the tank had a slower increase in temperature compared to other locations due to the inlet jet mixing that occurred in the actual tank.

Therefore, the idealized analytical results showed more stratification since the additional mixing was not considered.

The thermoclines represented by the analytical model also appear to be in the incorrect locations later on in the simulation. This was also shown by the simulation results obtained by Chu. The centers of the thermoclines for the analytical results and simulation results, which occur when the temperature is equal to the average between the hot and cold temperatures (in this case, $35^{\circ}C$), do not match with the experimental thermoclines. This was likely also a result of the inlet jet mixing at the top of the tank. Due to the existence of the inlet jet, additional, turbulent mixing was created that led to varying fluid velocities and diffusion at the top of the tank. Nizami [17] described this inlet jet region as having a linear velocity profile in the axial direction with a maximum near the top of the tank and a minimum at the boundary of the inlet jet region, determined from the inlet jet penetration depth. This increased velocity was caused by the fluid entrainment into the inlet jet. Therefore, this would cause the thermocline to move through the tank at a different rate compared to the ideal plug flow case.

The numerical diffusion analogy was also tested with the conditions studied by Chu. The analytical model was simulated with a diffusivity equal to the sum of the fluid diffusivity and the numerical diffusivity calculated with Eq. (4.11). The results are shown in Figure 4.12. The temperature profiles given by the analytical model with additional diffusion showed similar levels of stratification and thermocline locations as the TRNSYS simulation results obtained by Chu.

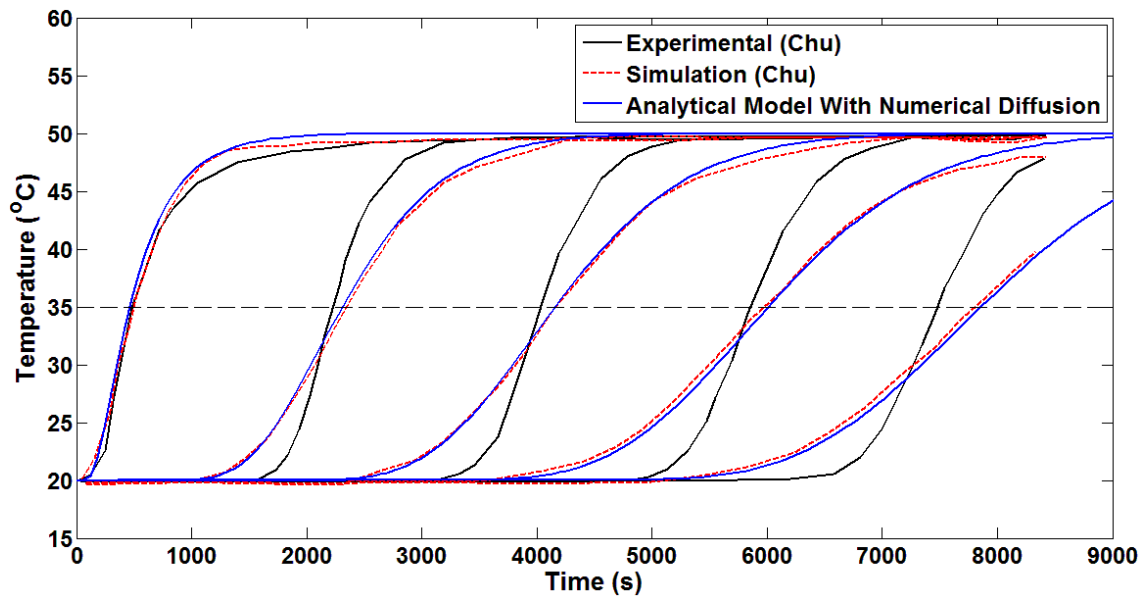


Figure 4.12 – Temperature vs time results at 5 different tank depths. The idealized analytical model results with additional numerical diffusion, calculated using the conditions studied by Chu, are compared with the experimental and simulation results obtained by Chu [12].

In conclusion, these results show that if a large number of nodes were to be used for the TRNSYS one-dimensional models, the analytical solution can be obtained, but these results would not always match with the temperature profiles of an actual thermal storage tank. This was because of the additional mixing mechanisms that exist in an actual tank which act to reduce the level of stratification. The location of the thermocline in an actual tank can also be affected by the additional mixing. Therefore, the temperature profiles predicted by a one-dimensional model would not always be in the correct location with time since a constant flow rate is assumed throughout the entire tank.

4.5 Conclusions

The case studies performed for this research revealed the main causes for the error introduced by the TRNSYS one-dimensional models. For the stagnant tank case in which only conduction was considered (Case 1), the Type 534 and Type 60 models were able to accurately predict the temperature profiles with time. Even when the number of nodes and time step sizes were varied, sufficiently accurate results were obtained compared to the analytical profiles. This was because there was no fluid motion through the tank and the conduction between the hot and cold regions occurred over a larger time scale.

The Case 1 results also showed the inaccuracies of the Type 4 model. Since this model does not calculate the conduction between the tank nodes, the temperature profiles did not change with time. The Type 4 model would still provide a simple analysis of the amount of hot fluid that is stored within the tank over time, however, the growth of the thermocline could not be modelled, which impacts the accuracy of the simulation of an entire solar thermal system.

The results from Case 2 show that errors were caused by the numerical treatment of the fluid flow through the tank. The error decreased when the number of nodes was increased and when the time step size was decreased. However, grid convergence was not obtained in the TRNSYS simulations due to the limitation of the maximum number of nodes in the tank. Therefore, none of the models were able to obtain the exact theoretical temperature profiles. Additional simulations with an in-house code were performed to show

that it would require about ten times as many nodes to obtain a more accurate result, which would be too computationally expensive for a large system model in TRNSYS.

A Taylor series expansion was also performed to explore the impact of the simulation parameters on the numerical error. It was found that the velocity and the node size have a very large effect on the error. These variables were shown to combine into a single term that acts as an additional diffusivity created by the numerical scheme. By adding this additional diffusivity to the fluid diffusivity in the analytical model, the theoretical results matched with the TRNSYS results, revealing that this was indeed the main cause of the numerical error.

Chapter 5

Development of Analytical Modelling Strategies

The previous chapter discussed the problems with using one-dimensional models to simulate the behaviour of thermal storage tanks. While they do provide a simple model that can be used in larger system simulations, they do not always perform well due to numerical error and the inherent simplifications of the physical mixing mechanisms. To alleviate the numerical error, a very large number of nodes is required, which would result in increased computational effort. Previous simulations performed by different researchers have shown agreement with experimental data because the additional diffusion created from the numerical error allowed the simulations to account for additional mixing mechanisms that were present in the experiments [40].

Therefore, this research looked into developing new modelling strategies that did not depend on a set of one-dimensional nodes. An analytical approach was used to model the storage tank behaviour which was developed from the semi-infinite wall solution, as discussed in section 3.2. This chapter will also discuss additional considerations that could be combined with the analytical solution to account for other mixing mechanisms that are not considered in previous one-dimensional models.

5.1 Idealized Analytical Solution

The idealized analytical solution used for this grid-less model was essentially identical to the solution used in Chapter 4 to compare with the TRNSYS model results. The

semi-infinite wall solution was used to model the diffusion between the hot and cold regions over time and the location of the calculated temperature profile was shifted depending on the predicted location of the thermocline center within the tank during charging. This model still assumed a one-dimensional profile since the temperature was assumed to be constant in the radial direction at each location.

The model first calculated the location of the thermocline with time. This was done by assuming that the thermocline moves at the mean tank fluid velocity, u_{tank} . The center of the thermocline, C , was then calculated with Eq. (5.2). For the simulations performed in this thesis, the inlet flow rate was constant. Therefore, the thermocline location was calculated as the product of the mean tank velocity and the simulation time.

$$u_{tank} = \frac{\dot{V}_{in}}{A_c} = \frac{\dot{m}_{in}}{\rho A_c} \quad (5.1)$$

$$C(t) = \int_0^t \frac{\dot{m}_{in}(t^*)}{\rho A_c} dt^* \quad (5.2)$$

The equation used to solve for the temperatures at any time and any location is shown below in Eq. (5.3). There are two different equations that are solved, depending on whether the point considered is above or below the thermocline center at the given simulation time. The variable, T_h , is the hot fluid temperature that enters the tank during a charging cycle, T_c is the cold fluid temperature that was initially in the tank, and T_{ave} is the average temperature $\left(\frac{1}{2}(T_h + T_c)\right)$.

$$\begin{aligned}
& T(x, t) \\
& = \begin{cases} T_{ave} + (T_c - T_{ave}) \operatorname{erf}\left(\frac{x - C}{\sqrt{4\alpha t}}\right) & \text{for } x > C \\ (T_c + T_h) - \left(T_{ave} + (T_c - T_{ave}) \operatorname{erf}\left(\frac{C - x}{\sqrt{4\alpha t}}\right)\right) & \text{for } x < C \end{cases} \quad (5.3)
\end{aligned}$$

The advantage of using this solution was that the temperature profile does not have to be calculated at specific time steps to acquire an accurate solution, like for the one-dimensional models. Since this model used an analytical approach, the temperature profiles could be calculated at any desired time and at any number of locations within the tank. The use of the analytical approach also reduced the amount of numerical error present in the model since the semi-infinite wall solution has been shown to accurately predict the thermocline behaviour with time.

5.2 Additional Considerations

The analytical solution discussed above only models the idealized temperature profiles in a thermal storage tank. Only the diffusion between the hot and cold regions is calculated throughout the simulation. However, as discussed previously, there are many other mixing mechanisms that lead to a loss of stratification, causing the analytical profiles to be incorrect. Therefore, methods of modelling these mechanisms analytically were explored such that they could be combined with the idealized analytical solution. This would create a more robust model that would be able to account for many different types of flows that could occur in a thermal storage tank.

5.2.1 Variable Inlet Temperatures

An important consideration for thermal storage tanks is the changes in the temperature of the inlet fluid with time. The temperature can change at different times of the day due to the amount of available solar energy that can be harvested by the collectors. Since the solar irradiation typically follows a cosine profile with time, as shown in Figure 1.2b), the temperature entering the tank increases in the morning until a solar noon is reached and then the temperature drops with the reducing solar irradiation.

Due to the use of time steps for one-dimensional simulations, the temperature of the fluid that enters the storage tank in the morning would jump to a higher value at the beginning of each time step, even though the temperature would be expected to increase at a continuous rate. For the analytical tank model, this would effectively create a new thermocline above the existing one since the higher temperature fluid, T_{h2} , enters the top of the tank that was at a slightly lower temperature, T_{h1} . To ensure that the correct amount of energy is added, compared to an actual storage tank with a continuously increasing inlet temperature, commercial codes use the average inlet temperature between the current and next time steps. This was also included in the current analytical model.

This effect was modelled using the same analytical concept from before and mathematical superposition of independent solutions. The initial thermocline, between temperatures T_{h1} and T_c , would progress through the tank at the same rate as before. When a higher temperature fluid enters the tank at a specific time, $t_{therm,2}$, a new thermocline, between temperatures T_{h2} and T_{h1} , would be calculated separately with a new thermocline

center location, C_2 , that started at the top of the tank at $t = t_{therm,2}$. The time used to calculate the position of the second thermocline, using Eq. (5.2), would be the current time subtracted by the time at which the inlet temperature increased, $t_2 = t - t_{therm,2}$. The following equations are used to calculate the two separate thermoclines:

$$T_1(x, t) = \begin{cases} T_{ave,1} + (T_c - T_{ave,1}) \operatorname{erf}\left(\frac{x - C_1}{\sqrt{4\alpha t}}\right) & \text{for } x > C_1 \\ (T_c + T_{h1}) - \left(T_{ave,1} + (T_c - T_{ave,1}) \operatorname{erf}\left(\frac{C_1 - x}{\sqrt{4\alpha t}}\right)\right) & \text{for } x < C_1 \end{cases} \quad (5.4)$$

$$T_2(x, t) = \begin{cases} T_{ave,2} + (T_{h1} - T_{ave,2}) \operatorname{erf}\left(\frac{x - C_2}{\sqrt{4\alpha t_2}}\right) & \text{for } x > C_2 \\ (T_{h1} + T_{h2}) - \left(T_{ave,2} + (T_{h1} - T_{ave,2}) \operatorname{erf}\left(\frac{C_2 - x}{\sqrt{4\alpha t_2}}\right)\right) & \text{for } x < C_2 \end{cases} \quad (5.5)$$

Where:

$$T_{ave,1} = 0.5(T_c + T_{h1}) \quad (5.6)$$

$$T_{ave,2} = 0.5(T_{h1} + T_{h2}) \quad (5.7)$$

$$C_1 = ut \quad (5.8)$$

$$C_2 = ut_2 \quad (5.9)$$

Figure 5.1 shows an example of two separate thermoclines plotted at the same instance of time. Thermocline 1 had already moved to the center of the tank when Thermocline 2 was introduced at the top due to an increase in the inlet temperature from

40°C to 50°C. Therefore Thermocline 1 had a larger thickness because more diffusion had occurred.

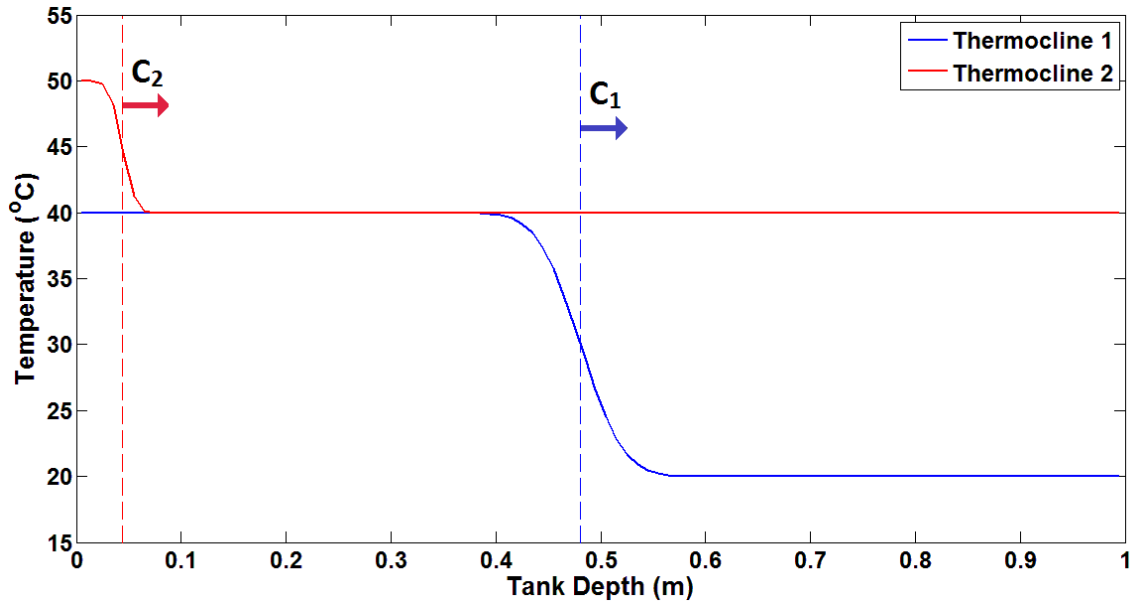


Figure 5.1 – Two thermoclines that are determined separately such that they can be combined using superposition to determine the overall temperature profile when the tank inlet temperature increases with time.

The two separate thermoclines were then added together using superposition to obtain the final temperature profile at the desired time. This was done by adding the initial profile to the second profile and subtracting the cold fluid temperature of the second profile (Eq. (5.10)), which in this case would be T_{h1} . This ensured that the profiles would be added together correctly when the individual thermoclines intersect as more diffusion occurs.

$$T_{final}(x, t) = (T_1(x, t) + T_2(x, t)) - T_{h1} \quad (5.10)$$

This process could be repeated for each time step that experienced an increase of the inlet fluid temperature. An example of this was simulated using the inlet temperature

data given in Table 5.1 at 600 second time intervals. The initial temperature of the fluid in the tank was set to 20°C and the inlet temperature started at 30°C . After each time step (600 s), the inlet temperature increased by 4°C until 3000 seconds and then remained constant at 50°C . As mentioned earlier, the analytical model uses the average inlet temperature for the duration of each time step instead of the temperature at the beginning of the time step to ensure the correct amount of energy is added to the tank. A charging mass flow rate of 0.01 kg/s was used.

Table 5.1 – Tank inlet temperatures at different times used for the simulation of the varying inlet temperature analytical model.

<i>Time (s)</i>	0	600	1200	1800	2400	3000
$T_{in} (^{\circ}\text{C})$	30	34	38	42	46	50

The results are shown in Figure 5.2. The first temperature profile for the analytical model plotted after 900 seconds shows the first two thermoclines added together to create a single temperature profile. As the simulation progressed, the width of these two thermoclines increased due to diffusion while additional thermoclines were created above them as the inlet temperature increased every time step (600s). After 4500 seconds, the first two thermoclines had intersected and created a more linear profile as more diffusion had occurred. Also, when the inlet temperature becomes constant, the profiles show a constant temperature at the top of the tank as the existing thermoclines move through the tank and diffuse with time.

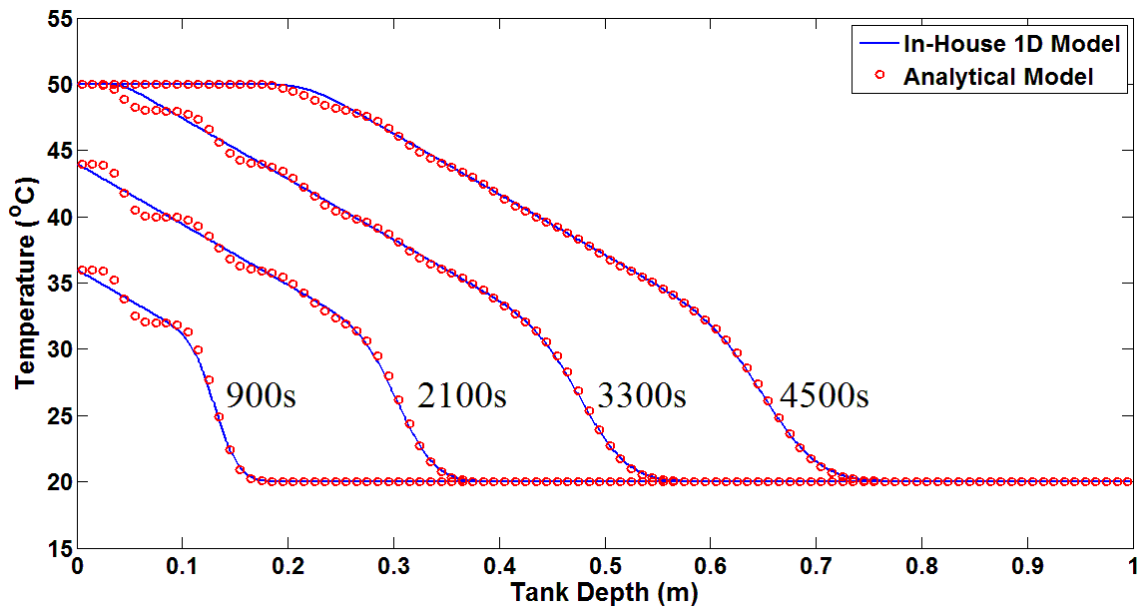


Figure 5.2 – Temperature vs. tank depth results after 900, 2100, 3300, and 4500 seconds for the analytical model (using 600 second time steps) and the in-house one-dimensional model (using 1 second time steps)

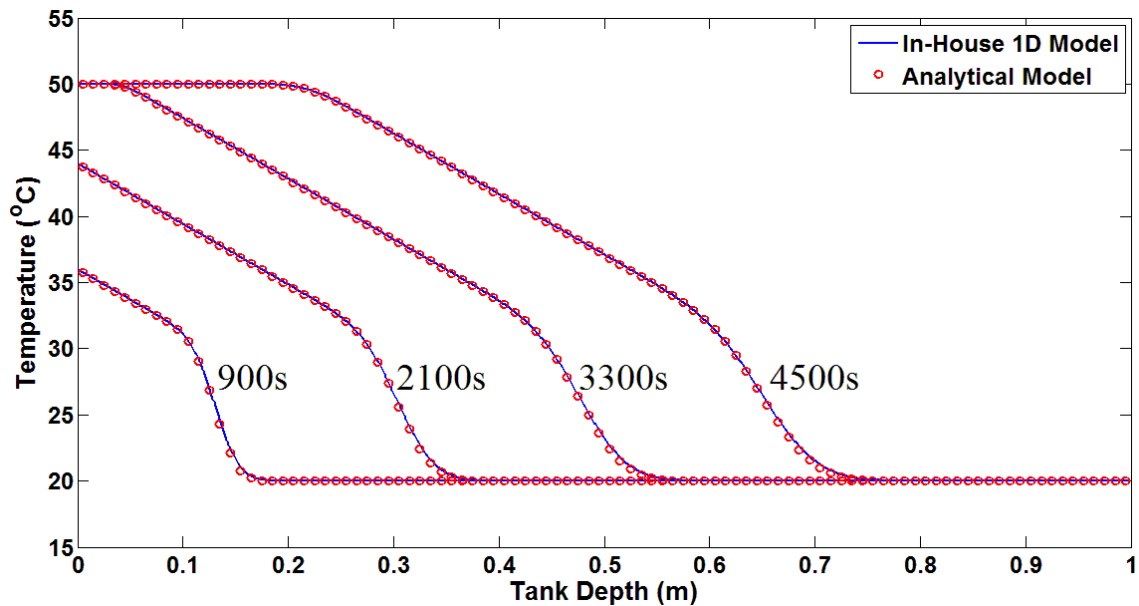


Figure 5.3 – Temperature vs. tank depth results after 900, 2100, 3300, and 4500 seconds for the analytical model (using 10 second time steps) and the in-house one-dimensional model (using 1 second time steps)

However, these profiles did not perfectly match with the expected profiles of an actual storage tank that would occur with a continuously increasing inlet temperature with time. This was simulated with the use of the in-house, one-dimensional model with 1000 equal volume nodes and one second time steps where the inlet temperature increased linearly with each time step (increased by $4/600^{\circ}\text{C}$ each step). With a larger time step size, the analytical model showed the correct amount of energy added to the tank but the thermocline profiles that were added together showed less diffusion. This was because the time intervals at which new thermoclines were created due to the increase in temperature were too large.

Figure 5.3 shows the results of the analytical model when the temperature was assumed to increase every 10 seconds instead of 600. This provided more accurate results since the increase in the inlet temperature for each time step was much smaller. Therefore, a larger number of additional thermoclines were calculated and added to produce a fuller profile and a better prediction was obtained. However, this would also lead to additional computational time.

This method would also not be applicable for a decreasing inlet temperature, which could be experienced later in the day as the amount of available solar energy decreases. The thermocline profiles could still be calculated and added together, but the final temperature profile would not be correct because plume entrainment would occur. Due to the lower density of the cooler temperature fluid entering the top of the tank, it would fall in the tank until it reached a similar temperature, causing additional mixing with the

surrounding hot fluid. This analytical model would only be able to plot the colder inlet fluid as a plug flow above the hotter region and not the effects of the fluid buoyancy.

5.2.2 Heat Losses to the Surroundings

The next mechanism that was considered was the heat losses to the tank surroundings. The TRNSYS one-dimensional models were able to consider this since it was calculated as another heat flow out of each node using the energy equation. However, an analytical approach was desired to obtain a higher accuracy. This was done by calculating new temperatures for the hot and cold regions with time as energy was lost to surroundings for a case with no fluid flow in the tank. The temperature of the fluid in the hot and cold regions would decrease as heat was lost.

Previous researchers who have studied tank heat losses, such as Abdoly and Rapp [30] and Oliveski et al. [18], considered storage tanks with no bulk fluid motion. As discussed previously, the effects of heat losses to the surroundings were much smaller compared to the advection during a charging cycle since it takes a longer period of time for there to be a significant change in the temperatures. Therefore, the analytical model for heat losses was developed for a stationary conduction case (Case 1).

The first challenge pertained to the calculation of the temperature profile with time was determining the shape of the profiles for each time step. At the beginning of each time step, the temperatures of the hot and cold regions will be different and the thermocline must be determined between the new temperature values. While the idealized analytical model

cannot account for this, the thermocline thickness, calculated from the idealized analytical model (as discussed in section 4.2), can be used to guide the temperature profile calculation.

After a thermocline profile is determined at the end of a simulation time step, the thermocline thickness can be calculated using Eq. (5.11). This was used to ensure that the thermocline thickness at the beginning of the next time step was the same when the new temperatures of the hot and cold regions, determined as a result of the heat losses, were used for the solution. To use the same analytical solution for the next time step, a new simulation time, t_{new} , needed to be calculated which corresponded to a temperature profile with the same thermocline thickness that was determined at the end of the previous time step, but existed between the new temperature values, $T_{c,new}$ and $T_{h,new}$. Eq. (5.11) was rearranged to solve for the time, t_{new} , as shown in Eq. (5.12). Therefore, the new simulation time that was used for the analytical model to calculate the temperature profile for the next time step would be $t_{new} + \Delta t$, where Δt is the time step size.

$$W_{therm,old} = 2\sqrt{4\alpha t_{old}} \operatorname{erf}inv\left(\frac{XT_{c,old} - T_{ave,old}}{T_{c,old} - T_{ave,old}}\right) \quad (5.11)$$

$$t_{new} = \left(\frac{1}{4\alpha}\right) \left(\frac{W_{therm,old}}{2 \left(\operatorname{erf}inv\left(\frac{XT_{c,new} - T_{ave,new}}{T_{c,new} - T_{ave,new}}\right)\right)}\right)^2 \quad (5.12)$$

The accuracy of this method would depend on the size of the time steps used because it was assumed that the temperature of the regions remained the same for the entire time step. Realistically, the temperatures would be changing constantly with time, which

would affect the growth rate of the thermocline. Therefore, with smaller time steps, the error in the assumption would be reduced. However, since the heat losses to the surroundings are typically small, this method still provides a good approximation and allows for the modelling of the temperature profile with varying hot and cold region temperatures.

The next challenge was to determine how the region temperatures change with time due to the heat losses to the surroundings. This was done by using Newton's Law of Cooling [29], as shown by Eq. (5.13), where T represents the value of the region temperature being solved for (either the hot region temperature, T_h , or the cold region temperature, T_c), T_∞ is the temperature of the surroundings, A_s is the wall surface area that is in contact with each of the fluid regions, and V is the volume of the regions. The surface area and the volume are written as Eq. (5.14) and Eq. (5.15), where L is the length of the regions and D is the tank diameter. Therefore, the energy balance was simplified to Eq. (5.16).

$$\rho C_p V \frac{dT}{dt} = -h A_s (T - T_\infty) \quad (5.13)$$

$$A_s = \pi D L \quad (5.14)$$

$$V = \frac{\pi}{4} D^2 L \quad (5.15)$$

$$\frac{dT}{dt} = -\frac{4h}{\rho C_p D} (T - T_\infty) \quad (5.16)$$

The initial condition used to solve this differential equation would be the initial region temperature, T_o . Therefore, the hot and cold region temperatures were solved for separately as functions of time, as shown below.

Initial conditions: $T_h(t = 0) = T_{h,0}$, $T_c(t = 0) = T_{c,0}$

$$T_h(t) = T_\infty + (T_{h,0} - T_\infty) \exp\left(-\frac{4h}{\rho C_p D} t\right) \quad (5.17)$$

$$T_c(t) = T_\infty + (T_{c,0} - T_\infty) \exp\left(-\frac{4h}{\rho C_p D} t\right) \quad (5.18)$$

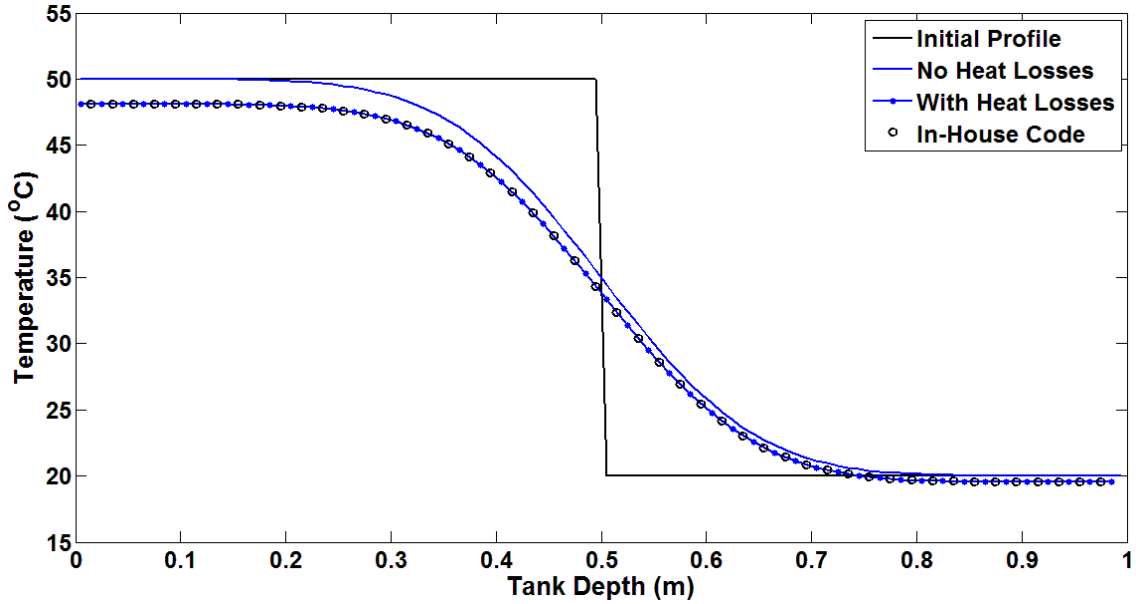


Figure 5.4 – Temperature vs tank depth results for the previous Case 1 conditions after 12 hours with the additional effects of heat losses to the surroundings calculated by the heat losses analytical model.

Using the conditions of Case 1 from Chapter 4, which initially consisted of hot water in the top half of the tank at 50°C and cold water in the bottom half at 20°C , the analytical model was used to simulate the performance of a tank with 300 second time

steps, a heat transfer coefficient of $h = 0.34 \text{ W/m}^2\text{K}$, and the surroundings at a temperature of 10°C . The results were compared with the same in-house one-dimensional model that was used in section 3.4.1. Figure 5.4 shows the temperature profiles after 12 hours when a significant amount of diffusion and heat losses to the surroundings had occurred. The results from the idealized analytical model with no heat losses are also plotted to show the difference between the different solutions.

The temperature profiles show that the analytical model that considered the heat losses to the surroundings agreed with the one-dimensional model results which used a large number of nodes. The temperature of the hot fluid at the top of the tank and the cold fluid at the bottom of the tank decreased as a result of the heat losses to surroundings which were at a lower temperature. Therefore, this model could be used to predict heat losses when there is no flow in the tank, i.e. when no charging or discharging occurs. This method would not be valid with fluid flow because hot fluid would constantly be entering the top of the tank. Therefore, the temperature of the hot region would not decrease as much and the very top of the tank would be at a higher temperature due to the buoyancy of the inlet fluid.

However, the decrease in the hot and cold region temperatures due to the heat losses to the surroundings would not always be significant for the time scale considered for the charging of a tank. The previous example showed the difference between the idealized case and the case with heat loss after 12 hours. For comparison, the charging of the tank considered previously in Chapter 4 (Case 2) only took about 2 hours. The decrease in the hot region temperature due to heat losses after 2 hours would only be about 0.32°C or

0.64% of the original hot region temperature. Therefore, the effect of the heat losses to the surroundings during charging or discharging could be neglected for some cases and the current model would be implemented when there is no fluid flow, such as when hot fluid is being stored in the tank for longer periods of time.

5.2.3 Tank Wall Conduction

The additional heat transfer created due to the conduction through the tank wall was modeled similarly to the method used for heat losses to the surroundings. The temperatures of the hot and cold regions were assumed to change with time due to the heat transferred through the storage tank walls. The temperature of the fluid in the hot region would decrease over time. However, the temperature of the fluid in the cold region would now increase as heat is conducted through the wall from the hot region.

To calculate the change in these temperatures over time, the analogy used by Lightstone [19] was implemented. This method, as described in section 2.1.3, treated the wall as a fin which acts to enhance the heat transfer between the hot and cold regions. Therefore, assuming that the temperature of the wall is equal to the average tank fluid temperature, the heat transfer into the wall from the hot region and out of the wall into the cold region was determined using Eq. (5.19) where ΔT is the temperature difference between the wall and the tank region being considered, h is the convective heat transfer coefficient between the wall and the tank fluid, P is the inner tank perimeter, k_{wall} is the thermal conductivity of the wall, and $A_{c,wall}$ is the cross-sectional area of the wall.

$$\dot{Q}_{wall} = \sqrt{hPk_{wall}A_{c,wall}} \frac{\Delta T}{2} \tanh\left(\sqrt{\frac{hP}{k_{wall}A_{c,wall}}} \frac{H}{2}\right) \quad (5.19)$$

Using this heat transfer equation, the temperature of the hot and cold regions were determined using the differential equation given by Eq. (5.20). The initial hot and cold region temperatures were used as the initial conditions to find two equations for $T_h(t)$ and $T_c(t)$ with time. All of the properties in Eq. (5.19) were collected and written as a single constant variable, C_{whc} .

$$\rho C_p V \frac{dT}{dt} = \dot{Q}_{wall} \quad (5.20)$$

$$\begin{aligned} \rho C_p V \frac{dT}{dt} &= -\frac{\sqrt{hPk_{wall}A_{c,wall}}}{2} \tanh\left(\sqrt{\frac{hP}{k_{wall}A_{c,wall}}} \frac{H}{2}\right) (T - T_{wall}) \\ &= C_{whc} (T - T_{wall}) \end{aligned} \quad (5.21)$$

$$T_h(t) = T_{wall} + (T_{h,o} - T_{wall}) \exp\left(-\frac{C_{whc}}{\rho C_p V} t\right) \quad (5.22)$$

$$T_c(t) = T_{wall} + (T_{c,o} - T_{wall}) \exp\left(-\frac{C_{whc}}{\rho C_p V} t\right) \quad (5.23)$$

Table 5.2 – Steel tank wall dimensions and thermal properties used for the tank wall heat conduction analytical model simulations.

Wall Thickness (d)	0.01 m
Convective Heat Transfer Coefficient (h_{wall})	1.5 W/m ² K
Thermal Conductivity (k_{wall})	45 W/mK

The same technique used for calculating the temperature profile with varying hot and cold region temperatures described in section 5.2.2 was used to calculate the profiles for the tank wall conduction case. The case of simple conduction (Case 1) was again studied to show the effectiveness of this analytical model for calculating the profiles when tank wall conduction was present. The tank was initially stratified with 50°C water in the top half and 20°C water in the bottom half. The properties for a steel wall used for this simulation are shown in Table 5.2.

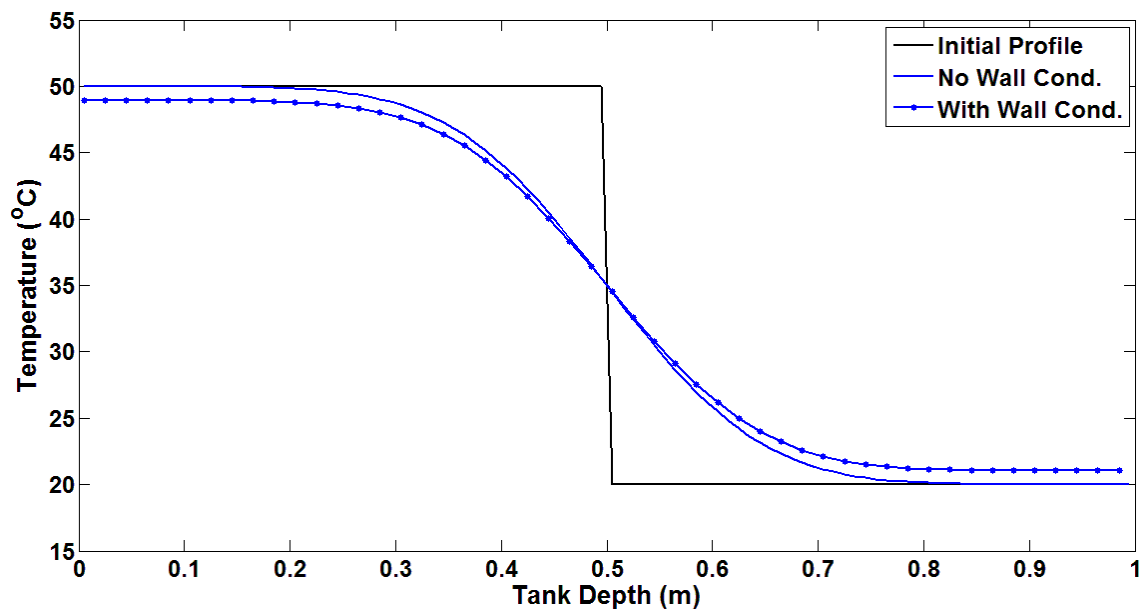


Figure 5.5 - Temperature vs tank depth results for the previous Case 1 conditions after 12 hours with the additional effects of tank wall heat conduction calculated by the wall conduction analytical model.

Figure 5.5 shows the results of the simulation after 12 hours. The temperature of the hot water at the top of the tank decreased and the temperature of the water at the bottom of the tank increased as a result of the heat transferred through the wall. Similar to the case with heat losses to the surroundings, the change in the region temperatures after 12 hours

was small. Therefore, this solution for tank wall heat conduction could be implemented only when there was no tank flow since the change in the region temperatures occurred over a larger time scale.

5.2.4 Inlet Jet Mixing

The modelling of the mixing effects caused by the inlet jet was important because it can lead to significantly different temperature profiles, as experienced by Oliveski et al. [18] and Leohrke and Holzer [20]. This additional mixing can lead to lower expected temperatures at the top of the tank compared to the temperature of the inlet fluid. Therefore, a plug-flow could not be considered as the tank is charging with a hot fluid. This was also a mechanism that the current TRNSYS one-dimensional models do not consider.

Inlet jet mixing effectively creates a region at the top of the tank (the inlet mixing region) that contains different flow characteristics compared to the rest of the tank. This leads to additional mixing between the hot inlet fluid and the initial cold fluid within the tank. As shown by the simulations performed by Oliveski et al. and Nizami et al. [17] (Figure 2.3 and Figure 3.4), the temperature and velocity of the fluid in the inlet mixing region varied in both the axial and radial directions as a result of the inlet jet penetration and the recirculation of fluid. The temperature in the rest of the tank only varied in the axial direction as the fluid flow was more uniform.

Nizami used 2D-axisymmetric simulations to visualize the flow patterns and temperature contours within a storage tank at different times during charging. The results were shown previously in Figure 3.5. These simulations revealed that a turbulent,

recirculation zone was created as surrounding fluid was entrained into the jet. Fluid from the jet that mixed with the surrounding fluid traveled upwards since the hotter fluid had a lower density. As more hot fluid entered the tank, the inlet mixing region filled with hotter fluid, but with a different velocity field and fluid properties than the rest of the tank due to the recirculation.

Additional 2D-axisymmetric simulations were performed for the case studied by Nizami to obtain more information about how the temperature of the fluid in the inlet mixing region changed at the beginning of a charging cycle. Details of the tank mesh and conditions used for the simulation are discussed in Appendix E.1.

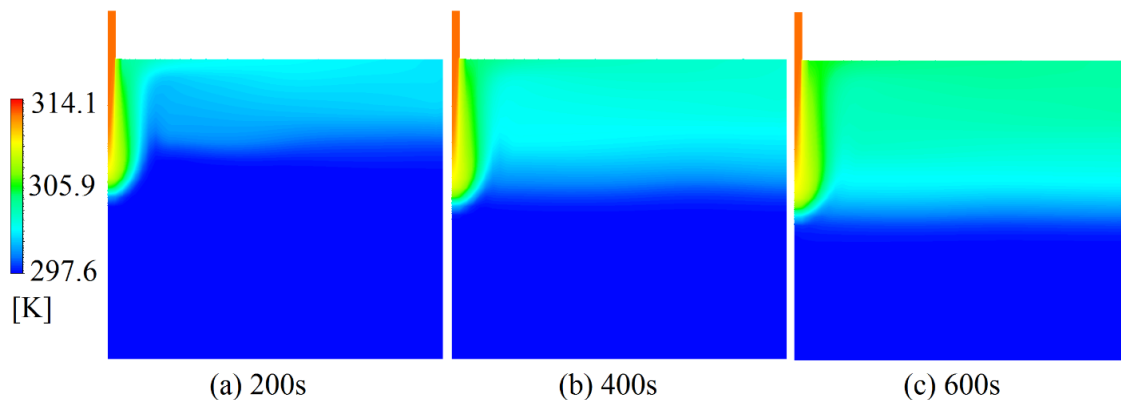


Figure 5.6 – Temperature contours of the inlet jet region for the conditions studied by Nizami et al. [17] after (a) 200s, (b) 400s, and (c) 600s, showing the formation of a thermocline within the inlet jet region.

The results, shown in Figure 5.6, reveal that the hot inlet fluid that recirculates to the top of the tank creates a thermocline within the inlet mixing region that travels downwards as more hot fluid enters the tank. After 200 seconds, there was a warm fluid region at the top of the tank and a cold region below. As time increased, the warm region expanded as more hot fluid entered the tank and showed a similar behaviour as a typical

thermocline. However, the velocity at which this thermocline moved through the inlet mixing region was different than the mean tank fluid velocity due to the jet entrainment.

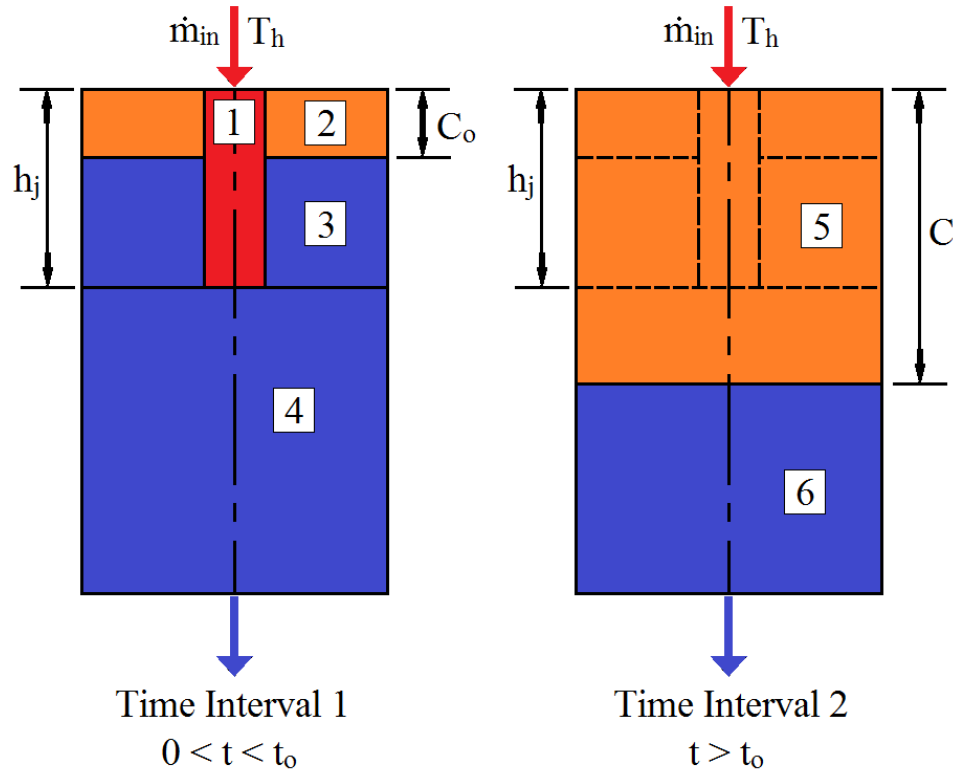


Figure 5.7 - Schematic of the constant temperature regions defined for time intervals 1 and 2 that are used to determine the temperature profile within the tank over time. For time interval 1, the tank is divided into 4 regions: (1) jet region, (2) inlet mixing hot region, (3) inlet mixing cold region, and (4) cold tank region. For time interval 2, the tank consists of 2 regions: (5) hot tank region and (6) cold tank region.

To analytically model the temperature profile behaviour with time for this scenario, the solution was divided into two different time intervals. The first time interval (for $0 < t < t_o$) was used to calculate the temperature profile while the thermocline resided within the inlet mixing region. The time at which this time interval ended (t_o) would be when the center of the initial thermocline reached the edge of the inlet mixing region, which would

be equal to the inlet jet penetration depth, h_j . This is the location where the velocity of the fluid is equal to the mean tank fluid velocity since there are no turbulent effects. The second time interval would exist for the rest of the charging time (for $t > t_o$) while the thermocline moves throughout the rest of the tank at the normal tank velocity. A visualization of these two time intervals is shown in Figure 5.7.

To model the temperature profile for time interval 1, the tank was divided into different regions, similar to the work done by Nizami et al. [17], as explained in section 3.1.2. However, the regions defined for this work considered separate constant temperature regions, whereas the model developed by Nizami divided the tank into regions with different flow patterns, which each contained a series of one-dimensional nodes in the axial direction, as shown in Figure 3.5 and Figure 3.6. Region 1 for the current work was determined to be the same as region δ_1 defined by Nizami, which was the region that contained the inlet jet and the fluid that rises to the top of the tank. However, the remaining tank regions for this work were defined differently to simplify the solution. Nizami assumed that the axial flow rate in region δ_3 had a linear distribution with a maximum at the top of the region to a minimum of \dot{m}_{in} at the bottom since flow was entrained into the jet region, δ_1 , from each node used to discretize region δ_3 . The current work only used 2 fully mixed temperature regions to define the region beside the inlet jet where the axial flow rate was assumed to be constant and equal to the summation of the inlet and entrainment flow rates ($\dot{m}_p = \dot{m}_{in} + \dot{m}_{ent}$).

Region 2 included the hot fluid that was brought to the top of the tank and gets redirected downwards. This region made up the hot region of the thermocline in the inlet mixing region where the volume increases as more hot fluid enters the tank. Region 3 contained the initial cold tank fluid that still existed in the inlet mixing region for the duration of time interval 1. Fluid from this region is entrained into the inlet jet and was defined as the cold region for the thermocline. Finally, Region 4 included the rest of the tank fluid outside of the inlet jet region where the flow rate was equal to the inlet flow rate.

For the duration of time interval 1, the temperatures of Region 3 and Region 4 were assumed to be constant at the initial cold fluid temperature, T_c . Therefore, only the temporal temperatures of Region 1 and Region 2 needed to be determined in order to solve for the tank temperature profile for time interval 1.

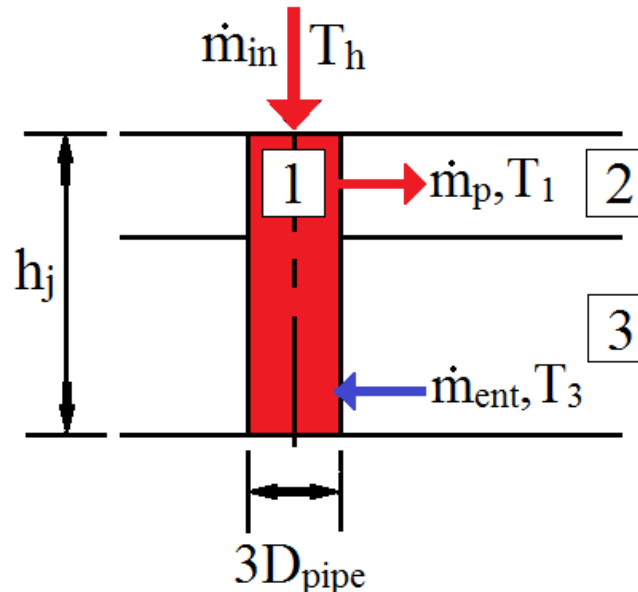


Figure 5.8 – Description of the energy inputs and outputs for temperature region 1, the inlet jet region.

The energy entering and leaving Region 1 is shown in Figure 5.8. Hot inlet fluid enters the top of the region at the inlet mass flow rate, \dot{m}_{in} . Cold fluid from Region 3 is entrained into the bottom of Region 1 at a flow rate of \dot{m}_{ent} . Finally, warm fluid that rises to the top of the tank leaves Region 1 at a flow rate equal to the sum of \dot{m}_{in} and \dot{m}_{ent} , which was indicated as \dot{m}_p (plume mass flow rate). The diameter of Region 1 was assumed to be approximately three times the diameter of the inlet pipe, which was approximated from simulations by Nizami et al. [17].

Using these energy flows, the energy equation given by Eq. (5.24) was solved to find the change in the temperature of Region 1, T_1 , with time for time interval 1. Eq. (5.25) was found by setting $T_3 = T_c$ and assuming that the volume of Region 1, V_1 , remained constant for the entire time interval. The volume would actually be increasing due to the behaviour of the inlet jet penetration depth. As the surrounding fluid temperature increases with time due to the constant addition of hot fluid, the buoyancy forces acting on the inlet jet would reduce, causing the jet to penetrate deeper. However, for the calculation of T_1 , the depth of Region 1 was assumed to be constant and equal to the initial jet penetration depth, which was calculated using Eq. (3.16). The initial temperature of Region 1 was set to T_c for the initial condition required to solve.

$$\rho C_p \frac{dV_1 T_1}{dt} = (\dot{m}_{in} C_p T_h + \dot{m}_{ent} C_p T_3) - \dot{m}_p C_p T_1 \quad (5.24)$$

$$T_1(t) = T_c + \frac{\dot{m}_{in}}{\dot{m}_p} (T_h - T_c) \left(1 - \exp \left(-\frac{\rho V_1}{\dot{m}_p} t \right) \right) \quad (5.25)$$

Since an expression for the temperature of Region 1 was determined (Eq. (5.25)), a solution for the temperature of Region 2 could be found since the temperature of the fluid entering is known. The energy flows for Region 2 are shown in Figure 5.9. Hot fluid from Region 1 enters along the inside surface. The depth of Region 2, C_o , was calculated as the location of the thermocline center. Therefore, the bottom boundary moves downwards at the mean flow velocity of the inlet jet region, which meant that no mass crossed the bottom boundary of Region 2.

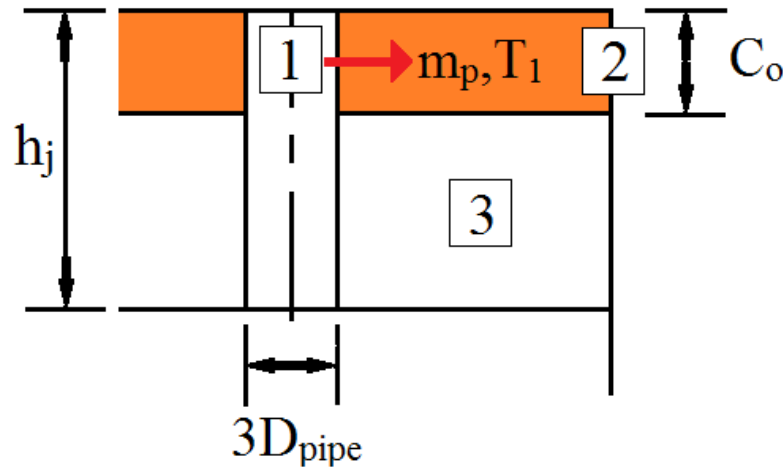


Figure 5.9 – Description of the energy inputs and outputs for temperature region 2, the inlet mixing hot region.

To determine the temperature of Region 2, T_2 , the axial flow rate was assumed to be constant for Regions 2 and 3, as mentioned above, and equal to the plume mass flow rate, \dot{m}_p , which is the sum of the inlet flow rate and the entrainment flow rate. Therefore, the bottom boundary of Region 2 moved at a constant velocity as the volume of Region 2 increases and the location of the thermocline center moves downwards. The location was determined by Eq. (5.26) where $C_{initial}$ represents the initial depth of Region 2, which was

set to a very small number. This was required to solve the proceeding differential equation without the division of zero at $t = 0$. Appendix E.2 discusses the choice of the value used for $C_{initial}$ for this model (0.00001 m). The quantity $A_{c,2}$ represents the cross-sectional area of Region 2.

$$C_o(t) = C_{initial} + \frac{\dot{m}_p}{\rho A_{c,2}} t \quad (5.26)$$

The magnitude of the inlet jet region flow rate was determined using the same correlation determined by Nizami et al. from parametric studies, as shown in Eq. (5.27). The inlet Richardson number was calculated using the initial tank inlet conditions.

$$\frac{\dot{m}_p}{\dot{m}_{in}} = 1.062 Ri^{-0.278} \quad (5.27)$$

The temperature of Region 2 was then determined using the differential equation given by Eq. (5.28). The initial temperature of Region 2 was set to T_c .

$$\rho C_p \frac{d}{dt} (V_2 T_2) = \dot{m}_p C_p T_1(t) \quad (5.28)$$

$$T_2(t) = \frac{\left(\dot{m}_p T_c t + \dot{m}_{in} (T_h - T_c) \left(t + \frac{\rho V_1}{\dot{m}_p} \exp\left(\frac{\dot{m}_p t}{\rho V_1}\right) \right) + Const \right)}{\dot{m}_p t + \rho A_2 C_{initial}} \quad (5.29)$$

$$Const = \rho A_2 C_{initial} T_c + \dot{m}_{in} (T_h - T_c) \frac{\rho V_1}{\dot{m}_p} \quad (5.30)$$

Figure 5.10 shows the description of Region 3. The temperature of Region 3 was assumed to remain constant for the duration of time interval 1 but the volume decreases

with time as Region 2 expands. Therefore, the top boundary of Region 3, moves downwards at a constant velocity while the bottom boundary also moves downwards, at a different rate, due to the increasing jet penetration depth with time. Fluid from Region 3 leaves the inside boundary, as fluid is entrained into the jet region (Region 1), and the bottom boundary, as fluid is sent to the rest of the tank (Region 4).

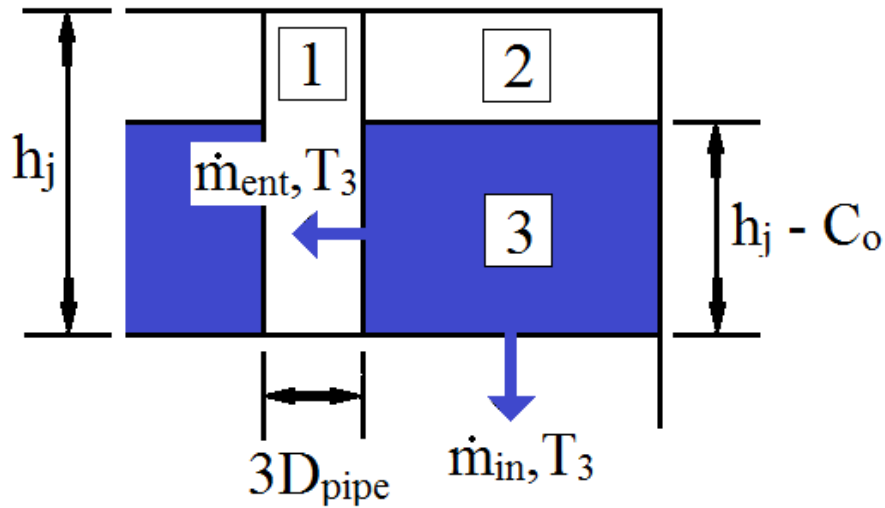


Figure 5.10 – Description of the energy inputs and outputs of region 3, the inlet mixing cold region.

With expressions for the temperatures of the regions in the inlet mixing region known, the jet penetration depth needed to be determined to solve for the duration of time interval 1, t_o . This was done using the correlation developed by Nizami et al., which depended on the inlet Richardson number, given by Eq. (5.31) where $T_I(t)$ represents the mean temperature within the inlet mixing region. This was determined by calculating the volume averaged temperature between Region 2 and Region 3 with time, as shown by Eq. (5.34). Therefore, for each time step, Eq. (5.31) and Eq. (5.34) were solved together, iteratively, to determine $T_I(t)$ and $h_j(t)$.

$$h_j(t) = a_{h_j} Ri(t)^{-b_{h_j}} = a_{h_j} \left(\frac{g\beta D_p (T_h - T_I(t))}{u_{in}^2} \right)^{-b_{h_j}} \quad (5.31)$$

$$a_{h_j} = -0.0150d^2 + 1.40d + 0.510 \quad (5.32)$$

$$b_{h_j} = 0.00535d + 0.448 \quad (5.33)$$

$$T_I(t) = \frac{C_o(t)T_2(t) + (h_j(t) - C_o(t))T_3}{h_j(t)} \quad (5.34)$$

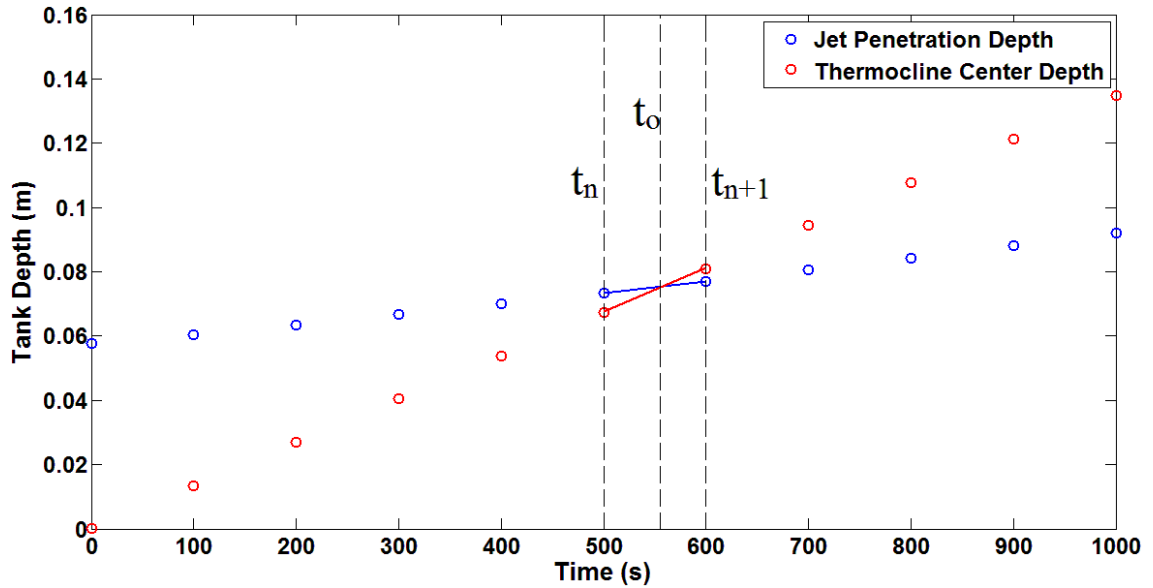


Figure 5.11 – Plots of the jet penetration depth and the thermocline center depth with time showing the intersection point when time interval 1 ends. The exact time is determined by assuming linear profiles between the two closest time steps values.

The end of time interval 1 would occur when the center of the thermocline reached the jet penetration depth, as described above. Since expressions for the jet penetration depth, h_j , and the thermocline location, C_o , with time were both known, the point of intersection was determined. Since the values of each variable were determined at specific

time intervals, this was done by first finding the time step at which the thermocline location first became larger than the penetration depth, t_{n+1} , as shown in Figure 5.11. Linear functions for each variable were then determined between the current and previous time steps to find the approximate time of the intersection, t_o .

The linear equations used to approximate the thermocline location and jet penetration depth between the two time steps were:

$$C_o(t) = C_o^n + (C_o^{n+1} - C_o^n) \frac{(t - t^n)}{(t^{n+1} - t^n)} \quad (5.35)$$

$$h_j(t) = h_j^n + (h_j^{n+1} - h_j^n) \frac{(t - t^n)}{(t^{n+1} - t^n)} \quad (5.36)$$

Therefore, the end of time interval 1 occurs when $C_o(t = t_o) = h_j(t = t_o)$.

$$t_o = t^n + \frac{(h_j^n - C_o^n)(t^{n+1} - t^n)}{(C_o^{n+1} - C_o^n) - (h_j^{n+1} - h_j^n)} \quad (5.37)$$

Having a definition for the time at which time interval 1 ended allowed for the characteristics of time interval 2 to be determined. As shown in Figure 5.7, the tank was divided into two constant temperature regions that were used to determine the change in the temperature profile as more hot fluid entered the tank. At the end of the first time interval, the temperature of the inlet mixing region may not be equal to the temperature of the inlet fluid. Therefore, changes in the temperature of the fluid above the thermocline for time interval 2 needed to be considered.

Region 5 consisted of the hot fluid above the thermocline center. As more fluid entered the tank, the bottom boundary of region 5 would move downwards at the mean fluid velocity. For time interval 2, the thermocline center is outside of the inlet mixing region. Therefore, the flow rate used to determine the velocity and location of the thermocline with time would be the inlet mass flow rate, \dot{m}_{in} . The thermocline location, C , is given by Eq. (5.38) where C_{o,t_o} is the thermocline center location at the end of time interval 1 (or the jet penetration depth when $t = t_o$) and A_c is the tank cross-sectional area.

$$C(t) = C_{o,t_o} + \frac{\dot{m}_{in}}{\rho A_c}(t - t_o) \quad (5.38)$$

To determine the temperature of Region 5, a similar approach to the calculation of Region 2 was implemented. Since the bottom boundary moves at the mean fluid velocity, no mass would cross the boundary. Therefore, the only energy transfer into Region 5 would be the hot inlet fluid at the top of the tank and the differential equation, Eq. (5.39), was solved to determine $T_5(t)$. The initial condition used to solve the differential equation would be the mean temperature of the inlet mixing region at the end of time interval 1 (or T_2 at $t = t_o$).

Initial Condition: $T_5(t = t_o) = T_l(t = t_o) = T_{l,t_o}$

$$\rho C_p \frac{dV_5 T_5}{dt} = \dot{m}_{in} C_p T_h \quad (5.39)$$

$$V_5(t) = A_c C(t) \quad (5.40)$$

$$T_5(t) = \frac{\frac{\dot{m}_{in} T_h}{\rho A_c} (t - t_o) + T_{I,t_o} C_{o,t_o}}{\frac{\dot{m}_{in}}{\rho A_c} (t - t_o) - C_{o,t_o}} \quad (5.41)$$

By determining analytical expressions for the temperatures of the tank regions, it was possible to solve for the overall temperature profiles in the tank with time. For time interval 1, the temperature profile was calculated using the same method as described in section 4.2.2 for heat losses to the surroundings. The temperature of Region 2 was used as the hot region temperature for the analytical solution, which would increase with time during charging. Therefore, the method of equating the thermocline thicknesses for each time step with different temperature parameters was used. For time interval 2, the same process was used, but now the hot region temperature for the thermocline was the temperature of Region 5. The MATLAB code used to simulate this analytical model is shown in Appendix D.5.

To validate this analytical model, experimental data was taken from Oliveski et al. [18] and Leohrke and Holzer [20] to analyze the accuracy using two different cases. The parameters for the two cases are shown in Table 5.3. The case studied by Oliveski et al. involved a low inlet Reynolds number and the case studied by Leohrke and Holzer had a high inlet Reynolds number. The inlet pipe for the high Reynolds number case was submerged by 50.8 mm. Therefore, the results obtained from the inlet jet mixing model were shifted downwards by the same amount. Both simulations were performed with the use of 100 tank nodes and 25 second time steps.

Table 5.3 – Low and high Reynolds number case conditions used by Oliveski et al. [18] and Leohrke and Holzer [20] for the experiments that were used to compare with the inlet mixing analytical model.

	Low Re Case (Oliveski et al.) Re = 1340	High Re Case (Leohrke and Holzer) Re = 8000
Inlet Temperature, $T_{in} (^{\circ}C)$	39.9	40.4
Initial Temperature, $T_{initial} (^{\circ}C)$	24.5	21.0
Inlet Flow Rate, \dot{m}_{in} (kg/s)	0.007655	0.090446
Tank Height, H (m)	0.57	2.032
Tank Diameter, D_T (m)	0.42	1.158
Inlet Pipe Diameter, D_P (m)	0.01	0.0254

The results for the low Reynolds number case are shown in Figure 5.12. Temperature vs. tank depth profiles were plotted at three different times; 10 minutes, 40 minutes, and 70 minutes. For this case, the time at the end of the first time interval, t_o , was predicted to be about 555 seconds. Therefore, the first temperature profile would represent the temperature profile just after the thermocline left the inlet mixing region. In addition to the experimental and model results, the temperature profiles given by the idealized analytical solution (i.e. the analytical solution based on the semi-infinite wall), which represent the temperature profiles that would be given by the TRNSYS one-dimensional models if there was no numerical error, and the results obtained from Nizami's quasi-1D model were plotted.

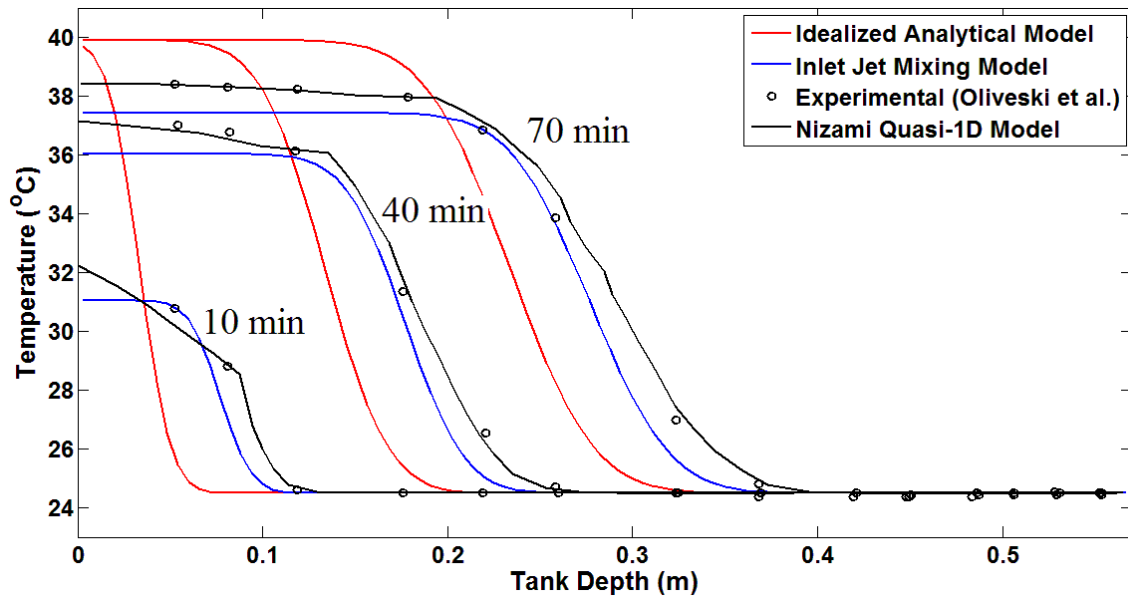


Figure 5.12 – Temperature vs tank depth results at 10 min, 40 min, and 70 min for the low Reynolds number ($Re=1340$) case. The inlet jet mixing model results were compared with the idealized analytical model, the experimental results obtained by Oliveski et al. [18], and the results from Nizami's quasi-1D model [17].

The idealized analytical solution did not provide the correct results because the temperature at the top of the tank was always equal to the inlet fluid temperature since it assumed a plug flow and could not replicate the effects of the inlet jet mixing at the top of the tank. However, the model for inlet jet mixing was able to calculate a rise in the temperature at the top of the tank with time due to the turbulent behaviour at the top of the tank. The location of the thermocline predicted by the idealized analytical solution was also incorrect. The temperature profiles were shown to occur higher in the tank for the same simulation times. This was because the idealized solution did not predict the additional velocity and mixing present within the inlet mixing region. The inlet jet mixing model did predict this as the location of the thermocline moved through the inlet mixing region at a higher rate during the first time interval.

While the inlet mixing model showed improvements over the idealized analytical model for determining the temperature profiles when a significant amount of inlet jet mixing was involved, the temperature predicted at the top of the tank was not correct for the entire simulation. The temperatures predicted by the model were lower than the experimental temperatures. This was the result of the method used to determine the hot region temperature for time interval 2. The volume of the region assumed to contain a constant hot temperature, Region 5, was too large, which led to the predicted temperatures being lower than they should have been. The results obtained from the model developed by Nizami et al. [17] showed better agreement with the experimental data since the model was able to predict the inlet jet behaviour with the use of a large number of nodes at the top of the tank.

The results obtained for the high Reynolds number case are shown in Figure 5.13. The temperature profiles were plotted at 15, 35, and 55 minutes. The duration of time interval 1 was calculated to be about 977 seconds, which was larger than the previous case. This made sense because with a higher Reynolds number, the jet would have more momentum and would penetrate deeper into the tank. Therefore, the thermocline would take a longer amount of time to progress through the inlet mixing region.

The comparison between the idealized analytical model and the inlet jet mixing model were similar to the previous case. The temperature at the top of the tank and the location of the thermocline were predicted with a higher accuracy with the inlet mixing model.

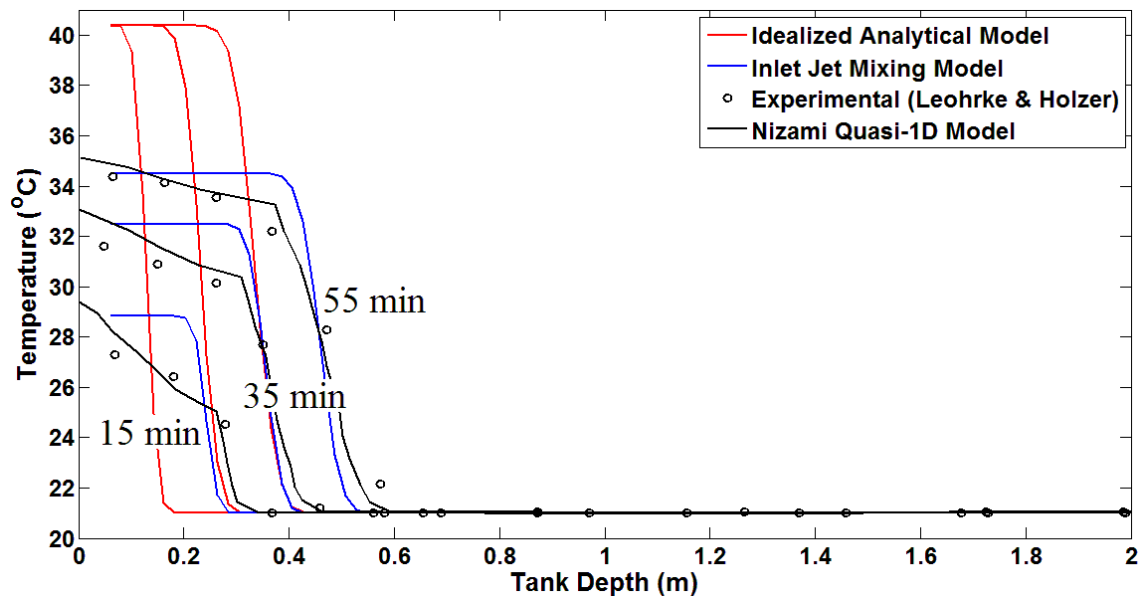


Figure 5.13 - Temperature vs tank depth results at 15 min, 35 min, and 55 min for the high Reynolds number ($Re=8000$) case conditions. The inlet jet mixing model results are compared with the idealized analytical model, the experimental results obtained by Leohrke and Holzer [20], and the results from Nizami's quasi-1D model [17].

The accuracy of the predicted temperatures at the top of the tank using the inlet mixing model was higher compared to the previous case. This was likely due to the increased amount of mixing caused by the inlet jet. Since more mixing would have occurred between the hot inlet fluid and the cold fluid initially in the actual tank, the temperature at the top of the tank would be lower and would take a longer period of time to increase. Also, since the inlet pipe was submerged in the tank for this case, there would have been a larger volume of cold fluid at the top of the tank, causing the temperature to be lower than if the pipe was not submerged. Therefore, since the model tends to under-predict the temperatures at the top of the tank, the predicted profiles matched better with the experimental data.

The experimental results also showed that there may have been more diffusion at the top of the tank since the temperature profiles showed a larger thermocline thickness

compared to the model results. Since there was a larger inlet Reynolds number, there would have been more mixing as entrainment occurred. Therefore, the effective diffusivity of the fluid within the inlet mixing region would have been larger. However, the inlet jet mixing model does not account for this additional diffusion. Nizami developed a correlation for the turbulent diffusivity created in the top region of the tank as a result of the inlet jet. When this correlation was included in Nizami's quasi-1D model, the results, which are also shown in Figure 5.13, gave a better approximation when compared with the experimental data. Therefore, to increase the accuracy of this inlet jet mixing model, this analysis could be implemented.

Finally, the inlet jet mixing model was used to simulate the conditions studied by Chu [12] since these results were what initially motivated this research. Figure 5.14 shows the temperature vs. time results at 5 different tank locations for the inlet jet mixing model, the experimental data collected by Chu, and the idealized analytical model developed in Section 5.1, which represent the results that the TRNSYS one-dimensional models would give if there was no numerical error.

The temperature profiles obtained from the inlet jet mixing model showed that the temperature of the fluid at the top of the tank increased at a slower rate, compared to the idealized analytical model, due to the predicted behaviour of the inlet jet mixing. This showed a better agreement with the experimental data. The thermocline locations predicted by the inlet jet mixing model also appear to be closer to the actual results because the assumption of a plug flow throughout the tank is not valid when the inlet jet causes a

significant amount of turbulent mixing at the top of the tank. Therefore, a more accurate solution was obtained with the use of the inlet jet mixing model

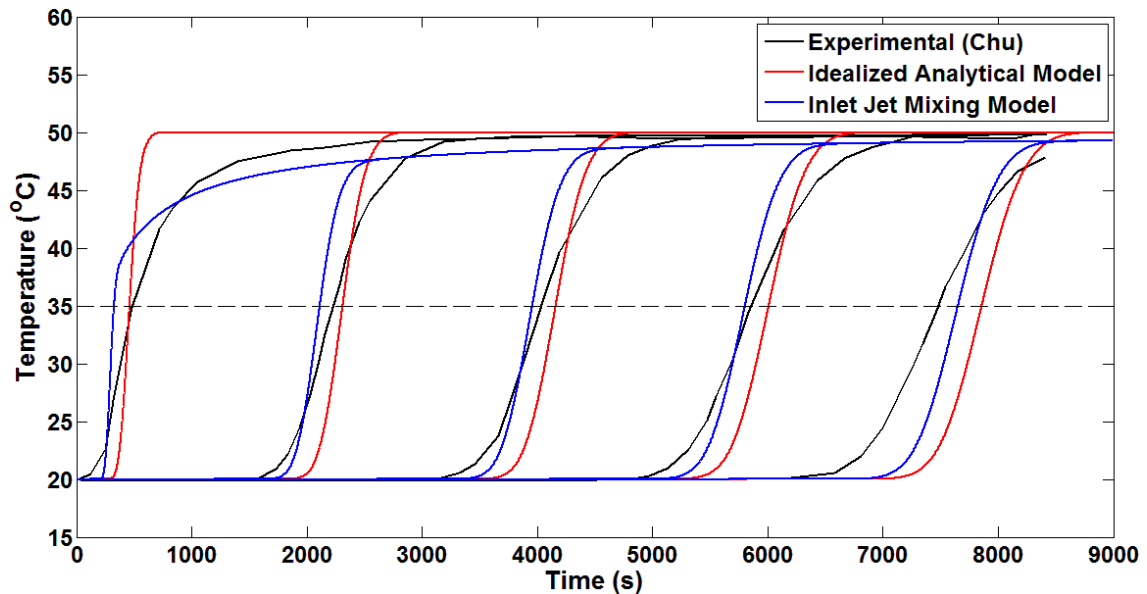


Figure 5.14 – Temperature vs time results at 5 different tank depths. The results of the inlet jet mixing model are compared with the idealized analytical model and the experimental results obtained by Chu [12].

5.3 Conclusions

This chapter outlined the development of new modelling strategies for thermal storage tanks. These models used analytical solution schemes which allowed for a higher accuracy for predicting the temperature profiles with time compared to the TRNSYS models. The one-dimensional, multi-node models used by TRNSYS were found to contain a large amount of numerical error since the simulations could not be run with a very large number of nodes without drastically increasing the computational effort. Therefore, the analytical approach used by these new modelling strategies allowed for a more accurate prediction of the temperature profiles. However, in order to determine if these models could

be used for the simulation of a solar thermal system over a long period of time, additional work should be done to assess the computational effort required.

The idealized analytical solution was developed based on the semi-infinite wall solution which was shown to give the results that would have been predicted by the TRNSYS multi-node models if there was no numerical error involved. However, the TRNSYS models were more robust as they were able to account for other mechanisms that lead to a loss of stratification, such as variable inlet temperatures, heat losses to the surroundings, and tank wall conduction.

Therefore, the analytical solution used was modified to account for each of these scenarios individually. The effects of an increasing inlet temperature were considered by calculating new thermoclines with each time step that the inlet temperature increased and adding them together using substitution. Heat losses to the surroundings were modelled by determining new temperatures for the hot and cold tank regions with time as heat left the tank. A similar approach was used to model the effects of tank wall conduction where the temperature of the hot region decreased as heat travelled into the wall and the cold region temperature increased as heat entered from the wall. The heat losses and tank wall conduction were only considered for a case with no tank flow since the change in the tank fluid temperature caused by these mechanisms was very small for the amount of time it would take to charge a typical storage tank.

Finally, an analytical solution was desired which included the effects of inlet jet mixing since this could lead to very different temperature profiles, especially at the top of

the tank. Therefore, the simulation was divided into two different time intervals which considered the initial growth of the thermocline within the inlet mixing region (time interval 1) and the rest of the tank which contained a uniform flow (time interval 2). This was done by assuming constant temperature regions within the tank. This analytical model was compared with experimental data from two different cases and it was found that the temperature profiles that were predicted gave more accurate results compared to the temperature profiles obtained with the idealized analytical solution.

Chapter 6

Conclusions and Future Work

Solar energy has shown to be an effective, sustainable resource that can be used as an alternative to natural gas or electrical resistance heating for space heating or hot water needs. Therefore, implementing solar thermal systems would help meet Canada's commitment to greenhouse gas reductions for the residential sector. These systems typically consist of solar collectors, thermal storage tanks, pumps, piping, and a hot water load.

Storage tanks are a necessity for solar thermal systems because there is a mismatch between the times at which solar energy is available and when higher heating loads are expected. Numerical modelling of these solar thermal systems is required in order to assess the performance over long periods of time. Therefore, simple and accurate models for predicting the temperatures within a thermal storage tank are desired to reduce the computational effort. Previous research, however, has shown that the storage tank models used for simulations with the TRNSYS simulation tool are not always able to accurately predict experimentally measured temperature profiles. This thesis focussed on the analysis of these TRNSYS storage tank models and the development of new modelling strategies which increased the accuracy of the temperature profile predictions while keeping the model simple enough such that they could be used in long term system simulations.

6.1 Performance of the TRNSYS One-Dimensional Multi-node Models

To test the performance of the TRNSYS one-dimensional multi-node models, two different cases were simulated that tested the basic functions of a thermal storage tank. The first case involved simple conduction within a stratified tank containing stationary fluid. This tested how well the models were able to predict the transient diffusion between the hot and cold temperature regions within the tank. The second case explored the ability of the models to predict plug flow charging of an initially cold tank. This allowed for assessment of the numerical treatment of advection. The simulation predictions were compared with analytical solutions based on the semi-infinite wall solution.

The results obtained for Case 1 revealed that the TRNSYS Type 534 and Type 60 models were able to accurately predict the temperature profiles with a maximum RMS error of about 1°C with the coarsest grid after 4 hours into the simulation. For varying time step sizes, the results were all very similar since the conduction occurred over a larger time scale than the time step sizes tested. It was also observed that the Type 4 model did not give accurate results because it did not consider conduction between the nodes. Therefore, the temperature profile from this model did not deviate from the initial condition.

The results of Case 2 showed a significant amount of numerical error when fluid flow was introduced. The numerical error was in the form of a false, numerical diffusion and resulted in a smeared thermocline profile. Although the RMS error reduces with the grid spacing, it was found that even with the finest grid spacing available (corresponding

to the maximum number of nodes allowed by TRNSYS), the RMS error was about 2.2°C after 1 hour into the simulation, which represents a significant amount of error. Similar results were obtained when the time step size was varied. With larger time steps, more error occurred, with RMS errors around 7°C . However, the solutions converged when a time step size of one second was used.

Additional simulations of Case 2 using an in-house one-dimensional code, which provided similar results compared with the TRNSYS models, revealed that the idealized analytical temperature profiles were obtainable with the one-dimensional models. However, it would have required about 10 times more nodes than what was allowed by TRNSYS to significantly reduce the numerical error. This would not be feasible for long term system simulations since it would require much more computational effort.

Finally, a Taylor series expansion was performed on the discretized energy equation used to solve the TRNSYS one-dimensional models to determine an expression for the numerical error. This revealed that the numerical scheme was first order accurate with spatial resolution and that the error appeared as an additional diffusion term. To test the conclusions from the Taylor series analysis, the numerical diffusion term was included in the analytical solution and compared with the results of the one-dimensional models. Excellent agreement between the numerical results and the analytical results was obtained. This analysis showed that the existing TRNSYS models suffer from numerical error and that the grid resolution required to reduce false diffusion would result in computational times that are incompatible with system simulations. As such, there is a need for improved modelling techniques.

6.2 Development of New Analytical Modelling Techniques

There are a number of physical mechanisms that can act to generate mixing within a storage tank and are not all inherently captured in the simple one-dimensional transient convection-diffusion equation which is solved in TRNSYS. The mixing mechanisms arise from the inlet jet entrainment, variations in the buoyancy force due to the time-varying nature of the collector outlet temperature, heat conduction through the tank walls, and heat losses from the tank itself. This thesis also explored methods to account for these effects while attempting to maintain the simplicity of the one-dimensional or quasi-one-dimensional framework.

The effects of an increasing inlet temperature were modelled by assuming a new thermocline would be created at the top of the tank after each time step where an increase in the inlet temperature was experienced. The concept of superposition of the analytical solutions was applied to develop the transient temperature profile in the tank. The method was assessed by comparing to a fine grid, one-dimensional numerical solution where good agreement was obtained.

Heat losses to the surroundings and heat conduction through the tank wall were only considered when there was no flow in the tank, for example, during overnight periods where the collector is not running and there is no load. During periods of charging or discharging, these heat transfer mechanisms have little impact in comparison to heat transfer by advection. Heat losses to the surroundings were modelled by determining new temperatures analytically for the hot and cold tank regions for each time step as a result of

the heat losses. The new profiles obtained as a result of the changing region temperatures were modelled by setting the thermocline thicknesses for the solutions of two consecutive time steps equal to each other. A similar approach, based on a fin analogy, was used to model the effects of tank wall conduction since the behaviour is similar. The temperature of the hot region decreases due to the heat sent to the wall, and the cold region temperature increases due to the heat delivered from the wall.

The last effect that was considered was the mixing caused by the inlet jet and was motivated by the work of Nizami et al. [17]. The solution was divided into two different time intervals. The first time interval occurred at the beginning of the simulation while the thermocline was located within the inlet mixing region. The fluid at the top of the tank moves at a different velocity than the rest of the tank due to the entrainment caused by the jet. Therefore, the thermocline development differed depending on where it was located within the tank. Time interval 1 ended when the center of the thermocline intersected with the inlet jet penetration depth, which increased as the surrounding fluid temperature increased. The thermocline profile during the second time interval was then determined while the hot region temperature increased as more hot fluid entered the top of the tank. This analytical model was compared with two different experimental cases to validate the results. It was found that the location of the thermocline with time agreed with the experimental results but the predicted temperature of the fluid at the top of the tank was slightly lower.

6.3 Recommendations for Future Work

The analysis of the TRNSYS one-dimensional models has shown that the amount of diffusion that is shown in the temperature profiles can be incorrect due to the numerical errors present in the simulations. Investigating the effect this additional diffusion has on the performance on an entire solar thermal system would be important to ensure that the long-term performance predicted by simulations using TRNSYS are providing meaningful results.

Previously developed models, similar to the TRNSYS storage tank models, could also be explored to test if they provide more accurate temperature profile predictions for different cases. The use of an adaptive-grid model, as suggested by Powell and Edgar [39], would allocate a larger number of nodes to the thermocline region and reduce the numerical error while keeping the computational effort to a minimum. Higher order schemes could also be implemented in the existing one-dimensional storage tank models for the approximation of the nodal temperatures. This would reduce the amount of numerical error predicted by the models.

The analytical modelling strategies developed in this research have shown better accuracy when modelling each individual mixing mechanism that they were designed for. However, all of these mechanisms can occur simultaneously in an actual tank. Therefore, it would be advantageous to develop a method of integrating these modelling strategies into a single tank model. For example, while hot fluid is being stored in a tank for a long period of time with no fluid flow, the models for heat losses to the surroundings and tank wall heat

conduction would both be used to predict the temperature profile. During tank charging, the inlet mixing model and the increasing inlet temperature model would both be used to simulate a realistic scenario.

The methods used to model the inlet jet mixing in a storage tank could also be improved. When compared with experimental results, it was shown that the accuracy of the predicted temperatures at the top of the tank, where a lot of mixing occurs, varied depending on the case. For the low Reynolds number case, the predicted temperatures were lower than the experimental and for the high Reynolds number case, the temperatures were much closer. Therefore, a better assumption could be made for predicting how the temperature increases during charging. It has also been shown by previous researchers that the amount of diffusion experienced in the turbulent mixing zone is larger. Therefore, a method to implement additional diffusion when the thermocline is located in the inlet mixing region would also increase the accuracy of the model.

It was also discussed how the effects of a decreasing inlet temperature were not possible with the developed analytical model. This was because the model does not consider the buoyancy of the cooler fluid entering the top of the tank and it would not predict the sinking that would occur. Therefore, this model should be expanded such that it can account for plume entrainment. The TRNSYS one-dimensional models consider this by implementing a mixing algorithm which mixes the fluid temperatures of two nodes when the temperature of the fluid in the upper node is lower.

Finally, it would be advantageous to explore the computational effort for these analytical modelling techniques compared to the TRNSYS storage tank models. The error function that is used to predict the temperature profile at each time step can be computationally expensive. There are also methods that have been developed to approximate the error function with simpler equations ([44], [45]) and could be implemented in the analytical models to reduce the computational effort.

References

- [1] Minister of Natural Resources, "Energy Efficiency Trends in Canada - 1990 to 2013," Natural Resources Canada, Ottawa, ON, 2016.
- [2] Natural Resources Canada, "About Renewable Energy," 2016. [Online]. Available: <http://www.nrcan.gc.ca/energy/renewable-electricity/7295#solar>.
- [3] B. Sibbitt, D. McClenahan, R. Djebbar, J. Thornton, B. Wong, J. Carriere and J. Kokko, "The performance of a high solar fraction seasonal storage district heating system - five years of operation," *Energy Procedia*, vol. 30, pp. 856-865, 2012.
- [4] "TRNSYS: Transient System Simulaton Tool," 2017. [Online]. Available: <http://http://www.trnsys.com/>.
- [5] J. J. Mutch, "Residential water heating: fuel conservation, economics, and public policy," Rand Corporation, Santa Monica, CA, 1974.
- [6] J. A. Duffie and W. A. Beckman, *Solar Engineering of Thermal Processes*, John Wiley & Sons, Inc., 2013, p. 54.
- [7] P. Mavros, V. Belessiotis and D. Haralambopoulos, "Stratified energy storage vessels: characterization of performance and modelling of mixing behavior," *Solar Energy*, vol. 52, no. 4, pp. 327-336, 1994.
- [8] C. A. Cruickshank, "Evaluation of a stratified multi-tank thermal storage for solar heating applications," *PhD Thesis, Queen's University*, 2009.
- [9] K. G. Hollands and M. F. Lightstone, "A review of low-flow, stratified-tank solar water heating systems," *Solar Energy*, vol. 43, no. 2, pp. 97-105, 1989.
- [10] M. Shaarawy, "Numerical Analysis of thermal stratification in large horizontal thermal energy storage tanks," *Master's Thesis, McMaster University*, 2014.
- [11] S. A. Klein, W. A. Beckman, J. W. Mitchell, J. A. Duffie, N. A. Duffie, T. L. Freeman, J. C. Mitchell, J. E. Braun, B. L. Evans, J. P. Kummer, R. E. Urban, A. Fiksel, J. W. Thornton, N. J. Blair, P. M. Williams, D. E. Bradley, T. P. McDowell, M. Kummert, D. A. Arias and M. J. Duffy, "Mathematial Reference. TRNSYS 17 User's Manual Volume 4," *Solar Energy Laboratory, University of Wisconsin-Madison*, 2010.

- [12] J. Chu, "Evaluation of a dual tank indirect solar-assisted heat pump system for a high performance house," *Master's Thesis, Carleton University*, 2014.
- [13] C. Baldwin and C. A. Cruickshank, "Using TRNSYS Types 4, 60 and 534 to model residential cold thermal storage using water and water/glycol solutions," in *IBPSA-Canada's eSim Conference*, Hamilton, 2016.
- [14] M. D. Wuestling, S. A. Klein and J. A. Duffie, "Promising control alternatives for solar water heating systems," *Journal of Solar Energy Engineering*, vol. 107, pp. 215-221, 1985.
- [15] H. Schlichting, *Boundary-Layer Theory* 7th Edition, McGraw-Hill, 1979.
- [16] A. Aviv, S. Morad, Y. Ratzon, G. Ziskind and R. Letan, "Experimental and numerical study of mixing in a horizontal hot-water storage tank," *Journal of Solar Energy Engineering*, vol. 131, 2009.
- [17] D. J. Nizami, M. F. Lightstone, S. J. Harrison and C. A. Cruickshank, "Negative buoyant plume model for solar domestic hot water tank systems incorporation a vertical inlet," *Solar Energy*, vol. 87, pp. 53-63, 2013.
- [18] R. D. C. Oliveski, A. Krenzinger and H. A. Vielmo, "Comparison between models for the simulation of hot water storage tanks," *Solar Energy*, vol. 75, pp. 121-134, 2003.
- [19] M. F. Lightstone, "A numerical study of thermal stratification in solar energy storage tanks," *Master's Thesis, University of Waterloo*, 1987.
- [20] R. I. Loehrke and J. C. Holzer, "Stratified thermal storage experiments. Technical Report HT-TS93," Prepared for the Boeing Computer Services Company, Seattle, Washington, 1979.
- [21] L. J. Shah and S. Furbo, "Entrance effects in solar storage tanks," *Solar Energy*, vol. 75, pp. 337-348, 2003.
- [22] Y. H. Zurigat, A. J. Ghajar and P. M. Moretti, "Stratified thermal storage tank inlet mixing characterization," *Applied Energy*, vol. 30, pp. 99-111, 1988.
- [23] J. D. Chung, S. H. Cho, C. S. Tae and H. Yoo, "The effect of diffuser configuration on thermal stratification in a rectangular storage tank," *Renewable Energy*, vol. 33, pp. 2236-2245, 2008.

- [24] G. F. Csordas, A. P. Brunger, K. G. T. Hollands and M. F. Lightstone, "Plume entrainment effects in solar domestic hot water systems employing variable-flow-rate control strategies," *Solar Energy*, vol. 49, no. 6, pp. 497-505, 1992.
- [25] L. J. Shah, E. Andersen and S. Furbo, "Theoretical and experimental investigations of inlet stratifiers for solar storage tanks," *Applied Thermal Engineering*, vol. 25, pp. 2086-2099, 2005.
- [26] E. Andersen, S. Furbo and J. Fan, "Multilayer fabric stratification pipes for solar tanks," *Solar Energy*, vol. 81, pp. 1219-1226, 2007.
- [27] Y. Jaluria and S. K. Gupta, "Decay of thermal stratification in a water body for solar energy storage," *Solar Energy*, vol. 28, no. 2, pp. 137-143, 1982.
- [28] Z. Lavan and J. Thompson, "Experimental study of thermally stratified hot water storage tanks," *Solar Energy*, vol. 19, pp. 519-524, 1977.
- [29] Y. A. Cengel and A. J. Ghajar, *Heat and Mass Transfer: Fundamentals and Applications*, 4th Edition, McGraw-Hill, 2010.
- [30] M. A. Abdoly and D. Rapp, "Theoretical and experimental studies of stratified thermocline storage of hot water," *Energy Convers. Mgmt*, vol. 22, pp. 275-285, 1982.
- [31] J. C. Holzer, H. N. Gari, R. I. Loehrke and M. K. Sharp, "Stratification enhancement in liquid thermal storage tanks," *Journal of Energy*, vol. 3, no. 3, pp. 129-130, 1979.
- [32] Y. H. Zurigat, P. R. Liche and A. J. Ghajar, "Influence of inlet geometry on mixing in thermocline thermal energy storage," *International Journal of Heat and Mass Transfer*, vol. 34, no. 1, pp. 115-125, 1991.
- [33] B. J. Newton, "Modelling of solar storage tanks," *Master's Thesis, University of Wisconsin-Madison*, 1995.
- [34] Y. Allard, M. Kummert, M. Bernier and A. Moreau, "Intermodel comparison and experimental validation of electrical water heater models in TRNSYS," in *Building Simulation 2011: 12th Conference of International Building Performance Simulation Association*, Sydney, 2011.
- [35] J. W. Thornton, D. E. Bradley, T. P. McDowell, N. J. Blair, M. J. Duffy, N. D. LaHam and A. V. Naik, "Storage Tank Library Mathematical Reference," *TESSLibs 17: Component Libraries for the TRNSYS Simulation Environment*, vol. 11, 2014.

- [36] L. Pantzlauff and R. M. Lueptow, "Transient positively and negatively buoyant turbulent round jets," *Experimenta in Fluids*, vol. 27, pp. 117-125, 1999.
- [37] J. S. Turner, "Jets and plumes with negative or reversing buoyancy," *Journal of Fluid Mechanics*, vol. 26, no. 4, pp. 779-792, 1966.
- [38] P. D. Friedman and J. Katz, "Rise height for negatively buoyant fountains and depth of penetration for negatively buoyant jets impinging an intergace," *Journal of Fluids Engineering*, vol. 122, pp. 779-782, 2000.
- [39] K. Powell and T. F. Edgar, "An adaptive-grid model for dynamic simulation of thermocline thermal energy storage systems," *Energy Conversion and Management*, vol. 76, pp. 865-873, 2013.
- [40] E. M. Kleinbach, W. A. Beckman and S. A. Klein, "Performance study of one-dimensional models for stratified thermal storage tanks," *Solar Energy*, vol. 50, no. 2, pp. 155-166, 1993.
- [41] A. Musser and W. Bahnfleth, "Evolution of temperature distributions in a full scale stratified chilled water storage tank," in *ASHRAE Transactions 104(1)*, 1998.
- [42] E. Garcia-Mari, M. Gasque, R. P. Gutierrez-Colomer, F. Ibanez and P. Gonzalez-Altozano, "A new inlet device that enhances thermal stratification during charging in hot water storage tank," *Applied Thermal Engineering*, vol. 61, pp. 663-669, 2013.
- [43] P. J. Pritchard, Fox and McDonald's Introduction to Fluid Mechanics, 8th Edition, John Wiley & Sons Inc., 2011.
- [44] H. T. Karlsson and I. Bjerle, "A simple approximation of the error function," *Computers and Chemical Engineering*, vol. 4, pp. 67-68, 1979.
- [45] I. W. Burr, "A useful approximation to the normal distribution function, with application to simulation," *Technometrics*, vol. 9, no. 4, pp. 648-651, 1967.

Appendix A

Semi-Infinite Wall Solution Comparison for Storage Tank Conduction

The analytical model used to predict the temperature profile within a storage tank was based on the semi-infinite wall solution since it predicts the conduction of heat that occurs in a wall that is introduced to a constant temperature boundary. This is similar to the behaviour of the fluid within a thermal storage tank because at the center of a thermocline, the temperature would be the average of the hot and cold region temperatures and remains constant, assuming no heat losses and a constant inlet temperature. Therefore, the semi-infinite wall solution should be able to predict the thermocline profile with time, as discussed in section 4.2.

To validate this assumptions, a simple case was considered which consisted of a storage tank with no flow that was initially perfectly stratified with hot fluid in the top half of the tank and cold fluid in the bottom half. The dimensions and initial conditions of the storage tank are shown in Figure A.1. The initial hot region temperature, T_h , was 50°C and the cold region temperature, T_c , was 20°C.

The temperature profiles obtained from the semi-infinite wall solution were compared with the in-house one-dimensional model described in section 3.4.1. The model used 100 equal volume nodes and 60 second time steps to ensure that there was grid and time step convergence. The results are shown in Figure A.2. The temperatures at different

tank heights were plotted after 6 hours and 12 hours. The profiles from the semi-infinite wall solution matched with the in-house model. Therefore, the semi-infinite wall solution was able to accurately predict the conduction that occurred between the hot and cold fluid regions within a storage tank when no flow was considered.

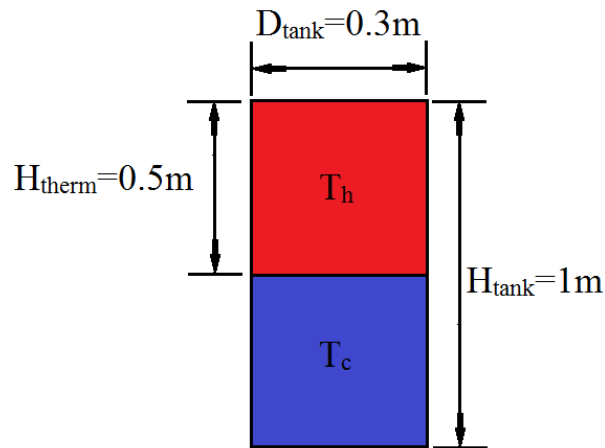


Figure A.1 – Initial conditions and dimensions of the storage tank used for simulations to compare the semi-infinite wall solutions with the in-house one-dimensional model.

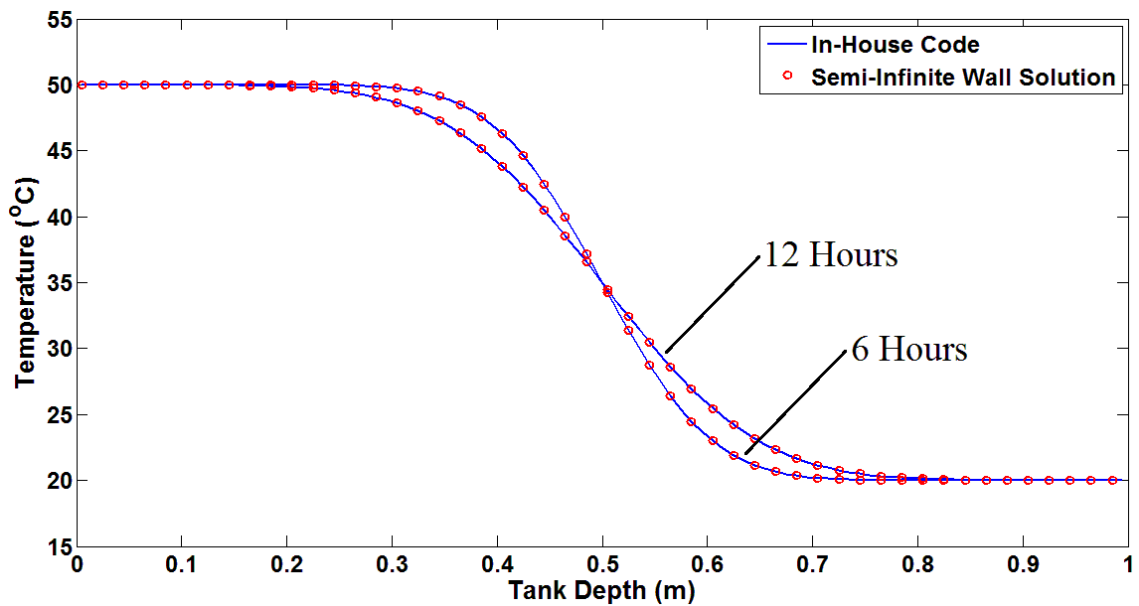


Figure A.2 – Temperature vs. tank depth results of the simulations using the semi-infinite wall solution and the in-house one-dimensional model after 6 and 12 hours.

By assuming a constant flow rate for the fluid within a storage tank, the semi-infinite wall solution can also be used to predict the temperature profile with time for a case with fluid flow. This was done by applying a Lagrangian framework which followed the thermocline. The location of the thermocline was found from integration of the one-dimensional plug flow velocity.

Appendix B

RMS Errors for TRNSYS Tank Model Case Studies

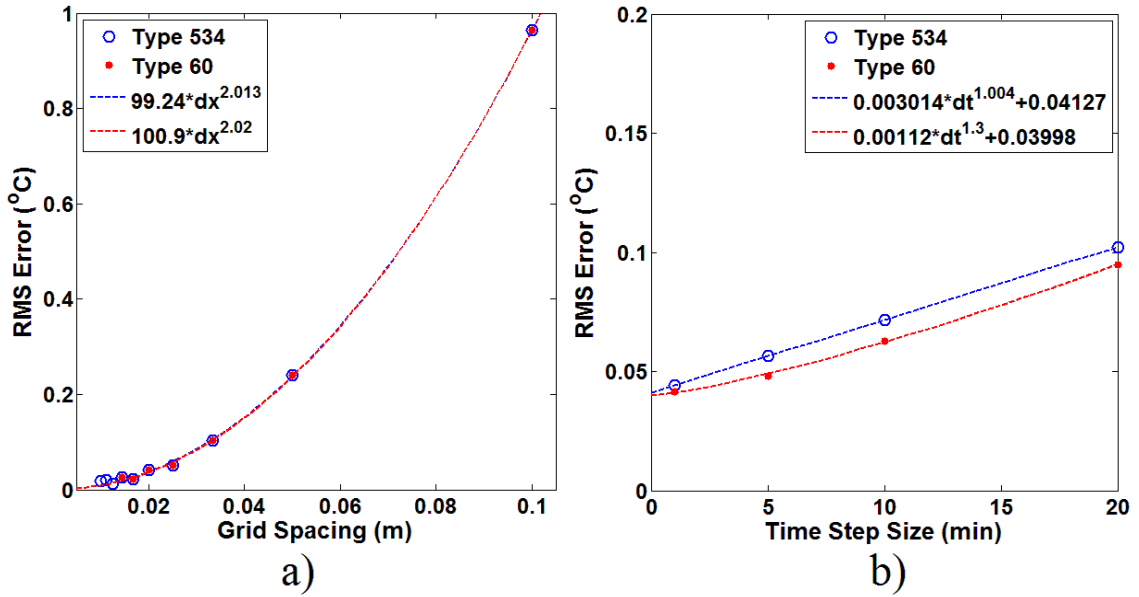
The RMS errors for the cases used to study the TRNSYS storage tank models in Chapter 4 were plotted to determine the average amount of error that was observed with the varying simulation parameters. The RMS values were calculated for the temperature profiles after 4 hours for Case 1 and after 1 hour for Case 2 using Eq. (B.1), where N is the number of tank nodes or the number of time steps used, $T_{i,simulated}$ is the simulated node temperature, and $T_{i,analytical}$ is the node temperature determined from the analytical model.

$$\text{Error}_{\text{RMS}} = \sqrt{\frac{\sum_{i=1}^N (T_{i,simulated} - T_{i,analytical})^2}{N}} \quad (\text{B.1})$$

The results for Case 1 and 2 are shown in Figure B.1. The grid spacing was varied between 0.01m and 0.1m, which corresponded to 100 and 10 nodes respectively. The time step sizes simulated were 1, 5, 10, and 20 minutes. Trend lines were also fit to the simulation data to obtain equations for the RMS error and determine the order of the errors for each case. The equations are shown in Table B.1.

Case 1, with only fluid conduction, showed small RMS errors since there was no fluid flow considered. Figure B.1a) shows the results with varying grid spacing. The maximum RMS error was about 0.96°C with the coarsest grid (with 10 nodes) for the Type 534 and Type 60 models. The trend plotted for these models showed an order of error of about 2.

Case 1



Case 2

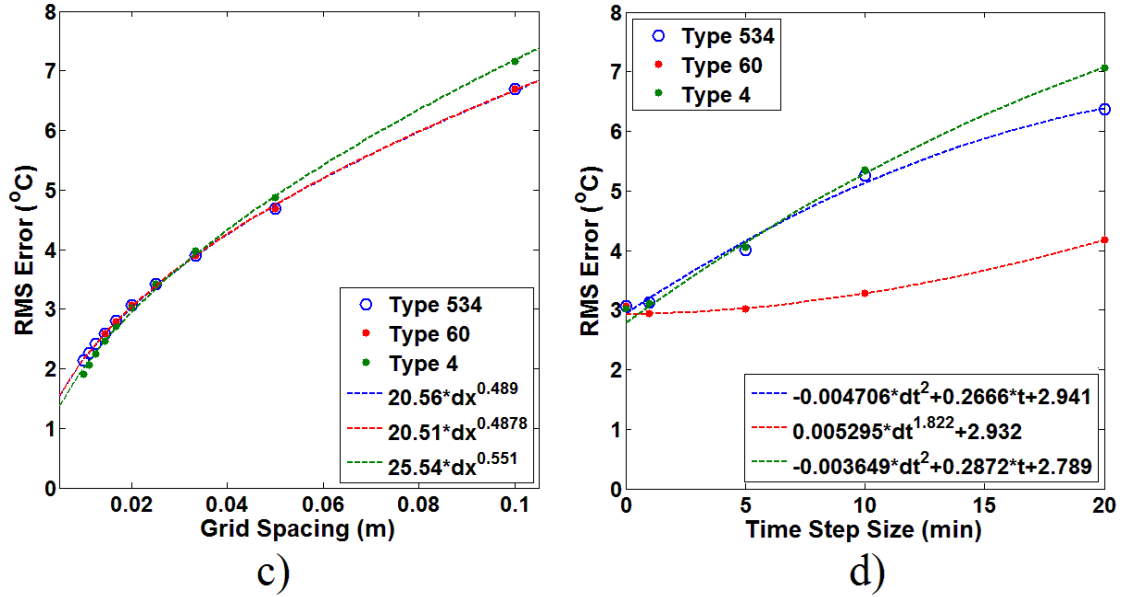


Figure B.1 – RMS temperature errors for a) Case 1 with varying grid spacing (after 4 hours), b) Case 1 with varying time step sizes (after 4 hours), c) Case 2 with varying grid spacing (after 1 hour), and d) Case 2 with varying time step sizes (after 1 hour).

Therefore the error for Case 1 can be reduced fairly quickly. By doubling the number of nodes, the error would be reduced by one quarter. The RMS error results for the Type 4 model were not shown for Case 1 because the model did not calculate conduction, and therefore produced a very large error since the initial profile did not change during the simulation.

Table B.1 – Equations of the trend-lines that fit the RMS error data for each of the TRNSYS models tested in Case 1 and Case 2.

Case	RMS Error Trend-line Equation
(a) Case 1, Grid Spacing	
Type 534	$99.24\Delta x^{2.013}$
Type 60	$100.9\Delta x^{2.02}$
(b) Case 1, Time Step Size	
Type 534	$0.003014\Delta t^{1.004} + 0.04127$
Type 60	$0.00112\Delta t^{1.3} + 0.03998$
(c) Case 2, Grid Spacing	
Type 534	$20.56\Delta x^{0.489}$
Type 60	$20.51\Delta x^{0.4878}$
Type 4	$25.54\Delta x^{0.551}$
(d) Case 2, Time Step Size	
Type 534	$-0.004706\Delta t^2 + 0.2666\Delta t + 2.941$
Type 60	$0.005295\Delta t^{1.822} + 2.932$
Type 4	$-0.003649\Delta t^2 + 0.2872\Delta t + 2.789$

The errors calculated for Case 1 with varying time step sizes were much smaller, as shown in Figure B.1b). The error produced by the Type 534 model showed a linear trend as the RMS error increased at a constant rate when the time step size increased. The Type 60 model showed less error since smaller, internal time steps were used. The Type 60 model also showed a slightly larger order of error since the rate of increase of the error was lower with smaller time step sizes.

Case 2 showed larger RMS errors since advection was included. As the grid spacing was decreased, Figure B.1c), the models showed a decrease in the RMS error from a maximum of $6.7^{\circ}C$ with the coarsest grid, to about $2^{\circ}C$. However, the minimum error was still significant, causing inaccurate temperature predictions. All three models showed an order of error of about 0.5. Therefore, as the grid spacing is decreased, the rate of reduction in the amount of error decreases. This means that a very large number of nodes would be required to obtain the exact analytical solution.

Finally, for varying time step sizes, the RMS error increased from $3^{\circ}C$ to $6.4^{\circ}C$ for the Type 534 and Type 4 models. The Type 60 model showed smaller RMS errors for larger time steps due to the use of internal time steps. All of the models still showed significant errors with smaller time step sizes because the simulations all used 50 nodes. Therefore, the predicted temperature profiles contained the error from the use of only 50 nodes and the error from the time step size selection. The Type 534 and Type 4 models showed an order of error of about 2. The error increased at a smaller rate as the time step size continued to increase. The Type 60 model also showed an order of error of 2, however, the rate of increase in the error increased as the time step size became larger.

Appendix C

Taylor Series Expansion of Energy Equation

This section outlines the steps used to obtain an expression for the numerical error that occurs with the Crank-Nicolson scheme (used in the TRNSYS Type 60 model). This was done by performing a Taylor series expansion on each of the terms of the discretized energy equation.

C.1 Converting Time Derivatives to Spatial Derivatives

To analyze the numerical error found from the Taylor series expansion of the energy equation, the resulting derivatives need to be written as only spatial derivatives or only time derivatives. For this research, everything was converted to spatial derivatives using the original energy equation where the unsteady term (time derivative of temperature) is equal to the sum of spatial derivatives for diffusion and convection, as shown in Eq. (C.1) where the subscripts represent the order of the derivatives.

$$T_t = \alpha T_{xx} - uT_x \quad (C.1)$$

Higher order time derivatives and mixed derivatives can also be converted using the same process:

$$T_{tt} = \frac{\partial}{\partial t} \left(\frac{\partial T}{\partial t} \right) = \frac{\partial}{\partial t} \left(\alpha \frac{\partial^2 T}{\partial x^2} - u \frac{\partial T}{\partial x} \right) \quad (C.2)$$

$$T_{tt} = \alpha \frac{\partial^2}{\partial x^2} \left(\frac{\partial T}{\partial t} \right) - u \frac{\partial}{\partial x} \left(\frac{\partial T}{\partial t} \right) \quad (C.3)$$

$$T_{tt} = \alpha \frac{\partial^2}{\partial x^2} \left(\alpha \frac{\partial^2 T}{\partial x^2} - u \frac{\partial T}{\partial x} \right) - u \frac{\partial}{\partial x} \left(\alpha \frac{\partial^2 T}{\partial x^2} - u \frac{\partial T}{\partial x} \right) \quad (C.4)$$

$$T_{tt} = \alpha^2 T_{x^4} - 2\alpha u T_{x^3} + u^2 T_{xx} \quad (C.5)$$

C.2 Taylor Series Expansions for Each Term

The following will show the process used for each term to obtain the numerical error.

(1) Unsteady Term

$$\frac{\partial T}{\partial t} = T_t = \frac{T_i^{k+1} - T_i^k}{\Delta t} \quad (C.6)$$

Taylor series expansion for the current time step, k:

$$T_t = \frac{1}{\Delta t} \left(\left(T_i^k + \Delta t [T_t]_i^k + \frac{\Delta t^2}{2} [T_{tt}]_i^k + \frac{\Delta t^3}{6} [T_{t^3}]_i^k + \dots \right) - T_i^k \right) \quad (C.7)$$

$$T_t = [T_t]_i^k + \frac{\Delta t}{2} [T_{tt}]_i^k + \frac{\Delta t^2}{6} [T_{t^3}]_i^k + \dots \quad (C.8)$$

Convert time derivatives to spatial derivatives using (C.1) - (C.5):

$$\begin{aligned} T_t = [T_t]_i^k + \frac{\Delta t}{2} & \left(\alpha^2 [T_{x^4}]_i^k - 2\alpha u [T_{x^3}]_i^k + u^2 [T_{xx}]_i^k \right) \\ & + \frac{\Delta t^2}{6} \left(\alpha^3 [T_{x^6}]_i^k - 3\alpha^2 u [T_{x^5}]_i^k + 3\alpha u^2 [T_{x^4}]_i^k \right. \\ & \left. - u^3 [T_{x^3}]_i^k \right) \end{aligned} \quad (C.9)$$

$$T_t = [T_t]_i^k + E1_i^k \quad (C.10)$$

Where $E1_i^k$ is the numerical error from the unsteady term:

$$\begin{aligned}
E1_i^k = & \frac{u^2 \Delta t}{2} [T_{xx}]_i^k - \left(\alpha u \Delta t + \frac{u^3 \Delta t^2}{6} \right) [T_{x^3}]_i^k \\
& + \left(\frac{\alpha^2 \Delta t}{2} + \frac{\alpha u^2 \Delta t^2}{2} \right) [T_{x^4}]_i^k + \dots
\end{aligned} \tag{C.11}$$

(2) Diffusion Term

$$\alpha \frac{\partial^2 T}{\partial x^2} = \alpha T_{xx} = \frac{\alpha}{2\Delta x^2} (T_{i+1}^{k+1} - 2T_i^{k+1} + T_{i-1}^{k+1} + T_{i+1}^k - 2T_i^k + T_{i-1}^k) \tag{C.12}$$

Taylor series expansion for the current node, i:

$$\begin{aligned}
\alpha T_{xx} = & \frac{\alpha}{2\Delta x^2} \left(\left(T_i^{k+1} + \Delta x [T_x]_i^{k+1} + \frac{\Delta x^2}{2} [T_{xx}]_i^{k+1} + \frac{\Delta x^3}{6} [T_{x^3}]_i^{k+1} + \dots \right) \right. \\
& - 2T_i^{k+1} \\
& + \left(T_i^{k+1} - \Delta x [T_x]_i^{k+1} + \frac{\Delta x^2}{2} [T_{xx}]_i^{k+1} - \frac{\Delta x^3}{6} [T_{x^3}]_i^{k+1} + \dots \right) \\
& + \left(T_i^k + \Delta x [T_x]_i^k + \frac{\Delta x^2}{2} [T_{xx}]_i^k + \frac{\Delta x^3}{6} [T_{x^3}]_i^k + \dots \right) - 2T_i^k \\
& + \left(T_i^{k+1} - \Delta x [T_x]_i^{k+1} + \frac{\Delta x^2}{2} [T_{xx}]_i^{k+1} - \frac{\Delta x^3}{6} [T_{x^3}]_i^{k+1} \right. \\
& \left. \left. + \dots \right) \right) \tag{C.13}
\end{aligned}$$

$$\alpha T_{xx} = \frac{\alpha}{2} [T_{xx}]_i^{k+1} + \frac{\alpha \Delta x^2}{24} [T_{x^4}]_i^{k+1} + \frac{\alpha}{2} [T_{xx}]_i^k + \frac{\alpha \Delta x^2}{24} [T_{x^4}]_i^k + \dots \tag{C.14}$$

Taylor series expansion for the current time step, k:

$$\begin{aligned}
\alpha T_{xx} = & \alpha [T_{xx}]_i^k + \frac{\alpha \Delta x^2}{12} [T_{x^4}]_i^k \\
& + \frac{\alpha}{2} \left(\Delta t [T_{xxt}]_i^k + \frac{\Delta t^2}{2} [T_{xxtt}]_i^k + \frac{\Delta t^3}{6} [T_{xxt^3}]_i^k + \dots \right) \\
& + \frac{\alpha \Delta x^2}{24} \left(\Delta t [T_{x^4t}]_i^k + \frac{\Delta t^2}{2} [T_{x^4tt}]_i^k + \frac{\Delta t^3}{6} [T_{x^4t^3}]_i^k + \dots \right)
\end{aligned} \tag{C.15}$$

Convert time derivatives to spatial derivatives:

$$\alpha T_{xx} = \alpha [T_{xx}]_i^k + E2_i^k \tag{C.16}$$

Where $E2_i^k$ is the numerical error from the diffusion term:

$$E2_i^k = -\left(\frac{\alpha u \Delta t}{2}\right) [T_{x^3}]_i^k + \left(\frac{\alpha \Delta x^2}{12} + \frac{\alpha^2 \Delta t}{2} + \frac{\alpha u^2 \Delta t^2}{2}\right) [T_{x^4}]_i^k + \dots \tag{C.17}$$

(3) Convection Term

$$u \frac{\partial T}{\partial x} = u T_x = \frac{u}{2\Delta x} (T_i^{k+1} - T_{i-1}^{k+1} + T_i^k - T_{i-1}^k) \tag{C.18}$$

Taylor series expansion for the current node, i:

$$\begin{aligned}
u T_x = & \frac{u}{2} \left([T_x]_i^{k+1} - \frac{\Delta x}{2} [T_{xx}]_i^{k+1} + \frac{\Delta x^2}{6} [T_{x^3}]_i^{k+1} + [T_x]_i^k \right. \\
& \left. - \frac{\Delta x}{2} [T_{xx}]_i^k + \frac{\Delta x^2}{6} [T_{x^3}]_i^k \right)
\end{aligned} \tag{C.19}$$

Taylor series expansion for the current time step, k:

$$\begin{aligned}
uT_x = & u[T_x]_i^k - \frac{u\Delta x}{2} [T_{xx}]_i^k + \frac{u\Delta x^2}{6} [T_{x^3}]_i^k \\
& + \frac{u}{2} \left(\Delta t [T_{xt}]_i^k + \frac{\Delta t^2}{2} [T_{xtt}]_i^k + \dots \right) \\
& - \frac{u\Delta x}{4} \left(\Delta t [T_{xxt}]_i^k + \frac{\Delta t^2}{2} [T_{xxtt}]_i^k + \dots \right) \\
& + \frac{u\Delta x^3}{12} \left(\Delta t [T_{x^3t}]_i^k + \frac{\Delta t^2}{2} [T_{x^3tt}]_i^k + \dots \right)
\end{aligned} \tag{C.20}$$

Convert time derivatives to spatial derivatives:

$$uT_x = u[T_x]_i^k + E3_i^k \tag{C.21}$$

Where $E2_i^k$ is the numerical error from the convection term:

$$\begin{aligned}
E3_i^k = & - \left(\frac{u\Delta x}{2} + \frac{u^2\Delta t}{2} \right) [T_{xx}]_i^k \\
& + \left(\frac{u\Delta x}{6} + \frac{\alpha u\Delta t}{2} + \frac{u^3\Delta t^2}{4} \right) [T_{x^3}]_i^k \\
& - \left(\frac{\alpha u^2\Delta t^2}{2} + \frac{\alpha u\Delta x\Delta t}{4} + \frac{u^3\Delta x^2\Delta t}{12} \right) [T_{x^4}]_i^k \\
& + \dots
\end{aligned} \tag{C.22}$$

C.3 Combining Discretized Terms

The discretized terms of the energy equation can now be combined to develop an expression for the overall numerical that is created with the use of the Crank-Nicolson scheme.

$$T_t - \alpha T_{xx} + u T_x = 0 \quad (C.23)$$

$$[T_t]_i^k - \alpha [T_{xx}]_i^k + u [T_x]_i^k + E1_i^k - E2_i^k + E3_i^k = 0 \quad (C.24)$$

Therefore, the total numerical error is:

$$E_i^k = E1_i^k - E2_i^k + E3_i^k \quad (C.25)$$

$$\begin{aligned} E_i^k = & -\left(\frac{u\Delta x}{2}\right) [T_{xx}]_i^k + \left(\frac{u\Delta x^2}{6} + \frac{u^3\Delta t^2}{12}\right) [T_{x^3}]_i^k \\ & - \left(\frac{\alpha\Delta x^2}{12} + \frac{\alpha u^2\Delta t^2}{2} + \frac{\alpha u\Delta x\Delta t}{4} + \frac{u^3\Delta x\Delta t^2}{8} \right. \\ & \left. + \frac{u^2\Delta x^2\Delta t}{12}\right) [T_{x^4}]_i^k + \dots \end{aligned} \quad (C.26)$$

Appendix D

MATLAB Code for the Analytical Models

The following sections outline the MATLAB scripts used in this thesis to simulate the case studies in Chapter 3 and the analytical modelling techniques developed in Chapter 4. The initial sections in the models was used for the model inputs, which were varied for the different cases.

D.1 Ideal Analytical Model Code

```
% -----
% -----
% Model Inputs
% -----
% -----

Th = 50; % Hot Temperature (C)
Tc = 20; % Cold Temperature (C)
Tave = (Th+Tc)/2; % Average Temperature (C)
mf = 0.01; % Mass Flow Rate (kg/s)

H = 1; % Tank Height (m)
Dtank = 0.3; % Tank Diameter (m)
Dpipe = 0.01; % Inlet Pipe Diameter (m)

visc = 0.00070057; % Average Fluid Viscosity (m2/s)
rhoH = 987.68; % Hot Water Density (kg/m3)
rhoC = 997.78; % Cold Water Density (kg/m3)
rho = 0.5*(rhoH + rhoC); % Average Fluid Density (kg/m3)
k = 0.62614; % Thermal Conductivity (W/mK)
cp = 4068.5; % Specific Heat Capacity (J/kgK)
beta = 0.00032452; % Thermal Expansion Coefficient
% (1/K)
alfa = k/(rho*cp); % Diffusivity (m2/s)
g = 9.81; % Gravitational Acceration
% (m/s2)
N = 100; % Number of Nodes
delt = 1; % Time Step Size (s)
tTotal = 7200; % Total Simulation Time (s)

NumDiff = 1; % Activate Numerical Diffusivity
% (0 = OFF, 1 = ON)
```

```

% -----
% -----
% Calculate Model Variables
% -----
% -----

Q = mf/rho; % Volumetric Flow Rate (L/min)
Ac = (pi/4)*(Dtank^2); % Tank Cross-section area (m2)
u = mf/(rho*(pi/4)*(Dtank^2)); % Mean Flow Velocity (m/s)
uIN = mf/(rhoH*(pi/4)*(Dpipe^2)); % Inlet Pipe Velocity (m/s)
x(1:N,1) = (H/(2*N)):(H/N):(H-H/(2*N)); % Node Locations

tEND = (tTotal/delt)+1; % Final Time Step Number
t(1:tEND,1) = 0:delt:tTotal; % Simulation time at each
% step(s)

if u == 0
    C(1:tEND,1) = H/2; % Location of thermocline (no
% fluid flow) (m)
else
    C = u*t; % Location of thermocline with
% time (w/ fluid flow) (m)
End

alfa = alfa + NumDiff*0.5*u*(H/N); % Additional Numerical
% Diffusivity Calculation (m2/s)

% -----
% -----
% Temperature Profile Calculation
% -----
% -----

for i = 1:tEND
    for j = 1:N
        if x(j,1) > C(i,1) % Below Thermocline

            T(i,j) = Tave + (Tc-Tave)*erf((x(j,1)-
C(i,1))/sqrt(4*alfa*t(i,1)));

            elseif x(j,1) < C(i,1) % Above Thermocline

                T(i,j) = (Tc + Th) - (Tave + (Tc-Tave)*erf((C(i,1)-
x(j,1))/sqrt(4*alfa*t(i,1))));

            end
        end
    end
end

```

D.2 Increasing Inlet Temperature Analytical Model Code

```

% -----
% -----
% Model Inputs
% -----
% -----

Tinitial = 20; % Initial Tank Fluid
               % Temperature (degC)

H = 1; % Tank Height (m)

visc = 0.00070057; % Average Fluid Viscosity
                  % (m2/s)
rhoH = 987.68; % Hot Water Density (kg/m3)
rhoC = 997.78; % Cold Water Density (kg/m3)
rho = 0.5*(rhoH + rhoC); % Average Fluid Density
                           % (kg/m3)
k = 0.62614; % Thermal Conductivity
              % (W/mK)
cp = 4068.5; % Specific Heat Capacity
              % (J/kgK)
beta = 0.00032452; % Thermal Expansion Coeff
                   % (1/K)
alfa = k/(rho*cp); % Diffusivity (m2/s)
g = 9.81; % Gravitational Acceration
           % (m/s2)
u = 0.0001; % Mean Tank Fluid Velocity
             % (m/s)
N = 100; % Number of Tank Nodes

% -----
% -----
% Read Input Temperature Data from Text File
% -----
% -----

load('InputTemp.txt') % Load input file

TIMEin = InputTemp(1:end,1); % Read Time Step Values (s)
Tin = InputTemp(1:end,2); % Read Inlet Temperature
                           % Values (degC)
Length = length(TIMEin); % Set Number of Time Steps
TinInitial = Tin(1,1); % Read Initial Inlet Temp.
                       % (degC)
ThermTime(1,1) = 0; % First Thermocline begins
                   % at t=0
ThermTemp(1,1) = TinInitial; % First Thermocline Hot
                              % Temperature (Initial Inlet
                              % Temp, degC)

```



```

% Determine times at which new thermocline is created (when temperature
% increases by 0.1 degC and the new hot temperature value for
% thermocline)
% -----

A = 0;
B = 1;
for i = 2:Length
    if abs(Tin(i,1) - Tin(B,1)) >= 0.01
        ThermTime((2+A),1) = TIMEin(i,1);
        TempIn((2+A),1) = Tin(i,1);
        A = A + 1;
        B = i;
    end
end

for i = 1:length(TempIn)
    if i == length(TempIn)
        ThermTemp(i,1) = TempIn(i,1);
    else
        ThermTemp(i,1) = 0.5*(TempIn(i,1) + TempIn(i+1,1));
    end
end

% -----
% -----
% Model Variable Calculations
% -----
% -----

% THERMOCLINE TEMPERATURES
% -----

Tave(1:length(ThermTime),1) = 0;
ThermInitial(1:length(ThermTime),1) = 0;
for i = 1:length(ThermTime)
    if i == 1
        Tave(i,1) = 0.5*(Tinitial + ThermTemp(i,1));
        ThermInitial(i,1) = Tinitial;
    else
        Tave(i,1) = 0.5*(ThermTemp(i-1,1) + ThermTemp(i,1));
        ThermInitial(i,1) = ThermTemp(i-1,1);
    end
end

% SIMULATION PARAMETERS
% -----

tEND = Length;                                % Final Time Step number
delt = TIMEin(2,1) - TIMEin(1,1);             % Time Step Size (s)

```

```

t = TIMEin; % Simulation times at each
              % time step (s)
x(1:N,1) = (H/(2*N)):(H/N):(H-H/(2*N)); % Node Locations (m)

% THERMOCLINE THICKNESS VARIABLES
% -----

C(1:tEND,1) = t.*u; % Initial Thermocline
                  % Location (m)

k = 0;
for i = 2:length(ThermTime)

    T(1:tEND,(1+k):(N+k)) = 0;
    k = k + N;

    for j = 1:tEND
        if t(j,1) <= ThermTime(i,1) % Determine when each
                                     % thermocline moves through
                                     % tank
            C(j,i) = 0;
        else
            C(j,i) = u*(t(j,1) - ThermTime(i,1));
        end
    end
end

% -----
% -----
% Thermocline Profile Calculation
% -----
% -----

m = 0;
for h = 1:length(ThermTime)
    for i = 1:tEND
        for j = 1:N
            if h == 1
                if x(j,1) > C(i,h)
                    T(i,j) = Tave(h,1) + (ThermInitial(h,1) -
Tave(h,1))*erf((x(j,1)-C(i,h))/sqrt(4*alfa*t(i,1)));
                elseif x(j,1) <= C(i,h)
                    T(i,j) = (ThermInitial(h,1)+ThermTemp(h,1)) -
(Tave(h,1) + (ThermInitial(h,1) - Tave(h,1))*erf((C(i,h)-
x(j,1))/sqrt(4*alfa*t(i,1))));
                end
            else
                if t(i,1) < ThermTime(h,1)
                    T(i,j+m) = ThermTemp(h-1,1);
                else
                    if x(j,1) > C(i,h)

```

```

        T(i,j+m) = Tave(h,1) + (ThermInitial(h,1) -
Tave(h,1))*erf((x(j,1)-C(i,h))/sqrt(4*alfa*(t(i,1)-ThermTime(h,1))));
        elseif x(j,1) <= C(i,h)
            T(i,j+m) = (ThermInitial(h,1)+ThermTemp(h,1)) -
(Tave(h,1) + (ThermInitial(h,1) - Tave(h,1))*erf((C(i,h)-
x(j,1))/sqrt(4*alfa*(t(i,1)-ThermTime(h,1))));
        end
    end
end
end
end
    m = m+N;
end

% -----
% -----
% Final Temperature Profile (Substitution)
% -----
% -----

Tfinal(1:tEND,1:N) = 0;
for i = 1:tEND
    for j = 1:N

        Tfinal(i,j) = T(i,j+N*(length(ThermTime)-1));

        for h = length(ThermTime):-1:2

            Tfinal(i,j) = Tfinal(i,j) + T(i,j+N*(h-2)) -
ThermInitial(h,1);

        end
    end
end
end

```

D.3 Heat Losses to the Surroundings Analytical Code Model

```

% -----
% -----
% Model Inputs
% -----
% -----

Th = 50; % Hot Temperature (C)
Tc = 20; % Cold Temperature (C)
Tave = (Th+Tc)/2; % Ave Temperature (C)
D = 0.3; % Tank Diameter (m)
H = 1; % Tank Height (m)
alfa = 0.0000001566; % Average Diffusivity (m2/s)

```

```

rho = 993.59; % Average Fluid Density
              % (kg/m3)
cp = 4068.5; % Average Specific Heat
             % Capacity (J/kgK)
mf = 0; % Mass Flow Rate (kg/s)

Tsurr = 10; % Surroundings Temperature
          % (C)
h = 0.34; % Convective Heat Transfer
          % Coeff (W/m2K)

N = 100; % Number of Nodes
delt = 300; % Time Step Size (s)
tTotal = 12*3600; % Total Simulation Time (s)
delx = H/N;

% -----
% -----
% Calculate Model Variables
% -----
% -----

x(1:N,1) = (H/(2*N)):(H/N):(H-H/(2*N)); % Node Centre Locations (m)
tEND = (tTotal/delt)+1; % Last Time Step Index
t(1:tEND,1) = 0:delt:tTotal; % Simulation time at each
                             % time step (s)
C(1:tEND,1) = H/2; % Stationary Thermocline
                  % Position (m)

% -----
% -----
% Calculate Temperature Profile with NO Heat Losses
% -----
% -----

for i = 1:tEND
    for j = 1:N
        if x(j,1) > C(i,1) % Below Thermocline

            T(i,j) = Tave + (Tc-Tave)*erf((x(j,1)-
C(i,1))/sqrt(4*alfa*t(i,1)));

        elseif x(j,1) < C(i,1) % Above Thermocline

            T(i,j) = (Tc + Th) - (Tave + (Tc-Tave)*erf((C(i,1)-
x(j,1))/sqrt(4*alfa*t(i,1))));

        elseif x(j,1) == C(i,1)

            T(i,j) = Tave;

```

```

        end
    end
end

% -----
% -----
% Calculate Temperature Profile With Heat Losses
% -----
% -----

% Determine Hot/Cold Region Temperatures with Time
% -----

Ttop(1,1) = Th; % Initial Hot Region
                % Temperature (degC)
Tbot(1,1) = Tc; % Initial Cold Region
                % Temperature (degC)

for i = 2:tEND

    Ttop(i,1) = Tsurr + (Th - Tsurr)*exp(-(4*h*t(i,1)/(rho*cp*D)));
    Tbot(i,1) = Tsurr + (Tc - Tsurr)*exp(-(4*h*t(i,1)/(rho*cp*D)));

end

% Determine Temperature Profile
% -----

TaveHL = 0.5*(Ttop + Tbot); % Average Temperature with
                             % Heat Losses (degC)
time(2,1) = delt;          % Time at first time step
                             % (s)

for i = 1:N
    if i <= (C(1,1)/H)*N % Setting Initial
                           % Temperature Profile
        Thl(1,i) = Th;
    else
        Thl(1,i) = Tc;
    end
end

for i = 2:tEND-1
    for j = 1:N

        if x(j,1) > C(i,1) % Below Thermocline

            Thl(i,j) = TaveHL(i,1) + (Tbot(i,1) -
TaveHL(i,1))*erf((x(j,1)-C(i,1))/sqrt(4*alfa*time(i,1)));

```

```

elseif x(j,1) < C(i,1) % Above Thermocline

    Thl(i,j) = (Tbot(i,1) + Ttop(i,1)) - (TaveHL(i,1)
+ (Tbot(i,1)-TaveHL(i,1))*erf((C(i,1)-x(j,1))/sqrt(4*alfa*time(i,1)))));

end
end

% Determine Thermocline Thickness at the end of the time step
% -----

Wth(i,1) = 2*sqrt(4*alfa*time(i,1))*erfinv(1 +
    0.001*(Tbot(i,1)/(Tbot(i,1) - TaveHL(i,1))));

% Determine Time for profile with temperatures of next time step
% to obtain the same thermocline thickness
% -----

tnew(i,1) = (1/(4*alfa))*(Wth(i,1)/(2*erfinv(1 +
0.001*(Tbot(i+1,1)/(Tbot(i+1,1)-TaveHL(i+1,1)))))^2;

% Calculate next 'fictitious' simulation time value
% -----

time(i+1,1) = tnew(i,1) + delt;
end

```

D.4 Wall Heat Conduction Analytical Model Code

```

% -----
% -----
% Model Inputs
% -----
% -----

Th = 50; % Hot Temperature (C)
Tc = 20; % Cold Temperature (C)
Tave = (Th+Tc)/2; % Ave Temperature (C)
D = 0.3; % Tank Diameter (m)
H = 1; % Tank Height (m)
alfa = 0.0000001566; % Average Diffusivity (m2/s)
rho = 993.59; % Average Fluid Density
% (kg/m3)
cp = 4068.5; % Average Specific Heat
% Capacity (J/kgK)
mf = 0; % Mass Flow Rate (kg/s)

hw = 100; % Convective Heat Transfer

```

```

% Coefficient between wall
% and fluid (W/m2K)
kw = 45; % Tank Wall Thermal
% Conductivity (W/mK)
a = 0.01; % Tank Wall Thickness

N = 100; % Number of Nodes
delt = 300; % Time Step Size (s)
tTotal = 12*3600; % Total Simulation Time (s)
delx = H/N;

% -----
% -----
% Calculate Model Variables
% -----
% -----

x(1:N,1) = (H/(2*N)):(H/N):(H-H/(2*N)); % Node Centre Locations
tEND = (tTotal/delt)+1; % Last Time Step Index
t(1:tEND,1) = 0:delt:tTotal; % Time Steps
C(1:tEND,1) = H/2; % Stationary Thermocline
% Position

% -----
% -----
% Calculate Temperature Profile for NO Wall Conduction
% -----
% -----

for i = 1:tEND
    for j = 1:N
        if x(j,1) > C(i,1) % Below Thermocline

            T(i,j) = Tave + (Tc-Tave)*erf((x(j,1)-
C(i,1))/sqrt(4*alfa*t(i,1)));

            elseif x(j,1) < C(i,1) % Above Thermocline

                T(i,j) = (Tc + Th) - (Tave + (Tc-Tave)*erf((C(i,1)-
x(j,1))/sqrt(4*alfa*t(i,1))));

            elseif x(j,1) == C(i,1)

                T(i,j) = Tave;

            end
        end
    end
end

% -----
% -----
% Calculate Temperature Profile with Wall Heat Conduction

```

```

% -----
% -----

% Determine Hot/Cold Region Temperatures with Time
% -----

P = pi*D; % Tank Wall Perimeter (m)
Do = D + a; % Wall Outer Diameter (m)
Acw = (pi/4)*(Do^2) - (D^2); % Cross-Sectional Area of
% Wall (m2)
Twall = 0.5*(Th + Tc); % Wall Temperature (degC)

Cwhc = 0.5*(sqrt(hw*P*kw*Acw))*tanh((H/2)*(sqrt((hw*P)/(kw*Acw))));
% Wall Heat Conduction
% Constant Term

Ttop(1,1) = Th; % Initial Hot Region
% Temperature (degC)
Tbot(1,1) = Tc; % Initial Cold Region
% Temperature (degC)

Vtop = (pi/4)*(D^2)*C(1,1);
Vbot = (pi/4)*(D^2)*(H-C(1,1));

for i = 2:tEND

    Ttop(i,1) = Twall + (Th - Twall)*exp(-(Cwhc*t(i,1)/(rho*cp*Vtop)));
    Tbot(i,1) = Twall + (Tc - Twall)*exp(-(Cwhc*t(i,1)/(rho*cp*Vbot)));

end

% Determine Final Temperature Profile
% -----

TaveWHC = 0.5*(Ttop + Tbot); % Average Thermocline
% Temperature (degC)
time(2,1) = deltt; % First Time Step (s)

for i = 1:N
    if i <= (C(1,1)/H)*N % Setting Initial
% Temperature Profile
        Twhc(1,i) = Th;
    else
        Twhc(1,i) = Tc;
    end
end

for i = 2:tEND-1
    for j = 1:N

```



```

        if x(j,1) > C(i,1)                                % Below Thermocline

            Twhc(i,j) = TaveWHC(i,1) + (Tbot(i,1) -
TaveWHC(i,1))*erf((x(j,1)-C(i,1))/sqrt(4*alfa*time(i,1)));

        elseif x(j,1) < C(i,1)                            % Above Thermocline

            Twhc(i,j) = (Tbot(i,1) + Ttop(i,1)) - (TaveWHC(i,1)
+(Tbot(i,1)-TaveWHC(i,1))*erf((C(i,1)-x(j,1))/sqrt(4*alfa*time(i,1))));

        end
    end

    % Determine Thermocline Thickness at the end of the time step
    % -----

    Wth(i,1) = 2*sqrt(4*alfa*time(i,1))*erfinv(1 +
0.001*(Tbot(i,1)/(Tbot(i,1) - TaveWHC(i,1))));

    % Determine Time for profile with temperatures of next time step
    % to obtain the same thermocline thickness
    % -----

    tnew(i,1) = (1/(4*alfa))*(Wth(i,1)/(2*erfinv(1 +
0.001*(Tbot(i+1,1)/(Tbot(i+1,1)-TaveWHC(i+1,1)))))^2;

    % Calculate next 'fictitious' simulation time value
    % -----

    time(i+1,1) = tnew(i,1) + delt;
end

```

D.5 Inlet Jet Mixing Analytical Model Code

```

% -----
% -----
% Model Inputs
% -----
% -----

Th = 50;                                % Hot Temperature (C)
Tc = 20;                                % Cold Temperature (C)
Tave = (Th+Tc)/2;                        % Average Temperature (C)
mf = 0.001;                             % Mass Flow Rate (kg/s)

H = 1;                                  % Tank Height (m)
Dtank = 0.3;                             % Tank Diameter (m)
Dpipe = 0.01;                            % Inlet Pipe Diameter (m)
visc = 0.00070057;                       % Average Fluid Viscosity
                                           % (m2/s)

```

```

rhoH = 987.68; % Hot Water Density (kg/m3)
rhoC = 997.78; % Cold Water Density (kg/m3)
rho = 0.5*(rhoH + rhoC); % Average Fluid Density
% (kg/m3)
k = 0.62614; % Thermal Conductivity
% (W/mK)
cp = 4068.5; % Specific Heat Capacity
% (J/kgK)
beta = 0.00032452; % Thermal Expansion Coeff.
% (1/K)
alfa = k/(rho*cp); % Diffusivity (m2/s)

N = 100; % Number of Nodes
delt = 1; % Time Step Size (s)
tTotal = 7200; % Total Simulation Time (s)
g = 9.81; % Gravitational Acceleration
% (m/s2)

% -----
% -----
% Calculate Model Variables
% -----
% -----

Q = mf/rho; % Volumetric Flow Rate
% (m3/s)
Ac = (pi/4)*(Dtank^2); % Tank Cross-section area
% (m2)
u = mf/(rho*(pi/4)*(Dtank^2)); % Mean Flow Velocity (m/s)
uIN = mf/(rhoH*(pi/4)*(Dpipe^2)); % Inlet Pipe Velocity (m/s)
x(1:N,1) = (H/(2*N)):(H/N):(H-H/(2*N)); % Node Locations

tEND = (tTotal/delt)+1; % Last Time Step Value
t(1:tEND,1) = 0:delt:tTotal; % Simulation time at each
% time step (s)

% -----
% -----
% Initial Jet Penetration Depth and Plume Velocity (from Nizami [12])
% -----
% -----

% NIZAMI CONSTANTS %
dpipe = Dpipe*1000; % Inlet Pipe
% Diameter (mm)
ahj = -0.0150*(dpipe^2) + 1.40*(dpipe) + 0.510; % Penetration Depth
% Parameter a
bhj = 0.00535*(dpipe) + 0.448; % Penetration Depth
% Parameter b

% MODELING CONSTANTS %
Rio = (g*beta*Dpipe*(Th-Tc))/(uIN^2); % Initial Richardson
% Number

```

```

hIo = (ahj/1000)*(Rio^(-bhj)); % Initial
                                   % Penetration Depth

% INLET PLUME VELOCITY (NIZAMI METHOD) %
mfp = mf*1.062*(Rio^(-0.278)); % Inlet Plume Mass
                                   % Flow Rate (kg/s)
up = mfp/(rho*(pi/4)*(Dtank^2)); % Inlet Plume
                                   % Velocity (m/s)

% -----
% -----
% Time Interval 1 (0<t<to)
% -----
% -----

% Determine TI and hj for 0<t<to:
% -----

A2 = (pi/4)*((Dtank^2) - ((3*Dpipe)^2)); % Cross-sectional Area of
                                   % Region 2 (m2)
V1 = (pi/4)*((3*Dpipe)^2)*hIo; % Volume of Region 1 (m3)
Ci = 0.00001; % Initial Thermocline
                                   % Location (m)
Taul = -rho*V1/mfp; % Time Constant for Region 1
CT2 = Tc*rho*A2*Ci + mf*(Th-Tc)*Taul; % Constant Term for Region 2

for i = 1:tEND
    T2Top(i,1) = mfp*Tc*t(i,1) + mf*(Th-Tc)*(t(i,1) -
    Taul*exp(t(i,1)/Taul)) + CT2;
    T2Bot(i,1) = mfp*t(i,1) + rho*A2*Ci;
    T2(i,1) = T2Top(i,1)/T2Bot(i,1); % Temperature of Region 2

    Co(i,1) = (mfp/(A2*rho))*t(i,1) + Ci; % Location of Thermocline

    if i == 1
        TIo(i,1) = Tave;
    else
        TIo(i,1) = TIo(i-1,100);
    end

    % Iterate to solve for the jet penetration depth, h, and inlet
    % mixing region temperature, TIo:

    for j = 1:100
        h(i,j)=(ahj/1000)*((g*beta*(Th-TIo(i,j))*Dpipe)/(uIN^2))^(-bhj);
        TIo(i,j+1) = (Co(i,1)*T2(i,1) + (h(i,j) - Co(i,1))*Tc)/(h(i,j));
    end

    Ri(i,1) = (g*beta*(Th-TIo(i,100))*Dpipe)/(uIN^2);
    hj(i,1) = h(i,100);

end

```

```

% Calculate end of time interval 1, to
% -----

for i = 2:tEND
    if hj(i,1) <= Co(i,1)                                % Determine when thermocline
                                                            % passes jet penetration
                                                            % depth
        n = i-1;
        break
    end
end

% Determine time at end of time interval 1, to:

to = t(n,1) + ((hj(n,1) - Co(n,1))*(t(n+1,1) - t(n,1)))/((Co(n+1,1) -
Co(n,1)) - (hj(n+1,1) - hj(n,1)));

TIto = TIo(n,100);                                       % Temperature at the end of
                                                            % time interval 1 (degC)
hto = hj(n,1);                                           % Jet Penetration Depth at
                                                            % end of time interval 1 (m)

% -----
% -----
% Time Interval 2 (t>to)
% -----
% -----

% Determine inlet mixing region temperature, TI, for t>to
% -----

CTIn = TIto*hto - (mf*Th*to)/(rho*Ac);
for i = 1:tEND
    TIn(i,1) = ((mf*Th*t(i,1))/(rho*Ac) + CTIn)/(u*(t(i,1) - to) + hto);
End

% Determine Overall TI
% -----

for i = 1:tEND
    if i <= n
        TI(i,1) = T2(i,1);
    else
        TI(i,1) = TIn(i,1);
    end
end

% Thermocline Location for t>to
% -----

for i = 1:tEND
    if t(i,1) <= to

```

```

        C(i,1) = up*t(i,1) + Ci;
    else
        C(i,1) = C(i-1,1) + u*delt;
    end
end

% -----
% -----
% Final Temperature Profile Calculation - Thermocline Thickness Method
% -----
% -----

TaveS = 0.5*(TI + Tc);
time(2,1) = delt;
Tth(1,1:N) = Tc;

for i = 2:tEND-1
    for j = 1:N
        if x(j,1) > C(i,1) % Below Thermocline

            Tth(i,j) = TaveS(i,1) + (Tc-TaveS(i,1))*erf((x(j,1)-
C(i,1))/sqrt(4*alfa*time(i,1)));

            elseif x(j,1) < C(i,1) % Above Thermocline

                Tth(i,j) = (Tc + TI(i,1)) - (TaveS(i,1) + (Tc-
TaveS(i,1))*erf((C(i,1)-x(j,1))/sqrt(4*alfa*time(i,1))));

            end
        end
    end

    % Determine Thermocline Thickness at the end of the time step
    % -----

    Wth(i,1) = 2*sqrt(4*alfa*time(i,1))*erfinv(1 + 0.001*(Tc/(Tc -
TaveS(i,1))));

    % Determine Time for profile with temperatures of next time step to
    % obtain the same thermocline thickness
    % -----

    tnew(i,1) = (1/(4*alfa))*(Wth(i,1)/(2*erfinv(1 + 0.001*(Tc/(Tc-
TaveS(i+1,1))))))^2;

    % Calculate next 'fictitious' simulation time value
    % -----

    time(i+1,1) = tnew(i,1) + delt;
end

```

Appendix E

Inlet Jet Mixing Model Validation

E.1 2D Axisymmetric Simulation Conditions

The simulation results for the low Reynolds number case, shown by Nizami et al. [17], provided information about the tank temperature profile and velocity fields after 10, 40, and 70 minutes. However, in order to more accurately predict the temperature profiles within the tank using the analytical modelling techniques, additional information was desired during the initial charging stage. Therefore, a 2D axisymmetric simulation was performed using the same parameters to obtain temperature contour results at times before 10 minutes.

E.1.1 Storage Tank Mesh

The mesh for the 2D axisymmetric storage tank was created using ICEM CFD 12.1. The basic shape of the tank, as shown in Figure E.1. The length of the inlet and outlet pipes were modelled as 0.3m to ensure that a fully developed flow was entering the tank. The dimensions for each section of the geometry are shown in Table E.1. The basic shape was then rotationally extruded by 5° to create the volume for one node in the rotational direction.

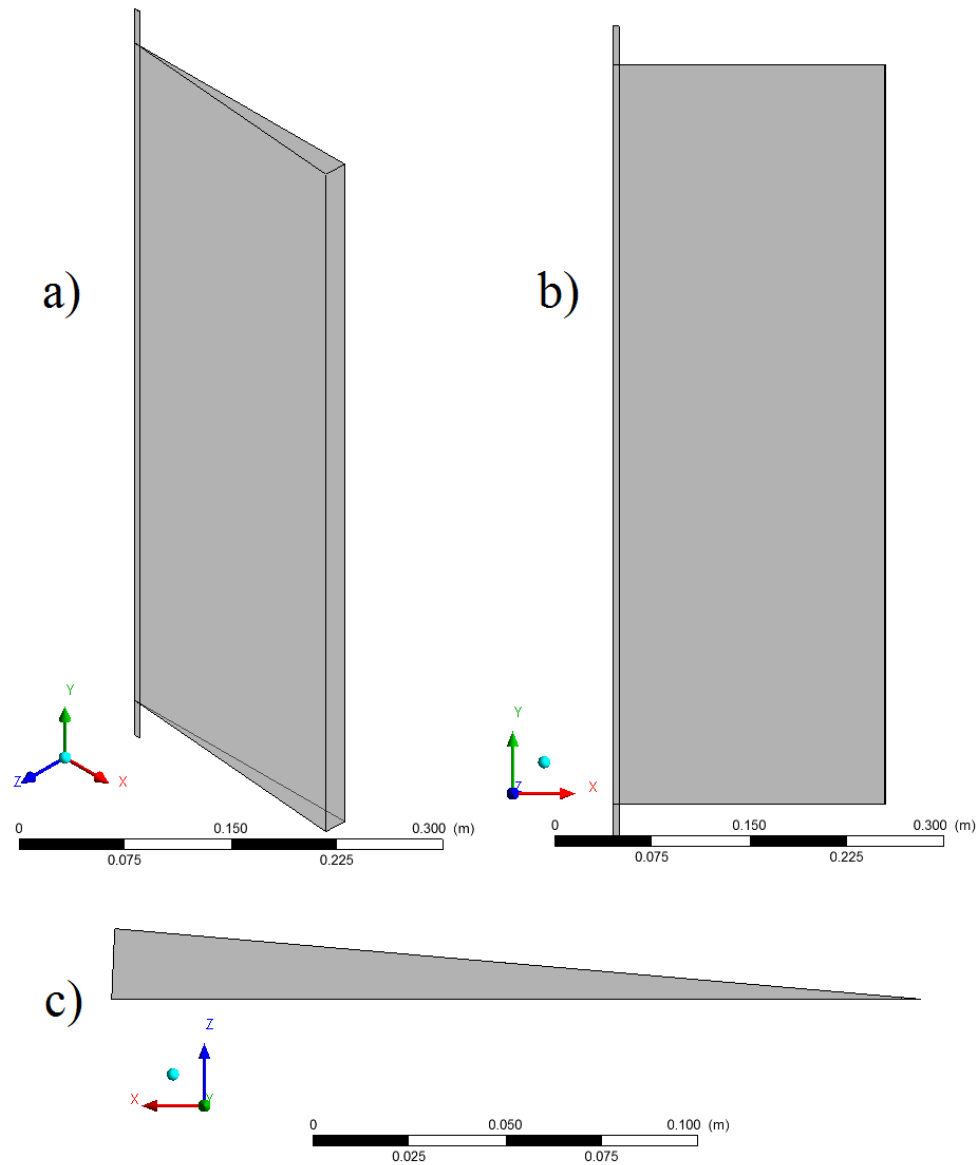


Figure E.1 – (a) Isometric view of the geometry used for the storage tank mesh created in ICEM, (b) Front view, (c) Top View.

Table E.1 – Dimensions of the geometry used for the mesh of the storage tank.

Tank Height (m)	2.032
Tank Diameter (m)	1.158
Inlet Pipe Diameter (m)	0.0254

Inlet/Outlet Pipe Length (<i>m</i>)	0.3
Extrusion Angle	5°

The number of nodes used to create the mesh was similar to the simulations performed by Nizami et al. The grid independence study shown by Nizami revealed that there was a negligible change in the simulation results when the amount of nodes was doubled from 43 in the radial direction and 249 in the axial direction. Therefore, for the simulations in this thesis, 45 nodes were used in the radial direction with minimum and maximum spacing between the grid points of 1.2mm and 5.46mm, respectively. The height of the storage tank was represented with 249 nodes in the axial direction with minimum and maximum spacing of 1.10mm and 2.309mm. For the inlet and outlet pipes, 5 nodes were used for the radial direction and 15 nodes were used in the axial direction with minimum and maximum spacing of 1.10mm and 2.225mm.

E.1.2 ANSYS CFX 14.0 Simulation Parameters

Simulations using the previously developed mesh were performed using ANSYS CFX 14.0. A time step size of 0.2 seconds was used since the results obtained by Nizami et al. did not vary when the time step size was reduced from 0.2 to 0.1 seconds. Buoyancy was determined with gravity acting in the negative y-direction and a reference temperature of 20°C. The heat transfer model was set to Thermal Energy and turbulence was captured using the Shear Stress Transport model. Buoyancy turbulence was also included in the production and dissipation terms of the turbulence model. High resolution was used for the

advection scheme since Nizami et al. found that better temperature predictions were found compared to the first order advection scheme.

The initial temperature of the water in the storage tank was set to 24.5°C and the water entering the tank was at 39.9°C . The walls of the tank were given no-slip conditions and were set as adiabatic. The sides of the mesh were given symmetry boundary conditions. The inlet boundary condition was set as a constant velocity over the entire cross-section. The magnitude of the inlet velocity was determined using the inlet Reynolds number, Eq. (E.1), as specified by Nizami. The fluid properties were determined at the average temperature between the initial and inlet fluid temperatures. Therefore, the fluid density and viscosity were 994.5 kg/m^3 and $7.4197 \times 10^{-4} \text{ kg/ms}$, respectively, which resulted in an inlet velocity of 0.10024 m/s . Finally, an average static pressure was given for the outlet boundary condition with a relative pressure of 0 Pa.

$$\text{Re} = \frac{\rho u_{\text{in}} D_P}{\mu} = 1340 \quad (\text{E.1})$$

$$u_{\text{in}} = \frac{1340 \left(7.4197 \times 10^{-4} \frac{\text{kg}}{\text{ms}} \right)}{994.5 \frac{\text{kg}}{\text{m}^3} (0.0254 \text{ m})} = 0.10024 \frac{\text{m}}{\text{s}} \quad (\text{E.2})$$

E.2 Choice of Initial Volume for Region 2

To determine the temperature of Region 2 with time for the inlet jet mixing model, an initial volume was needed where hot fluid enters from the jet region (Region 1). Realistically, the region would not have a volume at $t = 0$ since the entire tank is filled with cold fluid and no jet exists. However, in order to solve for the differential equation, a

non-zero initial condition was required. Therefore, the depth at which Region 2 extends at $t = 0$ was set to a very small value, C_i .

The value of C_i needed to be chosen such that the results of the inlet jet mixing model were not affected. Therefore, the effects of varying C_i on the duration of time interval 1, t_o , and the temperature of Region 2, $T_2(t)$, were studied.

Figure E.2 shows how the duration of time interval 1 was effected for different values of C_i when simulated with the low Reynolds number conditions studied by Oliveski et al. [18]. With larger values of C_i , t_o was smaller because the initial position of the thermocline would be located at a larger distance from the top of the tank. Therefore, it takes a shorter amount of time for the center of the thermocline to intersect with the inlet jet penetration depth. As C_i is reduced, the variation in the value of t_o becomes smaller.

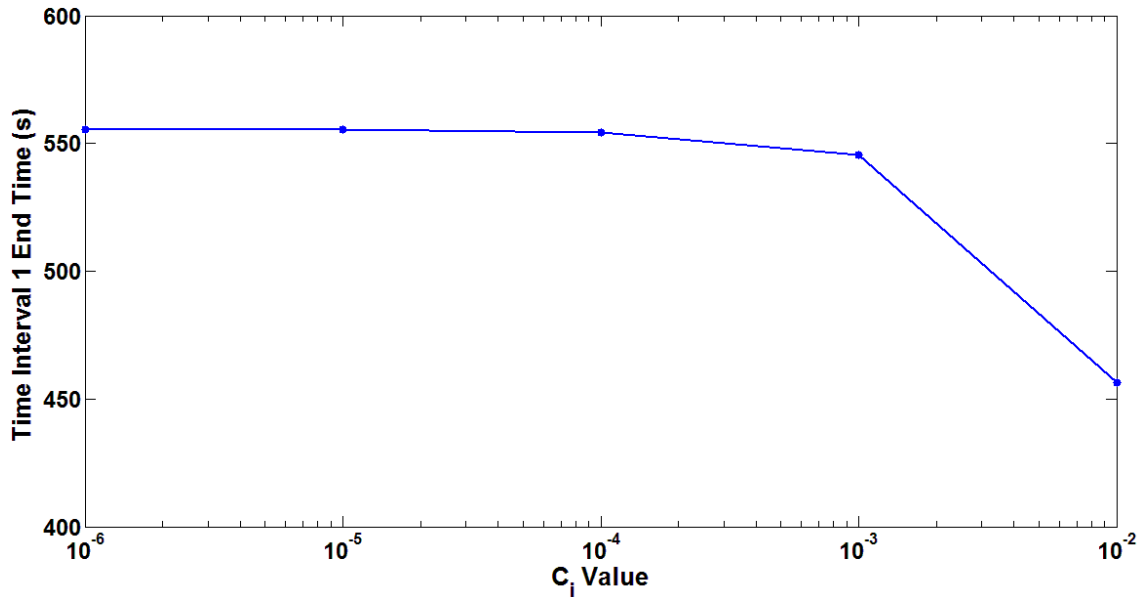


Figure E.2 – Calculated values for the duration of time interval 1 using different values for the initial depth of Region 2, C_i , using the low Reynolds number conditions studied by Oliveski et al. [18].

The effect of C_i on the temperature of Region 2, $T_2(t)$, with time is shown in Figure E.3. With larger values of C_i , the temperature increases at a slower rate because there is initially a larger volume of cold fluid that mixes with the warmer fluid entering from Region 1. Therefore, it takes a longer period of time before the temperature of Region 2 reaches a constant value. This would affect the accuracy of the final temperature profile within the tank because the predicted temperature of the inlet mixing region would be lower than expected. As the value of C_i is reduced, the profiles for T_2 converge.

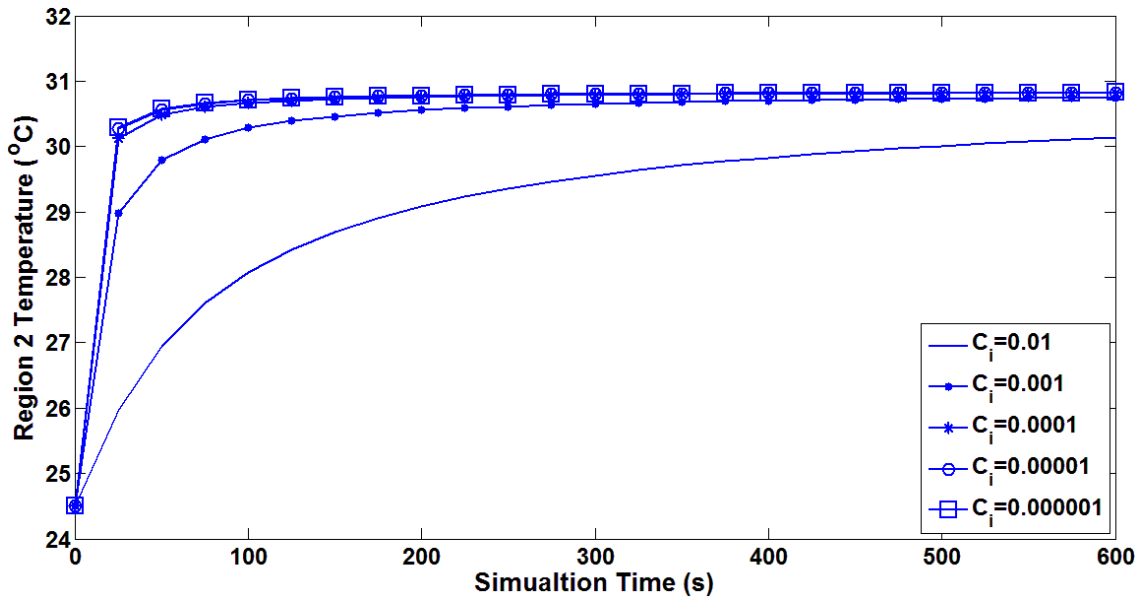


Figure E.3 – Region 2 temperature versus time for different values of C_i using the low Reynolds number case studied by Oliveski et al. [18].

From the results of these simulations, the value of C_i chosen for the inlet jet mixing analytical model was 0.00001m. This value ensured that the results obtained for the duration of time interval 1 and the Region 2 temperature with time were not affected by the initial volume of Region 2 for the low Reynolds number case.